



저작자표시-비영리-변경금지 2.0 대한민국

이용자는 아래의 조건을 따르는 경우에 한하여 자유롭게

- 이 저작물을 복제, 배포, 전송, 전시, 공연 및 방송할 수 있습니다.

다음과 같은 조건을 따라야 합니다:



저작자표시. 귀하는 원저작자를 표시하여야 합니다.



비영리. 귀하는 이 저작물을 영리 목적으로 이용할 수 없습니다.



변경금지. 귀하는 이 저작물을 개작, 변형 또는 가공할 수 없습니다.

- 귀하는, 이 저작물의 재이용이나 배포의 경우, 이 저작물에 적용된 이용허락조건을 명확하게 나타내어야 합니다.
- 저작권자로부터 별도의 허가를 받으면 이러한 조건들은 적용되지 않습니다.

저작권법에 따른 이용자의 권리는 위의 내용에 의하여 영향을 받지 않습니다.

이것은 [이용허락규약\(Legal Code\)](#)을 이해하기 쉽게 요약한 것입니다.

[Disclaimer](#)

공학박사학위논문

Electrical Properties of Single and Multiple Layer Graphene:

Carrier Concentration vs. Mobility

단일층 및 다층 그래핀의 전기적 특성:

캐리어 농도 vs. 이동도

2021 년 2 월

서울대학교 대학원

재료공학부

김민식

Electrical Properties of Single and Multiple Layer Graphene:

Carrier Concentration vs. Mobility

지도 교수 김 기 범

이 논문을 공학박사 학위논문으로 제출함

2021 년 1 월

서울대학교 대학원

재료공학부

김 민 식

김민식의 공학박사 학위논문을 인준함

2021 년 1 월

위 원 장 _____ 이 태 우 (인)

부위원장 _____ 김 기 범 (인)

위 원 _____ 김 진 영 (인)

위 원 _____ 유 재 철 (인)

위 원 _____ 조 성 용 (인)

**Electrical Properties of Single and
Multiple Layer Graphene:
Carrier Concentration vs. Mobility**

단일층 및 다층 그래핀의 전기적 특성:
캐리어 농도 vs. 이동도

A DISSERTATION SUBMITTED TO
DEPARTMENT OF MATERIALS SCIENCE AND ENGINEERING
SEOUL NATIONAL UNIVERSITY

FOR THE DEGREE OF
DOCTOR OF PHILOSOPHY

Min-Sik Kim

January 2021

Abstract

Electrical Properties of Single and Multiple Layer Graphene: Carrier Concentration vs. Mobility

Min-Sik Kim

Department of Materials Science and Engineering

The Graduate School

Seoul National University

Graphene is the most notable example of two-dimensional (2D) material. It has attracted significant attention due to its remarkable electrical, optical, and mechanical properties. In this dissertation, the electrical properties of single and multilayer graphene synthesized by chemical vapor deposition (CVD) are investigated. The graphene that is grown *via* CVD is inherently polycrystalline. As a result, the charge transport is hindered by scattering at the grain boundaries. I described a mechanism of direct visualization of the graphene grain boundary on Cu through Cu oxidation and the effect of Cu oxide growth on the electrical properties of graphene (Chapter 2). Besides, the effect of graphene grain boundary on the electrical properties by growing graphene on liquid Cu is investigated (Chapter 3). Finally, in chapter 4, the effect of interface and surface properties on electrical properties in multilayer graphene is studied as a function of the number of graphene layers.

Chapter 1 is the introductory section. It provides an overview of the properties of graphene. In addition, various methods of synthesizing graphene were briefly described. Among them, the advantages and principles of the CVD method using a metal catalyst are introduced. Although graphene synthesized by CVD is known to exhibit high quality, the electrical properties of single-layer graphene reported in papers show variations. The reason for this variation is that the thickness of graphene is so thin that various factors critically influence the electrical properties. The influencing factors are summarized as the effects of surface doping, interface scattering, and grain boundary scattering.

In chapter 2, direct visualization of graphene grain boundaries are reported. The

selective Cu oxidation through graphene grain boundary reveals that the graphene grains. The oxidation kinetics of Cu through graphene were evaluated from the surface coverage of Cu oxide (F_{ox}) by varying the oxidation time (10–360 min) and temperature (180°C–240°C) under an air environment. Transmission electron microscopy studies revealed that Cu_2O growth was governed by the out-diffusion of Cu through graphene grain boundaries. Further, the effect of Cu oxidation on graphene quality was investigated by measuring the electrical properties of graphene after transferring. The variation of the sheet resistance as a function of oxidation time at all oxidation temperature was converted into one curve as a function of F_{ox} . The sheet resistance of 250 Ω/sq was constant, similar to that of as-grown graphene up to $F_{ox} = 15\%$, and then it abruptly increased with F_{ox} . The sheet resistance is solely related to the decrease in the Hall mobility which clearly indicates damage of graphene. Therefore, we systematically developed the oxidation kinetics of Cu through graphene and simultaneously examined the changes in the electrical properties of graphene.

In order to liquid Cu phase effect on growth behavior and electrical property of graphene, in chapter 3, I compared the graphene grown on solid and liquid Cu. The graphenes were grown above and below the copper (Cu) melting point (1083 °C) by only changing the growth temperature from 1020 °C to 1100 °C at intervals of 40 °C. As the phase of the Cu catalyst changes from solid to liquid, the grain size of graphene increases by 2 orders of magnitude from 0.4 to 40 μm , while the nuclei density decreases by 4 orders of magnitude from 3.02 $/\mu m^2$ to 0.0004 $/\mu m^2$. The effect of the smooth surface of the liquid metal catalyst on graphene growth is remarkable even after considering the temperature difference. The reduction of defect density arising from the increase of the graphene grain size effect on carrier mobility which was increased from 180 to 760 cm^2/Vs . It resulted in sheet resistance, which was reduced from 1764 to 484 Ω/sq . Simple melting of Cu catalyst provides an improvement of the graphene quality without further tuning of the growth parameters.

The electrical properties of multilayer graphene with different interface and surface properties are investigated in chapter 4. All multilayer graphenes were prepared by the multiple transfers of CVD grown single-layer graphene with multiple Cu etching. First, the effect of interface properties with and without dopant between graphene layers on the electrical properties of multilayer graphene was investigated by varying the number of layers from 1 to 12. In both of the cases, the sheet resistance decreased with the increasing number of layers; from 700 to 104 Ω/sq for the interlayer-undoped graphene and from 280 to 25 Ω/sq for the interlayer-doped graphene. Further, Hall measurements revealed that the origins of the sheet resistance reduction in the two cases are different. In the interlayer-undoped

graphene, the sheet resistance decreased due to the increase in mobility with the addition of inner layers, which has a low carrier density and high carrier mobility. On the other hand, it decreased due to the increase in sheet carrier density in the interlayer-doped multilayer graphene. The mobility and carrier density variations in both of the cases were confirmed by fitting with the model of the Hall effect in the heterojunction. Besides, we found that even if there are polymer residues between graphene layers, it behaves like a dopant, so as the number of graphene layers increases, the mobility does not change and the carrier density increases. Furthermore, surface property modification by the doping of the top layer and the formation of double-layer graphene with different partial coverages allow the separate control of carrier density and mobility.

In conclusion, the electrical properties of single and multilayer graphene were studied. The graphene grain boundary visualization through Cu oxidation is governed by out-diffusion of Cu cation at graphene grain boundary which minimizes the damage to graphene quality, therefore no degradation is observed on the electrical property of graphene up to 15% of Cu oxide coverage. By comparing the growth behavior of graphene on solid and liquid Cu, it is suggested that the flat surface of liquid Cu extremely reduces the heterogeneous nucleation which increases grain size. Therefore, the carrier mobility of graphene enhanced which synthesized on liquid Cu. Finally, it was confirmed that the main factor (carrier density and mobility) of sheet resistance reduction depending on the interface and surface properties of multilayer graphene by varying the location of dopants and polymer residues. It provides an effective approach for controlling the properties of multilayer graphene for electronic applications.

Keyword: graphene, grain boundary, visualization, multilayer graphene, sheet resistance, carrier density, mobility

Student Number: 2014-30208

Table of Contents

Abstract	i
Table of contents	iv
List of tables	vi
List of figures	vii

Chapter 1. Introduction 1

1.1. The fundamentals of graphene	2
1.1.1. Background	2
1.1.2. The band structure of graphene	9
1.1.3. Properties of graphene.....	13
1.2. Graphene synthesis methods	17
1.2.1. Chemical vapor deposition graphene	20
1.3. The factors affecting the electrical properties of graphene	24
1.3.1. Doping by surface adsorbed molecules.....	27
1.3.2. Interface (substrate) scattering	31
1.3.3. Grain boundary scattering	34
References	37

Chapter 2. Graphene grain boundary visualization by Cu oxidation 45

2.1. Introduction	46
2.2. Experimental details	49
2.2.1. Synthesis of graphene.....	49
2.2.2. Cu oxidation on graphene/Cu foil structure	49
2.2.3. Characterization of graphene and Cu oxide	49
2.3. Results and discussion.....	52
2.3.1. Characterization of as-grown graphene.....	52
2.3.2. Selective oxidation of Cu at graphene grain boundary	54
2.3.3. Cu oxidation mechanism.....	57
2.3.4. Cu oxide growth kinetics.....	61
2.3.5. Electrical properties of graphene based on Cu oxidation.....	65
2.4. Summary and conclusion	71
References	72

Chapter 3. Liquid Cu phase effect on graphene growth	77
3.1. Introduction	78
3.2. Experimental details	81
3.2.1. Synthesis of graphene	81
3.2.2. Transfer and Characterization	83
3.3. Results and discussion	84
3.3.1. Growth behavior of graphene	84
3.3.2. Comparison of electrical properties of graphene grown on solid and liquid copper by chemical vapor deposition	92
3.4. Summary and conclusion	94
References	95

Chapter 4. Electrical properties of interface-engineered multilayer graphene	100
4.1. Introduction	101
4.2. Experimental details	105
4.2.1. Synthesis of partial and full coverage single-layer graphene	105
4.2.2. Graphene transfer (layer-by-layer stacking) and chemical doping	106
4.2.3. Characterization	109
4.3. Results and discussion	110
4.3.1. Characterizations of inter-layer doped and undoped multilayer graphene	110
4.3.2. Electrical properties of interlayer doped and undoped multilayer graphene	117
4.3.3. Undoped multilayer graphene surface doping with dopant	122
4.3.4. Multilayer graphene with interlayer polymer residue	124
4.3.5. Double-layer graphene with different 2 nd layer coverage	126
4.4. Summary and conclusion	128
References	129

Chapter 5. Summary and conclusions	136
---	------------

Abstract (in Korean)	141
List of publications	143

List of tables

Chapter 1

Table. 1-1. Four representative methods for obtaining graphene films.

Table. 1-2. .Summary of previous studies on graphene doping by molecule adsorption.

Table. 1-3. .Summary of previous studies on mobility of graphene with different substrate.

Table. 1-4. .Summary of previous studies on enlarging grain size methods.

Chapter 2

Table. 2-1. Oxidation conditions of Cu coated by graphene

List of figures

Chapter 1

Figure. 1-1. Graphene lattice structure: sp^2 hybridized carbon atoms arranged in a 2D honeycomb lattice.

Figure. 1-2. sp^2 hybrid orbitals with three major lobes at 120° . The remaining orbital, p_z , is sticking out of the plane of graphene.

Figure. 1-3. Lattice structure of graphene. (a) Real lattice. The dots represent C atoms. (b) Reciprocal lattice. Γ and K(K') are the center and edge points of the hexagon (= first Brillouin zone), respectively.

Figure. 1-4. (a) The micromechanical cleavage technique using Scotch tape for producing graphene. (b) Optical microscopy image of first observed single layer graphene.

Figure. 1-5. Graphene on 300 nm SiO_2 imaged with white light. The contrast can also be used as a quantitative tool for defining the number of graphene layers on a given substrate.

Figure. 1-6. (a) Energy bands near the Fermi level in graphene. The conduction and valence bands cross at points K and K'. (b) Energy bands in vicinity of K and K' points. (c) Density of states near the Fermi level with Fermi energy E_F .

Figure. 1-7. A single and bilayer graphene suspended on a porous membrane. Optical absorbance is measured at 2.3% per layer. The inset shows the sample design with several apertures.

Figure. 1-8. (a) SEM image of a typical suspended six-probe graphene device taken at 15° with respect to the sample plane. Device schematic of partially etched SiO_2 , side-view.

Figure. 1-9. Schematic of CVD graphene growth mechanisms on Ni and Cu.

Figure. 1-10. Schematic of monolayer graphene growth by CVD on Cu.

Figure. 1-11. Sheet resistance deviation of CVD graphene.

Figure. 1-12. Process flow of graphene synthesis and transfer.

Figure. 1-13. (a) Optical microscopy images of polymer residues after graphene transfer. (b) Current-voltage transfer curves for field effect transistors measured in air, as a function of initial concentration of PMMA solution. (c) Doping states of graphene during exposure to air within 10 h.

Figure. 1-14. Schematics of (a) charge impurity scattering and (b) acoustic phonon scattering of graphene electron on SiO₂.

Figure. 1-15. Schematic of random nucleation and growth CVD graphene on Cu.

Chapter 2

Figure. 2-1. Optical microscope image of as-grown single-layer graphene on Cu foil. Except for the Cu grain boundaries, there is no optical contrast observed as graphene defects.

Figure. 2-2. OM images of the as-grown graphene after the oxidation at (a)–(d) 180°C, (e)–(h) 200°C, (i)–(l) 220°C, and (m)–(p) 240°C

Figure. 2-3. (a) Optical microscopy image and (b) SEM image of sample oxidized at 220 °C for 1 hour. EDS mapping image of (b), representing Cu (c) and O (d) element, respectively.

Figure. 2-4. Cross-sectional TEM images and EDS analysis (a) bright-field STEM image, (b) HAADF STEM image, (c) SADP of Cu₂O, (d) HRTEM image, (e) EDS line spectrum across the interface between Cu and Cu₂O, and (f) schematic diagrams of Cu oxidation through graphene grain boundary.

Figure. 2-5. Cross-sectional HRTEM image at the interface between Cu and Cu₂O.

Figure. 2-6. (a) RGB colored optical image file is converted to an integer file with 256-gray scale. (b) The count of damaged pixels is extracted from the intensity histogram and (c) it is divided by the total number of pixels to obtain the oxide coverage.

Figure. 2-7. (a) Cu oxide coverage as a function of oxidation time and (b) oxidation reaction constant as a function of inverse oxidation temperature.

Figure. 2-8. Electrical properties of graphene as a function of the oxidation time at different oxidation temperatures (180°C, 200°C, 220°C, and 240°C); (a) sheet resistance (b) sheet carrier density, and (c) Hall mobility with dashed lines which represent the values of the as-grown graphene.

Figure. 2-9. Electrical properties of graphene as a function of Cu oxide coverage at different oxidation temperature (180°C, 200°C, 220°C, 240°C); (a) sheet resistance (b) sheet carrier density, and (c) Hall mobility. The black dashed lines represent the values of the as-grown graphene. (d) contour map of graphene sheet resistance with white dashed lines which indicates constant F_{ox} lines of 10% and 15%. The blue star represents the optimal condition of G-GB visualization.

Figure. 2-10. Optical image of graphene transferred to SiO₂/Si substrate

Chapter 3

Figure. 3-1. Schematic illustration of partial and full coverage graphene growth on solid/liquid Cu at 1020, 1060 and 1100 °C.

Figure 3-2. SEM and optical images of graphene grown on solid and liquid Cu with various growth time. SEM image of (a) 10 min, (b) 20 min and (c) 30 min growth on solid Cu at 1020 °C. (d) 10 minutes, (e) 20 min and (f) 30 min growth on solid Cu at 1060 °C. Optical microscopy image of (g) 10 min, (h) 20 min and (i) 30 min growth on liquid Cu at 1100 °C after selective oxidation of Cu. Parallel arrows indicate graphene grains are aligned in the same directions.

Figure. 3-3. (a) Graphene coverage on Cu as a function of growth time obtained at different temperatures. (b) nuclei density and (c) grain size difference of graphene grown on solid and liquid Cu, respectively.

Figure. 3-4. TEM images of graphene grown on solid and liquid Cu. (a) Bright-field image of full coverage graphene grown on solid Cu (1020 °C) and (b) diffraction pattern of the dashed area of (a). (c) dark-field image of the same area from the diffraction spot 1. (d) Bright-field image of full coverage graphene grown on solid Cu (1060 °C) and (e) diffraction pattern of the dashed area of (d). (f) dark-field image of the same area from the diffraction spot 2. (g) Bright-field image of partial coverage hexagonal shaped graphene

ne grown on liquid Cu. The edges of the domains are delineated by dashed lines. (h-k) diffraction patterns taken in corresponding windows of grid.

Figure. 3-5. Raman spectra of full coverage graphene films grown on (a) solid Cu (1020 °C, 1060 °C) and (b) liquid Cu (1100 °C). (c-d) statistical analysis of Raman spectra on I_D/I_G and I_{2D}/I_G taken from randomly selected 100 points on full coverage graphene, respectively.

Figure. 3-6. Electrical property of full coverage graphene grown on solid and liquid Cu. (a) sheet resistance of graphene grown with different temperature and extracted (b) Hall mobility.

Chapter 4

Figure. 4-1. Schematic diagram showing graphene transfer by layer-by-layer stacking. Two types of multilayer graphene samples preparation: interlayer-undoped and interlayer doped multilayer graphene.

Figure. 4-2. Schematic diagram showing interlayer polymer residue existed multilayer graphene transferred by using thermal release tape.

Figure. 4-3. Optical microscope images of graphene on selectively oxidized Cu foil after (a) 3, (b) 5, (c) 7.5 and (c) 20 min of first growth step and (e) two-step growth.

(f) Optical microscope images which area is randomly selected of single-layer graphene transferred on SiO₂/Si.

Figure. 4-4. (a) Schematic diagram of *u*-MLG and *d*-MLG. The *u*-MLG has surface residues while in *d*-MLG, benzimidazole molecules are adsorbed between the graphene layers. (b) Optical transmittance at 550 nm as a function of the number of graphene layers. XPS spectra of *u*-SLG and *d*-SLG: (c) C 1s peak and (d) N 1s peak.

Figure. 4-5. Optical microscope images of *u*-MLG (a) 1 layer, (b) 2 layers, (c) 3 layers, (d) 4 layers and *d*-MLG (e) 1 layer, (f) 2 layers, (g) 3 layers, (h) 4 layers after transferred on SiO₂/Si.

Figure. 4-6. Raman spectrum analysis of graphene (a) Raman spectrum of *u*-SLG and *d*-SLG. (f) blueshifts of G and 2D band after doping. (g) The ratio of the 2D to G band intensities (I_{2D}/I_G) as a function of the number of graphene layers. Raman spectra of (a) *u*-MLG from 1 to 4 layers and (b) *d*-MLG from 1 to 4 layers. (c) FWHM of 2D band of *u*-MLG and *d*-MLG as a function of the number of graphene layers.

Figure. 4-7. The electrical property of *u*-MLG and *d*-MLG. (a) Sheet resistance, (b) sheet carrier density, and (c) carrier mobility of *u*-MLG (black) and *d*-MLG (red). And (d) separately magnified sheet carrier density of *u*-MLG. The dotted lines represent the calculated results.

Figure. 4-8. (a) Schematic diagram of surface doped *u*-MLG with benzimidazole molecules. Electrical properties of *u*-MLG (black) and top-layer doping of *u*-MLG (blue): (b) sheet resistance, (c) carrier mobility, and (d) carrier density.

Figure. 4-9. (a) Schematic diagram of MLG with polymer residue in the interlayers. Electrical properties of MLG with polymer residue in the interlayers: (b) sheet resistance, (c) carrier mobility, and (d) carrier density.

Figure. 4-10. (a) Optical microscope images of graphene transferred on SiO₂/Si by varying the additional layer coverage. (b) Resistor models of single-layer to double-layer graphene with increasing second-layer coverage. Black and red resistors represent sheet resistance of monolayer and double-layer graphene. (c) Variation in sheet resistance of the samples with different additional layer coverages, and (d) the corresponding variations in sheet carrier density (red) and carrier mobility (blue).

CHAPTER 1.

Introduction

1.1. The fundamentals of graphene

1.1.1. Background

Graphene is a two-dimensional sheet of sp^2 -hybridized carbon. It is a hexagonal lattice (*i.e.*, a honeycomb structure, as shown in **figure 1-1**) that is considered the basis of carbon allotropes with honeycomb lattices. The name graphene was introduced in 1986 which is a combination of the word *graphite* and the suffix *-ene*.¹ Although the exact definition of graphene refers to a single atomic layer of carbon, in general, the term graphene implies both the single-layer and multilayer graphene (the number of layers $< \sim 10$)

The crystal structure of graphene is formed by bonds between C atoms and is important for the physical properties of graphene. One C atom has four valence electrons that form various hybridized orbitals thereby allowing the formation of carbon allotropes and numerous organic materials. The s , p_x , and p_y atomic orbitals on each carbon hybridize to form strong covalent sp^2 bonds as shown in **figure 1-2**. The three sp^2 bonds are positioned at 120° and the length of these bonds is about 0.142 nm. The remaining outer-shell electron occupies a p_z orbital that is oriented perpendicularly to the plane. The p_z orbital on each carbon overlaps with its three neighboring carbons to form a band of filled π orbitals, known as the valence band and a band of empty π^* orbitals called conduction band which is responsible for most of the notable electronic properties of graphene. The graphene sheets stack to form graphite with an interplanar spacing of 0.335 nm. The Bravais lattice of graphene is a hexagonal lattice in which two carbon atoms correspond to one basis. The primitive unit cell and its unit vector (\mathbf{a}_1 and \mathbf{a}_2 with length $(a) = \sqrt{3}a_{C-C} = 0.246$

nm) are represented in **Figure 1-3(a)**. The reciprocal lattice of graphene is also a hexagonal lattice with a 90° rotation relative to the real lattice, as shown in **Figure 1-3(b)**. The hexagons in **Figure 1-3(b)** represent the first Brillouin zone of graphene, which is the region of interest when describing the structure of the electronic energy band. In particular, the high symmetry points (Γ , K, and K') are useful for describing the complete electronic properties of graphene. In the next section, the K point will be the focal point for determining the band structure of graphene.

The theory of graphene was first explored by Wallace in 1947 as a starting point for understanding the electronic properties of 3D graphite.² Since then, many researches have been conducted to isolate or grow graphene. In 1999, Ruoff's group presented one mechanical exfoliation approach for graphite by using an atomic force microscope (AFM) tip to manipulate small pillars patterned into highly oriented pyrolytic graphite by plasma etching. The thinnest slabs observed were more than 200nm thick.³ Kim's group later improved the method by transferring the pillars to a tipless cantilever, which successively stamped down slabs as thin as 10nm.⁴ In 2004, it was ultimately a much simpler approach that led to the first isolation of single-layer graphene by the Manchester group of Geim and Novoselov.⁵ As shown in **figure 1-4**, they pulled graphene layers from graphite and transferred them onto SiO₂ substrate by using the Scotch tape. Although the flakes present on the tape are much thicker than one layer, van der Waals attraction to the substrate can delaminate a single sheet when the tape is then lifted away. In addition, as shown in **figure 1-5**, the Manchester group made single layer of graphene visible on 300-nm-thick SiO₂ using the interference effect.⁶ It can also easily distinguish the number of graphene layers. Although these achievements seem simple, since then they have significantly contributed to the research on graphene that has been going on.

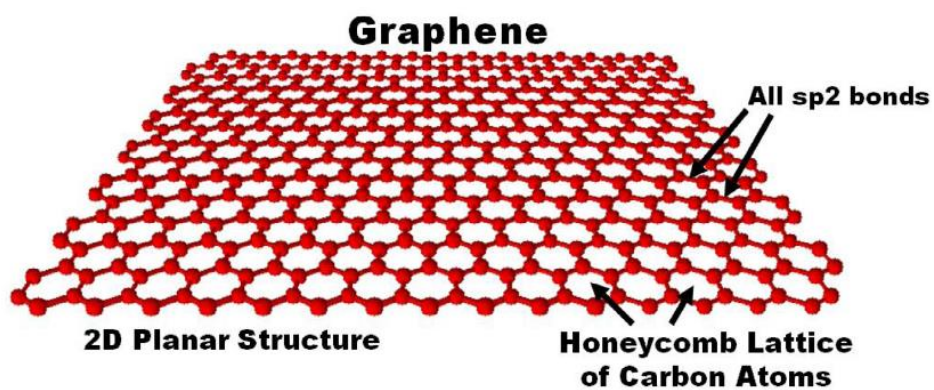


Figure. 1-1. Graphene lattice structure: sp^2 hybridized carbon atoms arranged in a 2D honeycomb lattice.⁷

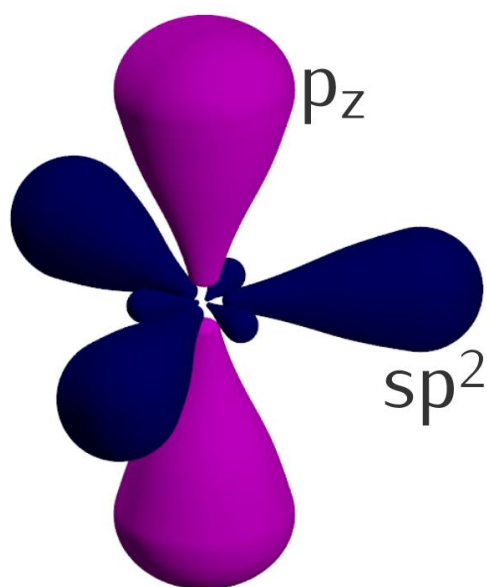


Figure. 1-2. sp^2 hybrid orbitals with three major lobes at 120° . The remaining orbital, p_z , is sticking out of the plane of graphene

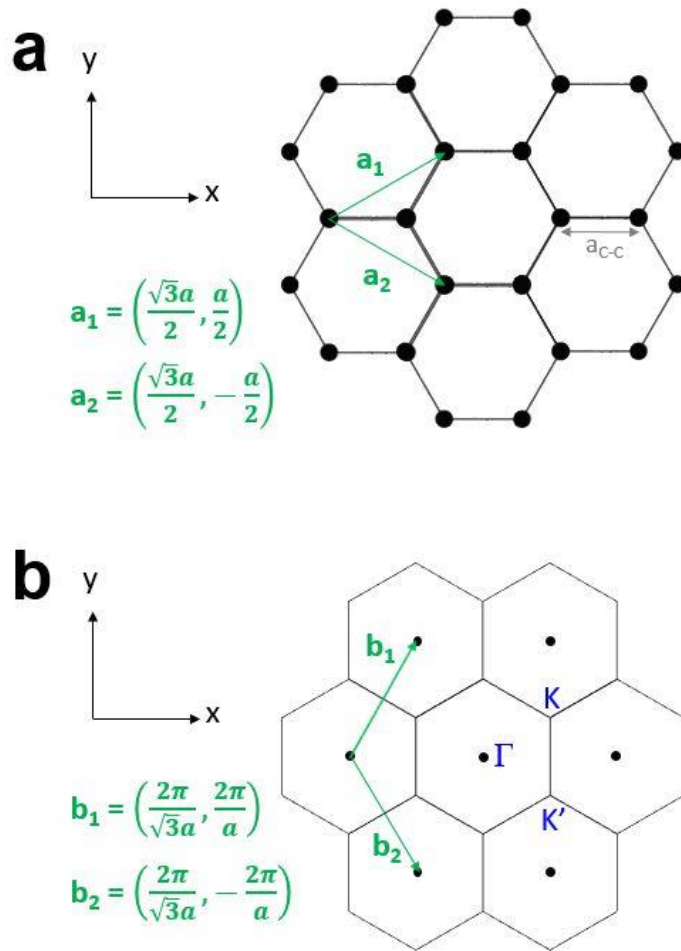


Figure. 1-3. Lattice structure of graphene. (a) Real lattice. The dots represent C atoms. (b) Reciprocal lattice. Γ and K(K') are the center and edge points of the hexagon (= first Brillouin zone), respectively.

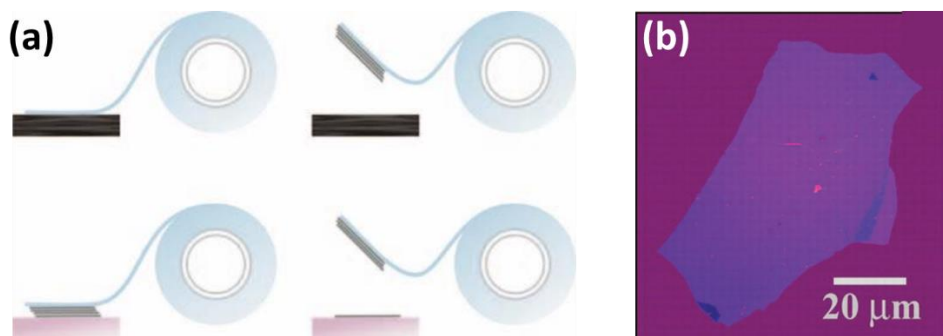


Figure. 1-4. (a) The micromechanical cleavage technique using Scotch tape for producing graphene. (b) Optical microscopy image of first observed single layer graphene. ⁵

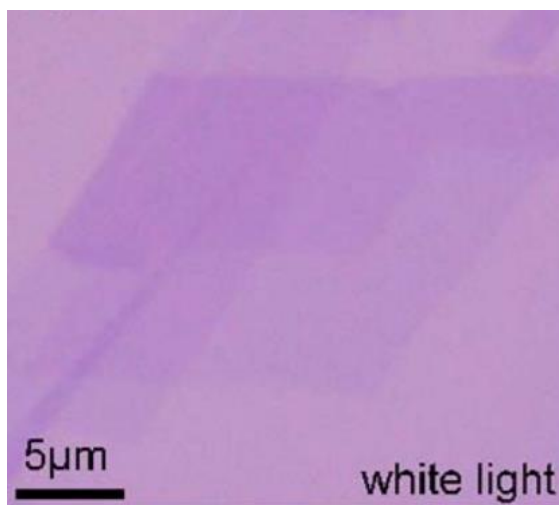


Figure. 1-5. Graphene on 300 nm SiO₂ imaged with white light. The contrast can also be used as a quantitative tool for defining the number of graphene layers on a given substrate.⁶

1.1.2. The band structure of graphene

To understand the behavior of electrons, the energy dispersion in reciprocal space (i.e., band structure) is detailed in this section. The energy-momentum (**E-k**) diagram including the full band structure at the first Brillouin zone of graphene shown in **figure 1-6 (a)**. The band of valence (band of π electrons) and conduction (band of π^* electrons) meet at Dirac points, which six points are located at the edge of the Brillouin zone. The momentum and energy of electrons show a linear energy-momentum dispersion with a dispersion relationship proportional to each other near the Dirac point. As a result, graphene is considered a semi-metal that exhibits conductivity due to zero-band gap, but the density of states at the Fermi level (E_F) is “0”.

Analysis of the band structure of graphene has been studied based on the model of tight-binding energy dispersion^{2,8-9} and it shows the following correlation between energy and momentum.

$$E(k) = \pm \gamma \sqrt{1 + 4\cos\frac{\sqrt{3}a}{2}k_x \cos\frac{a}{2}k_y + 4\cos^2\frac{a}{2}k_y} \quad (1-1)$$

where the sign of \pm represents the conduction band and the valence band, respectively, $\gamma \approx 3 \text{ eV}$ is the hopping integral of nearest neighbor, and a is 2.46 Å which is the basis of the unit cell size. Furthermore, energy-momentum dispersion near the Dirac point can be simplified as follows:

$$E(k) = \pm \frac{\sqrt{3}a}{2} \gamma |k| = \pm \hbar v_F k \quad (1-2)$$

where \hbar is the reduced Planck constant (6.582×10^{-16} eV·s). And, v_F of the electron in graphene reaches to 10^6 m/s which is 1/300 times of the light speed. This approximation is similar to the equation for Einstein's theory of relativity with the assumption of mass is negligible as follows:

$$E^2 = m^2 c^4 + c^2 p^2 \quad (1-3)$$

$$E = cp = \hbar ck \quad (1-4)$$

where m , c , and p are the rest mass, the velocity of light, and momentum, respectively. This can be understood as the case where the speed of light changes to the v_F of graphene. Therefore, the high mobility of graphene can be achieved because of its small effective mass.

To calculate the carrier density of graphene, the equation of the density of state $g(E)$ is calculated using Eq. 1-2 and v_F , as follows:

$$g(E) = \frac{2}{\pi(\hbar v_F)^2} |E| \quad (1-5)$$

The Eq. 1-5 indicates that $g(E)$ is a linear function of E as shown in **figure 1-6 (b)** and **(c)**. The Eq. 1-5 results the equation of intrinsic carrier density using Fermi-Dirac distribution as follows:¹⁰

$$n_i = \frac{\pi}{6} \left(\frac{k_B T}{\hbar v_F} \right)^2 \quad (1-6)$$

where T and k_B are temperature and Boltzmann's constant, respectively. At 285 K, n_i is $6.682 \times 10^{10} \text{ cm}^{-2}$ and the bulk density is $1.98 \times 10^{18} \text{ cm}^{-3}$. This value is 4–5 orders lower than that (10^{22} – 10^{23} cm^{-3}) of metal.

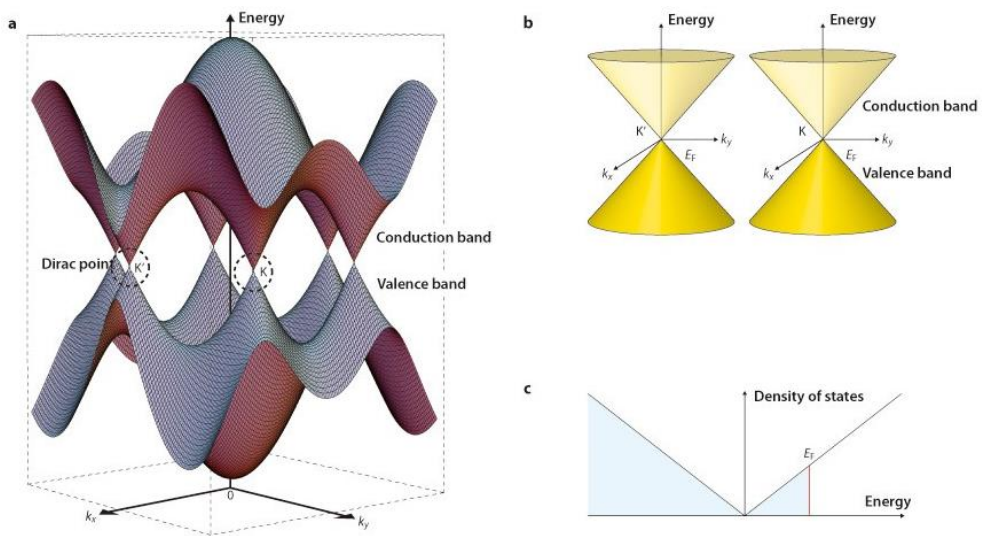


Figure. 1-6. (a) Energy bands near the Fermi level in graphene. The conduction and valence bands cross at points K and K' . (b) Energy bands in vicinity of K and K' points. (c) Density of states near the Fermi level with Fermi energy E_F .¹⁰

1.1.3. Properties of graphene

Graphene has excellent physical properties due to its extremely thin thickness, strong c-c bonding, and unique band structure. In this section, the outstanding characteristics of graphene are detailed.

The intrinsic strength of graphene is predicted to exceed that of any other material.¹¹ The graphene strength by atomic force microscopy (AFM) based measurement exhibit a large breaking strength of $\approx 40\text{N/m}$ due to the absence of planes associating the fracture strength with the strong c-c bonding.¹² Along with its high breaking strength graphene is also very pliable with Young's modulus $\approx 1.0\text{ TPa}$ and an elastic strain of up to 20%. The Young's modulus of graphene is an outstanding value compared to that of other materials. In addition, the superior thermal conductivity of $5,200\text{ W/mK}$ ($20\times\text{Cu}$) was measured on suspended graphene which is due to the isolation of electrons from phonons.¹³ And, the short C-C bond length of 0.142 nm in graphene implies that the pore size would be 0.246 nm which is smaller than the diameter of small molecules like helium and hydrogen. Therefore, the impermeability of graphene makes it possible to use it as a diffusion barrier for various gases.⁷ The atomically thin thickness of graphene provides high optical transmittance. The zero-band gap of graphene allows the energy transition between the conduction and valence band, regardless of the photon's frequency. From the universal AC conductivity for Dirac fermions ($G = e^2/4\hbar$), the optical transmittance of graphene (T) is as follows:

$$T = \left(1 + \frac{2\pi G}{c}\right)^{-2} = (1 + 0.5\pi\alpha)^{-2} = 1 - \pi\alpha \quad (1-7)$$

where $\alpha(= e^2/\hbar c)$ is the fine structure constant and $\pi\alpha$ is 2.3%.¹⁴ Eq. 1-7 indicates that T is constant with respect to the frequency of light. **Figure 1-7** shows experimentally measured T , which demonstrates the theoretical predictions. Accordingly, T depends only on the number of graphene layers (N) as follows.

$$T(\%) = 100 - N\pi\alpha = 100 - 2.3N \quad (1-8)$$

It implies that the single layer of graphene has high transmittance of 97.7% in visible light.

Because of the unique conical band structure of graphene which mentioned above, graphene is expected to have a very small effective mass of charge carriers, very high mobility, and very low carrier density. In 2008, Bolotin *et al.* investigated the mobility and carrier density of graphene which are obtained by mechanical exfoliation.^{15,16} In order to reduce the various scattering factors, they fabricated suspended graphene as shown in **figure 1-8** by a combination of electron beam lithography and etching of SiO₂ substrate. They achieved a very high mobility of 230,000 cm²/Vs with electron densities of 2×10^{11} cm⁻² which mobility is 20 times higher than that of silicon. Because of its extremely high mobility, graphene is expected to be a promising candidate for next-generation electronic materials such as high-speed transistors.

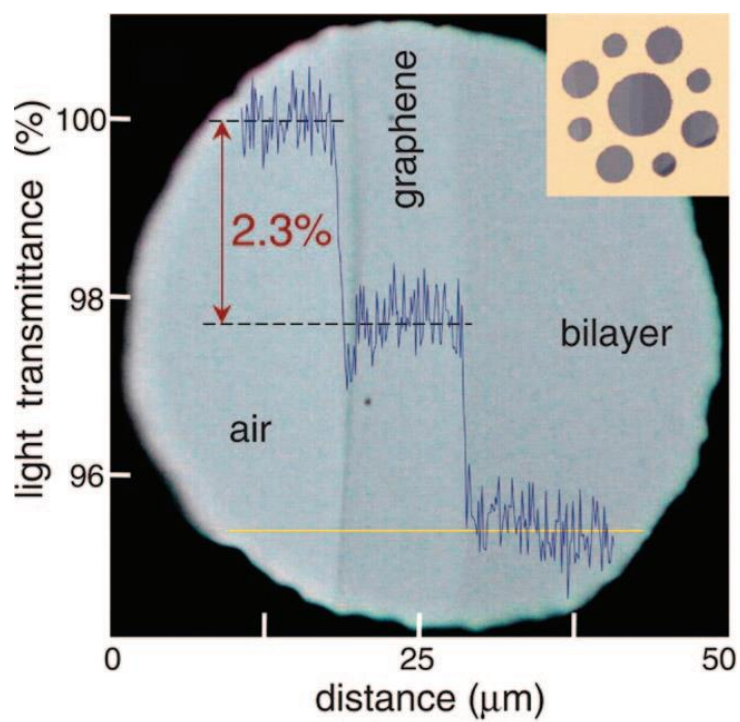


Figure. 1-7. A single and bilayer graphene suspended on a porous membrane. Optical absorbance is measured at 2.3% per layer. The inset shows the sample design with several apertures.¹⁴

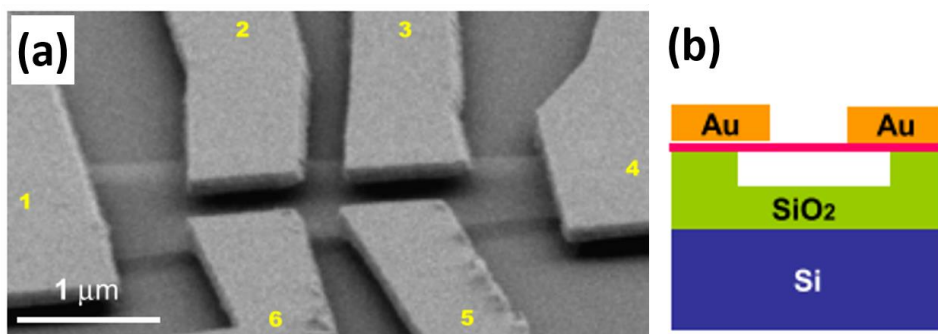


Figure. 1-8. (a) SEM image of a typical suspended six-probe graphene device taken at 15° with respect to the sample plane. Device schematic of partially etched SiO₂, side-view.¹⁵

1.2. Graphene synthesis methods

Due to various potential properties of graphene, demands for graphene have been increased. These requirements have been led the development of graphene synthesis methods. To apply the commercial field, high quality and large amount of production ability have been required. There are several methods to synthesis graphene. **Table 1-1** provides four representative methods to synthesis graphene.^{15,17-}

²¹ First method is mechanical exfoliation which graphene is obtained from graphite using scotch tape. It is difficult to control the size and shape so impossible to utilize it for large-scale applications. However, in terms of structural integrity, the obtained graphene exhibits the best properties. Thus, the efficiency of any new synthesis methods is determined by comparison with the properties of mechanically exfoliated graphene. Chemical reduction from the graphene oxide method can fabricate a large amount of graphene. Graphite is oxidized to graphene oxide by acid solution. And then the reduction process is conducted in the high-temperature furnace. Assembled graphene films have poor electrical properties and lots of defects. Defects formed during the oxidation and reduction processes. Another method to synthesis graphene is conversion of SiC to graphene. When SiC heated around 1400°C under vacuum, it results in the sublimation of silicon with the result that graphitization of carbon. This method allows for producing high-quality graphene.²² However, SiC substrates are expensive and the scale of graphene is limited by the size of the SiC substrate. And it is difficult to transfer graphene to the arbitrary substrate.

Finally, the most promising method is chemical vapor deposition (CVD) onto transition metal substrates such as Ni, Pd, Ru, Ir, or Cu.^{21,23-26} The essence is precursors in the vapor phase. Precursors are usually used carbon containing gas CH₄

or vapors of liquid carbon source alcohols. The precursors pyrolysis to carbon at high temperature and the formation of graphitic structure from dissociated carbon atoms. Transition metals serve as efficient catalysts that transform hydrocarbons into graphitic materials. It is expected to be the most suitable for large-scale and high-quality graphene production. In addition to this, it is relatively inexpensive.

Method	Mechanical exfoliation	Chemical reduction from graphene oxide	Epitaxial growth on SiC	Chemical vapor deposition based graphene growth
Size	10 ~ 100 μm	> 6 inch	< 4 inch	> 6 inch
Mobility	Best 200,000 cm^2/Vs	Low 1 cm^2/Vs	High 5,400 cm^2/Vs	High 4050 cm^2/Vs
Transfer	Yes	Yes	No	Yes
Application	No	Yes	Little	Most
Scalable	No	Yes	Not yet	Yes

Table. 1-1. Four representative methods for obtaining graphene films.¹⁷

1.2.1. Chemical vapor deposition graphene

The interest in graphene has led to the development of the CVD method using metals as a catalysts. Without metals, graphitic structure formed beyond 2500°C. This temperature is so high that needs a special setup for the deposition system and substrate. Furthermore, huge energy consumption could be a considerable issue. The function of metals is catalysts which lower the energy barrier of the reaction. The catalysts lower energy barriers not only for the pyrolysis of precursors but for the graphitic structure formation. Various metal catalysts were explored such as Ni, Cu, Co, Ru, Ir, Pd, Pt, and Re. Because of its low cost and etchability, among the various metals, Ni and Cu are most commonly used. Ruoff group studied the growth mechanism of Cu and Ni by utilizing a carbon isotope-labeled CH₄.²⁷ Due to the different carbon solubility of Cu and Ni, they show different growth mechanisms as shown in **figure 1-9**. The Ni has a carbon solubility of 0.1 atomic % at elevated temperature. This value cannot be neglected. After CH₄ is dissociated to carbon monomer at 1000°C and it dissolved into the Ni surface due to the finite solubility. Dissolved carbon atoms precipitate onto Ni surface and make graphene layers during the cooling. However, unwanted carbon deposition may also occur during cooling. The different cooling rate provides a thickness variation of graphene.²⁸ Extreme fast cooling leads to little carbon precipitation. This is because of not sufficient time which is not allowed for carbon to precipitate. On the other hand, slow cooling has nothing on the Ni surface in that carbon atoms diffuse deep into the bulk catalyst. Hence the control of the layer of deposited graphene is main challenge in Ni. It originated from the unique dimension of graphene. Graphene is a sub-nanometer-thick material, whereas the typical CVD deals with the film much thicker than

graphene. The growth of graphene requires extremely precise control of the thickness of film which has never been achieved in the past in CVD.

However, extremely low carbon solubility of Cu allows that carbon monomers only be decomposed and deposited on exposed Cu which indicates that single-layer graphene growth by self-limiting as shown in **figure 1-10**.²⁹ So, it provides easier controllability over the deposition of graphene on the copper surface as the cooling rate at the last step does not affect the graphene thickness. Therefore, since uniform thickness of single-layer graphene showing relatively high mobility of $4050 \text{ cm}^2/\text{Vs}$, was first grown on Cu,²¹ lots of CVD graphene growth studies have been focused on Cu. The CVD graphene quality can be manipulated by tuning process parameters such as pre-treatment of Cu, annealing, growth time, temperature, pressure, and gas flow rate of hydrocarbon, etc.

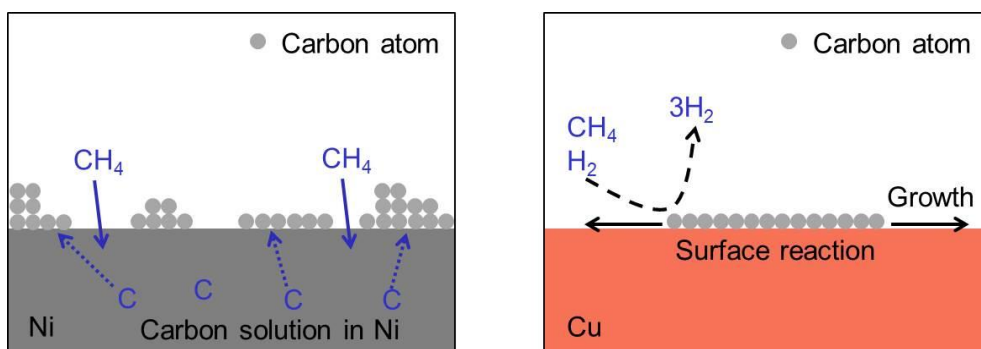


Figure. 1-9. Schematic of CVD graphene growth mechanisms on Ni and Cu.

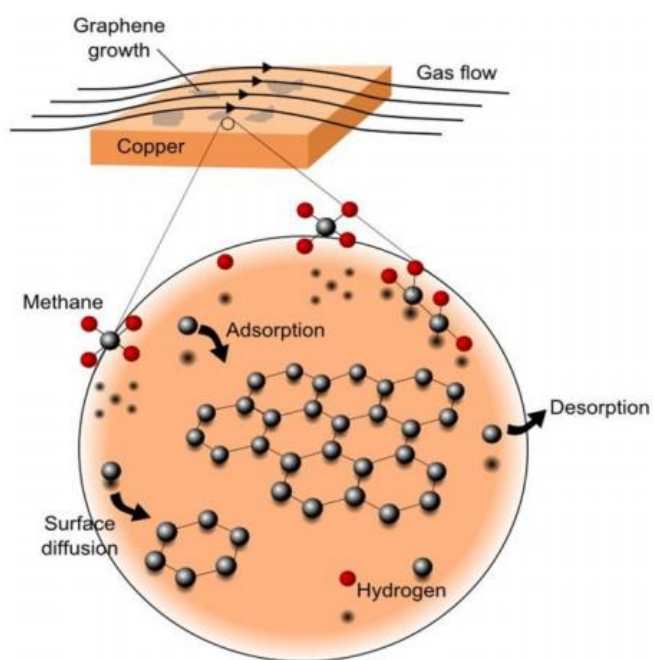


Figure. 1-10. Schematic of monolayer graphene growth by CVD on Cu.²⁹

1.3. The factors affecting the electrical properties of graphene

In this study, I focused on the electrical properties of CVD graphene. Due to the high mobility, the sheet resistance of Ideal graphene is expected to have a very low value of 30 Ohm/sq, but, as shown in **figure 1-11**, the sheet resistance of graphene grown by CVD actually shows much higher values.^{19,30-35} In addition, it is worth noting that although the various graphene shown in **figure 1-11** were grown on Cu as a single layer, the sheet resistance varies significantly from 300 to 1300 Ohm/sq. However, it is difficult to clearly define the origin of variation in sheet resistance from various studies. In order to measure the electrical properties of CVD graphene, synthesis and transfer processes are required as shown in **figure 1-12**. Not only defects during the synthesis process but also various artifacts such as tearing of graphene and polymer residue during the transfer process can cause changes in electrical properties. The conductivity, which generally represents the electrical properties of a material, is expressed as the product of carrier density, mobility, and unit charge as follows:

$$\sigma = qn\mu \quad (1-9)$$

In this part, factors that influence the electrical properties of graphene were explained by dividing them in terms of mobility and carrier density.

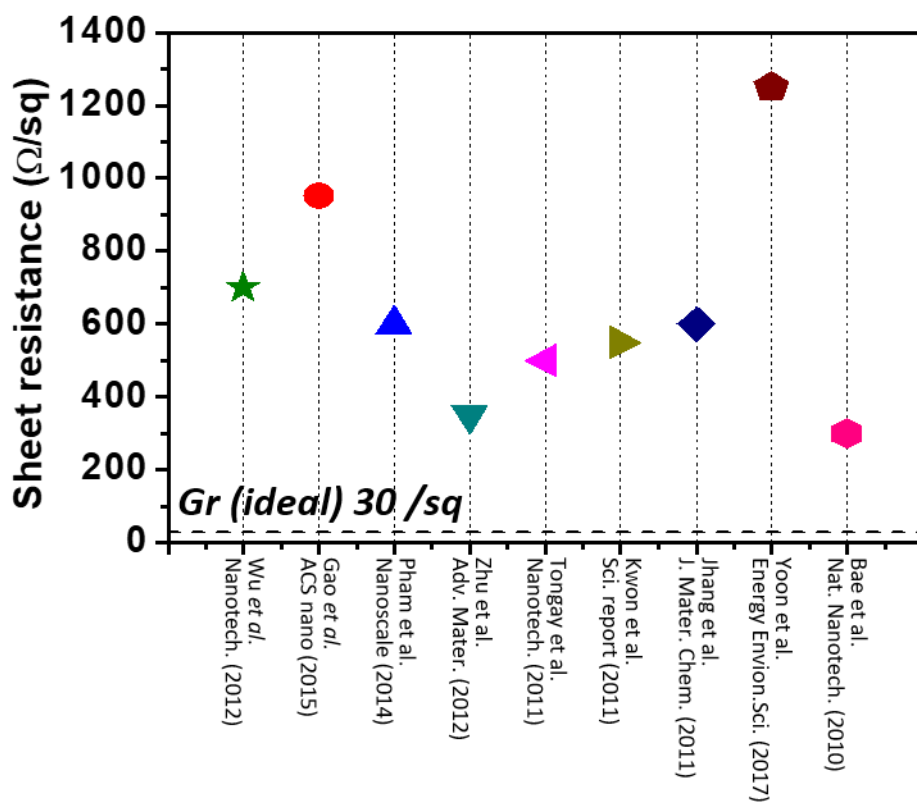


Figure. 1-11. Sheet resistance deviation of CVD graphene.^{19,30-35}

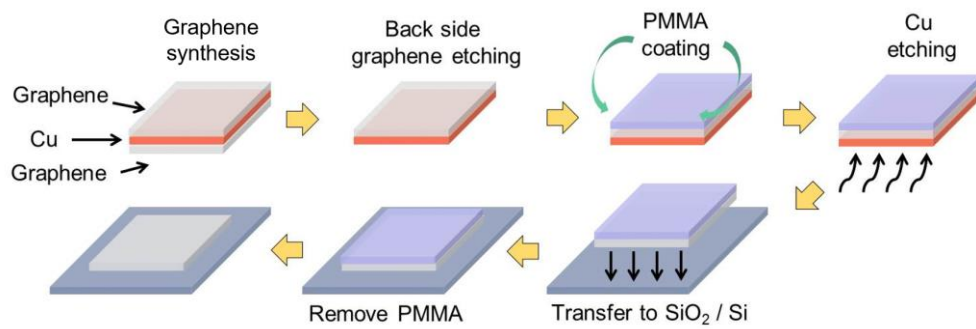


Figure. 1-12. Process flow of graphene synthesis and transfer.

1.3.1. Graphene doping by molecules adsorption

The graphene which is a single atomic layer is so thin that it is highly affected by surface conditions. Although the supporting polymer was removed during the transfer process, the polymer residues remained as shown in **figure 1-13(a)**.³⁶ It p-dopes graphene which was confirmed, as shown in **figure 1-13(b)**, through the shift of the Dirac point of the field effect transistor transfer curve.³⁷ Furthermore, even simply exposed to air, adsorbed oxygen and water molecules also p-dopes graphene (**figure 1-13(c)**).³⁸ Rather, using the sensitive surface properties of graphene, various studies to improve conductivity by adsorbing dopant molecules on the graphene surface are being conducted. Doping by molecules physisorption changes graphene carrier density by charge transfer due to the energy level difference between graphene and dopant. **Table 1-2** shows representative results of several doping processes using single-layer CVD graphene that report sheet resistance and carrier density. Nitrate-based dopants are widely used, low sheet resistance of 180 Ohm / sq was obtained by applying HNO₃,³⁹ a representative material. Studies on graphene doping by spin coating or dipping chloride-based materials such as metal chloride and chloroform have also been reported.^{40,41} The metal ions deposited on graphene are reduced by obtaining electrons from graphene, which makes graphene p-doping. Organic molecules containing amine groups have also been reported as p-type dopants.⁴²⁻⁴⁴ Among them, Benzimidazole molecules show high doping efficiency which results in the sheet resistance of 260 Ohm/sq. Benzimidazole doping is *in-situ* process in which graphene is doped simultaneously with Cu etching during the transfer process. The Benzimidazole molecules are covered by graphene. Therefore, it shows excellent stability as it is free from desorption and oxidation of molecules. Finally, materials with a larger work function than graphene, such as Ru and Pt,⁴⁵⁻⁴⁷

are selectively deposited on defects (e.g. particle boundaries, wrinkles, cracks, holes) through the ALD process to increase carrier density. Our group obtained a high carrier density of $1 \times 10^{14} \text{ cm}^{-2}$ by selective deposition of Ru.

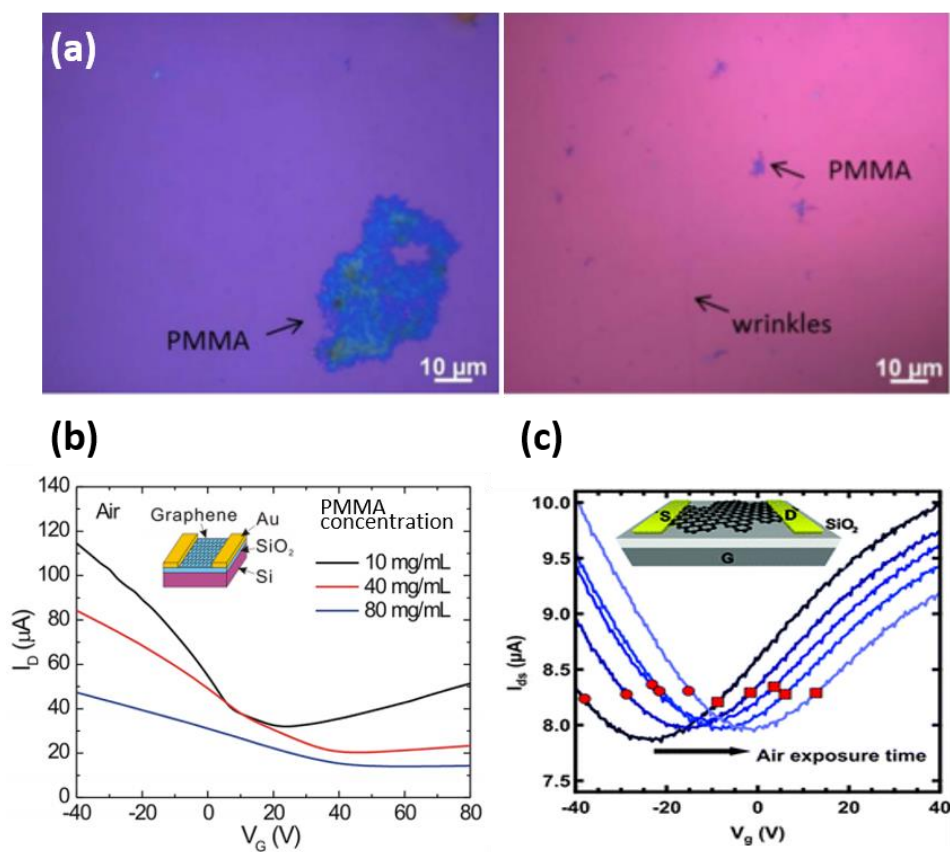


Figure. 1-13. (a) Optical microscopy images of polymer residues after graphene transfer. (b) Current-voltage transfer curves for field effect transistors measured in air, as a function of initial concentration of PMMA solution. (c) Doping states of graphene during exposure to air within 10 h.³⁶⁻³⁸

Dopant	Method	R _s (Ω/sq)	Carrier density (cm^{-2})	Doping type	Ref. No.
HNO ₃	Dipping	180	4×10^{13}	p	39
AuCl ₃	Spin-coating	500	1.6×10^{13}	p	40
CHCl ₃	Dipping	300	1.8×10^{13}	p	41
C ₆ H ₄ N(NH)CH	Cu etching	~260	1×10^{13}	p	44
Ru	ALD	125	10×10^{13}	p	47

Table. 1-2. Summary of previous studies on graphene doping by molecule adsorption.^{39-41,44,47}

1.3.2. Interface (substrate) scattering

Next, it is the factor that changes the carrier mobility of graphene. The electrical property of graphene is also strongly influenced by the interface property between graphene and substrate. The surface of SiO₂, which is mainly used for characterization of CVD graphene, causes phonon-related carrier scattering and trapping in charged impurities, as shown in **figure 1-14**. It results additional scattering which limits the mobility of graphene.^{48,49} To solve the problem, the results of the mobility by changing the substrates are summarized in **table 1-4**.^{15,50,51} Graphene transferred to another two-dimensional material of dangling bond free substrate, hexagonal boron nitride (h-BN), which reduces impurity scattering, improving mobility up to 20000 cm²/Vs.⁵⁰ In addition, the hydrophobic properties of hexamethyldisilazane (HMDS) prevent the deposition of dipoles on the surface, thereby suppressing additional scattering and improving mobility.⁵¹ Therefore, pristine graphene with nothing in the interface can be expected to have very high mobility due to the absence of additional scattering elements. As mentioned earlier, suspended graphene has a very high mobility of 230,000.¹⁵

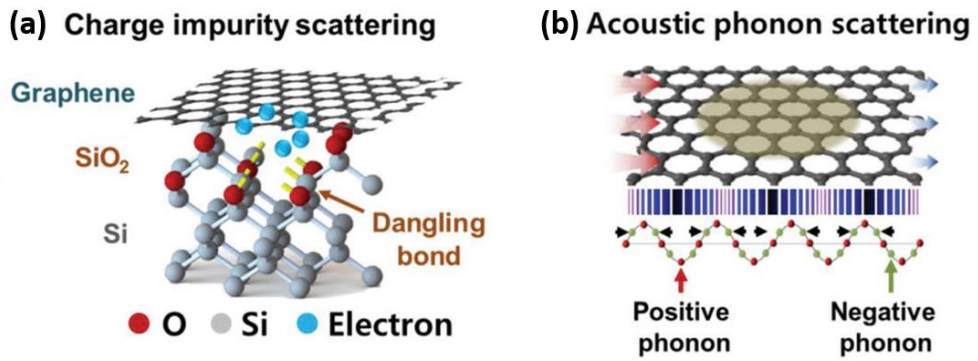


Figure. 1-14. Schematics of (a) charge impurity scattering and (b) acoustic phonon scattering of graphene electron on SiO_2 .⁴⁹

Substrate	Carrier mobility (cm ² /Vs)	Ref. No.
SiO ₂	~ 4,000	51
h-BN	15,000 ~ 20,000	50
HMDS	~ 12,000	51
Suspended	~ 230,000	15

Table. 1-4. .Summary of previous studies on mobility of graphene with different substrate.^{15,50,51}

1.3.3. Grain boundary scattering

The CVD graphene grown on Cu results in polycrystalline nature by forming grain boundaries, which are structural defects, when merged between grains due to random nucleation and growth, as shown in **figure 1-15**. It was confirmed by comparing the resistivity of inter-grain and intra-grain that the resulting graphene grain boundary deteriorates the electrical properties.⁵² It was confirmed that this decrease in electrical properties is due to the decrease in mobility due to scattering in the graphene grain boundary.⁵³ Therefore, the CVD synthesis methods to improve the quality of graphene have been focused on reducing grain boundary by enlarging grain size. The results of large-sized graphene grains by varying the growth parameter are summarized in **table 1-5**. Efforts to increase grain size can be explained by two major principles: reducing nucleation sites or stitching of grains with the same orientation.

The nucleation density of graphene was decreased by reducing the hydrocarbon supply.⁵⁴ Since the rough surface of Cu causes heterogeneous nucleation, the graphene particle size was increased to 1.2mm by smoothing the Cu surface through long pre-annealing.⁵⁵ In addition, by reducing the catalytic region of Cu through deliberate oxidation, the grain size was increased beyond the mm scale. In order to grow single-crystal graphene, Xu *et al.*, grow the graphene on single crystal Cu (111).⁵⁶ They found that graphene epitaxially grows on Cu (111) orientation. By stitching the average grain size of 200 μm aligned graphene, they grow single-crystalline graphene. In addition, our group grew uniform graphene grains on liquid Cu. Owing to the self-assembly behavior of hexagonal graphene flakes with aligned orientation and to the possibility of forming a single grain of graphene through a commensurate growth of these graphene flakes.⁵⁷

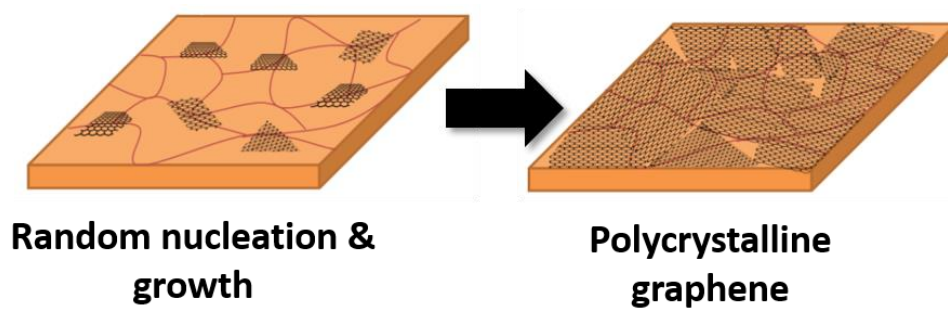


Figure. 1-15. Schematic of random nucleation and growth CVD graphene on Cu.

Method	Principles	Grain size	Ref. No.
Longtime pre-annealing	Removing nucleation site	1.2 mm	55
Reducing C supply	Removing nucleation site	2.3 mm	54
Oxidized Cu	Removing nucleation site	10 mm	58
Oxidized Cu + H ₂	Removing nucleation site	5 mm	53
Resolidification Cu	Removing nucleation site	1mm	59
On Cu (111)	Same orientation	200 μm	56
On liquid Cu	Same orientation	50 μm	57

Table. 1-5. .Summary of previous studies on enlarging grain size methods.⁵³⁻⁵⁹

References

1. Boehm, H. P.; Setton, R.; Stumpp, E., Nomenclature and Terminology of Graphite-Intercalation Compounds. *Carbon* **1986**, *24* (2), 241-245.
2. Wallace, P. R., The Band Theory of Graphite. *Phys Rev* **1947**, *71* (7), 476-476.
3. Lu, X. K.; Yu, M. F.; Huang, H.; Ruoff, R. S., Tailoring graphite with the goal of achieving single sheets. *Nanotechnology* **1999**, *10* (3), 269-272.
4. Zhang, Y. B.; Small, J. P.; Pontius, W. V.; Kim, P., Fabrication and electric-field-dependent transport measurements of mesoscopic graphite devices. *Appl Phys Lett* **2005**, *86* (7).
5. Novoselov, K. S.; Geim, A. K.; Morozov, S. V.; Jiang, D.; Zhang, Y.; Dubonos, S. V.; Grigorieva, I. V.; Firsov, A. A., Electric field effect in atomically thin carbon films. *Science* **2004**, *306* (5696), 666-669.
6. Blake, P.; Hill, E. W.; Castro Neto, A. H.; Novoselov, K. S.; Jiang, D.; Yang, R.; Booth, T. J.; Geim, A. K., Making graphene visible. *Appl Phys Lett* **2007**, *91* (6).
7. Berry, V., Impermeability of graphene and its applications. *Carbon* **2013**, *62*, 1-10.
8. Reich, S.; Maultzsch, J.; Thomsen, C.; Ordejon, P., Tight-binding description of graphene. *Phys Rev B* **2002**, *66* (3).
9. Castro Neto, A. H.; Guinea, F.; Peres, N. M. R.; Novoselov, K. S.; Geim, A. K., The electronic properties of graphene. *Rev Mod Phys* **2009**, *81* (1), 109-162.
10. Ando, T., The electronic properties of graphene and carbon nanotubes. *Npg Asia Mater* **2009**, *1* (1), 17-21.

11. Zhao, Q. Z.; Nardelli, M. B.; Bernholc, J., Ultimate strength of carbon nanotubes: A theoretical study. *Phys Rev B* **2002**, *65* (14).
12. Lee, C.; Wei, X. D.; Kysar, J. W.; Hone, J., Measurement of the elastic properties and intrinsic strength of monolayer graphene. *Science* **2008**, *321* (5887), 385-388.
13. Balandin, A. A.; Ghosh, S.; Bao, W. Z.; Calizo, I.; Teweldebrhan, D.; Miao, F.; Lau, C. N., Superior thermal conductivity of single-layer graphene. *Nano Lett* **2008**, *8* (3), 902-907.
14. Nair, R. R.; Blake, P.; Grigorenko, A. N.; Novoselov, K. S.; Booth, T. J.; Stauber, T.; Peres, N. M. R.; Geim, A. K., Fine structure constant defines visual transparency of graphene. *Science* **2008**, *320* (5881), 1308-1308.
15. Bolotin, K. I.; Sikes, K. J.; Jiang, Z.; Klima, M.; Fudenberg, G.; Hone, J.; Kim, P.; Stormer, H. L., Ultrahigh electron mobility in suspended graphene. *Solid State Commun* **2008**, *146* (9-10), 351-355.
16. Bolotin, K. I.; Sikes, K. J.; Hone, J.; Stormer, H. L.; Kim, P., Temperature-dependent transport in suspended graphene. *Phys Rev Lett* **2008**, *101* (9).
17. Bae, S.; Kim, S. J.; Shin, D.; Ahn, J. H.; Hong, B. H., Towards industrial applications of graphene electrodes. *Phys Scripta* **2012**, *T146*.
18. Lee, Y.; Bae, S.; Jang, H.; Jang, S.; Zhu, S. E.; Sim, S. H.; Song, Y. I.; Hong, B. H.; Ahn, J. H., Wafer-Scale Synthesis and Transfer of Graphene Films. *Nano Lett* **2010**, *10* (2), 490-493.
19. Bae, S.; Kim, H.; Lee, Y.; Xu, X. F.; Park, J. S.; Zheng, Y.; Balakrishnan, J.; Lei, T.; Kim, H. R.; Song, Y. I.; Kim, Y. J.; Kim, K. S.; Ozyilmaz, B.; Ahn, J. H.; Hong, B. H.; Iijima, S., Roll-to-roll

- production of 30-inch graphene films for transparent electrodes. *Nat Nanotechnol* **2010**, 5 (8), 574-578.
20. Eda, G.; Fanchini, G.; Chhowalla, M., Large-area ultrathin films of reduced graphene oxide as a transparent and flexible electronic material. *Nat Nanotechnol* **2008**, 3 (5), 270-274.
 21. Li, X. S.; Cai, W. W.; An, J. H.; Kim, S.; Nah, J.; Yang, D. X.; Piner, R.; Velamakanni, A.; Jung, I.; Tutuc, E.; Banerjee, S. K.; Colombo, L.; Ruoff, R. S., Large-Area Synthesis of High-Quality and Uniform Graphene Films on Copper Foils. *Science* **2009**, 324 (5932), 1312-1314.
 22. Berger, C.; Song, Z. M.; Li, X. B.; Wu, X. S.; Brown, N.; Naud, C.; Mayou, D.; Li, T. B.; Hass, J.; Marchenkov, A. N.; Conrad, E. H.; First, P. N.; de Heer, W. A., Electronic confinement and coherence in patterned epitaxial graphene. *Science* **2006**, 312 (5777), 1191-1196.
 23. Kim, K. S.; Zhao, Y.; Jang, H.; Lee, S. Y.; Kim, J. M.; Kim, K. S.; Ahn, J. H.; Kim, P.; Choi, J. Y.; Hong, B. H., Large-scale pattern growth of graphene films for stretchable transparent electrodes. *Nature* **2009**, 457 (7230), 706-710.
 24. Kwon, S. Y.; Ciobanu, C. V.; Petrova, V.; Shenoy, V. B.; Baren, J.; Gambin, V.; Petrov, I.; Kodambaka, S., Growth of Semiconducting Graphene on Palladium. *Nano Lett* **2009**, 9 (12), 3985-3990.
 25. Sutter, P. W.; Flege, J. I.; Sutter, E. A., Epitaxial graphene on ruthenium. *Nat Mater* **2008**, 7 (5), 406-411.
 26. Coraux, J.; N'Diaye, A. T.; Busse, C.; Michely, T., Structural coherency of graphene on Ir(111). *Nano Lett* **2008**, 8 (2), 565-570.
 27. Li, X. S.; Cai, W. W.; Colombo, L.; Ruoff, R. S., Evolution of Graphene

- Growth on Ni and Cu by Carbon Isotope Labeling. *Nano Lett* **2009**, *9* (12), 4268-4272.
28. Yu, Q. K.; Lian, J.; Siriponglert, S.; Li, H.; Chen, Y. P.; Pei, S. S., Graphene segregated on Ni surfaces and transferred to insulators. *Appl Phys Lett* **2008**, *93* (11).
 29. Goniszewski, S.; Gallop, J.; Adabi, M.; Gajewski, K.; Shaforost, O.; Klein, N.; Sierakowski, A.; Chen, J.; Chen, Y. F.; Gotszalk, T.; Hao, L., Self-supporting graphene films and their applications. *Iet Circ Device Syst* **2015**, *9* (6), 420-427.
 30. Gao, T. C.; Li, Z. T.; Huang, P. S.; Shenoy, G. J.; Parobek, D.; Tan, S. S.; Lee, J. K.; Liu, H. T.; Lee, P. W., Hierarchical Graphene/Metal Grid Structures for Stable, Flexible Transparent Conductors. *Acs Nano* **2015**, *9* (5), 5440-5446.
 31. Pham, V. P.; Kim, K. N.; Jeon, M. H.; Kim, K. S.; Yeom, G. Y., Cyclic chlorine trap-doping for transparent, conductive, thermally stable and damage-free graphene. *Nanoscale* **2014**, *6* (24), 15301-15308.
 32. Wu, W.; Yu, Q. K.; Peng, P.; Liu, Z. H.; Bao, J. M.; Pei, S. S., Control of thickness uniformity and grain size in graphene films for transparent conductive electrodes. *Nanotechnology* **2012**, *23* (3).
 33. Yoon, J.; Sung, H.; Lee, G.; Cho, W.; Ahn, N.; Jung, H. S.; Choi, M., Superflexible, high-efficiency perovskite solar cells utilizing graphene electrodes: towards future foldable power sources. *Energ Environ Sci* **2017**, *10* (1), 337-345.
 34. Zhang, J.; Hu, P. A.; Wang, X. N.; Wang, Z. L.; Liu, D. Q.; Yang, B.; Cao, W. W., CVD growth of large area and uniform graphene on tilted copper

- foil for high performance flexible transparent conductive film. *J Mater Chem* **2012**, 22 (35), 18283-18290.
35. Kwon, K. C.; Ham, J.; Kim, S.; Lee, J. L.; Kim, S. Y., Eco-friendly graphene synthesis on Cu foil electroplated by reusing Cu etchants. *Sci Rep-Uk* **2014**, 4.
 36. Barin, G. B.; Song, Y.; Gimenez, I. D.; Souza, A. G.; Barretto, L. S.; Kong, J., Optimized graphene transfer: Influence of polymethylmethacrylate (PMMA) layer concentration and baking time on graphene final performance. *Carbon* **2015**, 84, 82-90.
 37. Suk, J. W.; Lee, W. H.; Lee, J.; Chou, H.; Piner, R. D.; Hao, Y. F.; Akinwande, D.; Ruoff, R. S., Enhancement of the Electrical Properties of Graphene Grown by Chemical Vapor Deposition via Controlling the Effects of Polymer Residue. *Nano Lett* **2013**, 13 (4), 1462-1467.
 38. Levesque, P. L.; Sabri, S. S.; Aguirre, C. M.; Guillemette, J.; Siaj, M.; Desjardins, P.; Szkopek, T.; Martel, R., Probing Charge Transfer at Surfaces Using Graphene Transistors. *Nano Lett* **2011**, 11 (1), 132-137.
 39. D'Arsie, L.; Esconjauregui, S.; Weatherup, R. S.; Wu, X. Y.; Arter, W. E.; Sugime, H.; Cepek, C.; Robertson, J., Stable, efficient p-type doping of graphene by nitric acid. *Rsc Adv* **2016**, 6 (114), 113185-113192.
 40. Kwon, K. C.; Choi, K. S.; Kim, S. Y., Increased Work Function in Few-Layer Graphene Sheets via Metal Chloride Doping. *Adv Funct Mater* **2012**, 22 (22), 4724-4731.
 41. Kim, H. H.; Yang, J. W.; Jo, S. B.; Kang, B.; Lee, S. K.; Bong, H.; Lee, G.; Kim, K. S.; Cho, K., Substrate-Induced Solvent Intercalation for Stable Graphene Doping. *Acs Nano* **2013**, 7 (2), 1155-1162.

42. Kim, Y.; Ryu, J.; Park, M.; Kim, E. S.; Yoo, J. M.; Park, J.; Kang, J. H.; Hong, B. H., Vapor-Phase Molecular Doping of Graphene for High-Performance Transparent Electrodes. *Acs Nano* **2014**, 8 (1), 868-874.
43. Jo, K.; Kim, S. M.; Lee, S. M.; Kim, J. H.; Lee, H. J.; Kim, K. S.; Kwon, Y. D.; Kim, K. S., One-step etching, doping, and adhesion-control process for graphene electrodes. *Carbon* **2015**, 82, 168-175.
44. Kim, S. J.; Ryu, J.; Son, S.; Yoo, J. M.; Park, J. B.; Won, D.; Lee, E. K.; Cho, S. P.; Bae, S.; Cho, S.; Hong, B. H., Simultaneous Etching and Doping by Cu-Stabilizing Agent for High-Performance Graphene-Based Transparent Electrodes. *Chem Mater* **2014**, 26 (7), 2332-2336.
45. Kim, M.; Nabeya, S.; Han, S. M.; Kim, M. S.; Lee, S.; Kim, H. M.; Cho, S. Y.; Lee, D. J.; Kim, S. H.; Kim, K. B., Selective Atomic Layer Deposition of Metals on Graphene for Transparent Conducting Electrode Application. *Acs Appl Mater Inter* **2020**, 12 (12), 14331-14340.
46. Kim, K.; Lee, H. B. R.; Johnson, R. W.; Tanskanen, J. T.; Liu, N.; Kim, M. G.; Pang, C.; Ahn, C.; Bent, S. F.; Bao, Z. N., Selective metal deposition at graphene line defects by atomic layer deposition. *Nat Commun* **2014**, 5.
47. Kim, M.; Kim, K. J.; Lee, S. J.; Kim, H. M.; Cho, S. Y.; Kim, M. S.; Kim, S. H.; Kim, K. B., Highly Stable and Effective Doping of Graphene by Selective Atomic Layer Deposition of Ruthenium. *Acs Appl Mater Inter* **2017**, 9 (1), 701-709.
48. Chen, J. H.; Jang, C.; Xiao, S. D.; Ishigami, M.; Fuhrer, M. S., Intrinsic and extrinsic performance limits of graphene devices on SiO₂. *Nat Nanotechnol* **2008**, 3 (4), 206-209.

49. Kim, S. J.; Park, B.; Noh, S. H.; Yoon, H. S.; Oh, J.; Yoo, S.; Kang, K.; Han, B.; Jun, S. C., Carrier scattering in quasi-free standing graphene on hexagonal boron nitride. *Nanoscale* **2017**, 9 (41), 15934-15944.
50. Dean, C. R.; Young, A. F.; Meric, I.; Lee, C.; Wang, L.; Sorgenfrei, S.; Watanabe, K.; Taniguchi, T.; Kim, P.; Shepard, K. L.; Hone, J., Boron nitride substrates for high-quality graphene electronics. *Nat Nanotechnol* **2010**, 5 (10), 722-726.
51. Lafkioti, M.; Krauss, B.; Lohmann, T.; Zschieschang, U.; Klauk, H.; von Klitzing, K.; Smet, J. H., Graphene on a Hydrophobic Substrate: Doping Reduction and Hysteresis Suppression under Ambient Conditions. *Nano Lett* **2010**, 10 (4), 1149-1153.
52. Yu, Q. K.; Jauregui, L. A.; Wu, W.; Colby, R.; Tian, J. F.; Su, Z. H.; Cao, H. L.; Liu, Z. H.; Pandey, D.; Wei, D. G.; Chung, T. F.; Peng, P.; Guisinger, N. P.; Stach, E. A.; Bao, J. M.; Pei, S. S.; Chen, Y. P., Control and characterization of individual grains and grain boundaries in graphene grown by chemical vapour deposition. *Nat Mater* **2011**, 10 (6), 443-449.
53. Zhou, H. L.; Yu, W. J.; Liu, L. X.; Cheng, R.; Chen, Y.; Huang, X. Q.; Liu, Y.; Wang, Y.; Huang, Y.; Duan, X. F., Chemical vapour deposition growth of large single crystals of monolayer and bilayer graphene. *Nat Commun* **2013**, 4.
54. Yan, Z.; Lin, J.; Peng, Z. W.; Sun, Z. Z.; Zhu, Y.; Li, L.; Xiang, C. S.; Samuel, E. L.; Kittrell, C.; Tour, J. M., Toward the Synthesis of Wafer-Scale Single-Crystal Graphene on Copper Foils. *Acs Nano* **2012**, 6 (10), 9110-9117.
55. Wang, H.; Wang, G. Z.; Bao, P. F.; Yang, S. L.; Zhu, W.; Xie, X.;

- Zhang, W. J., Controllable Synthesis of Submillimeter Single-Crystal Monolayer Graphene Domains on Copper Foils by Suppressing Nucleation (vol 134, pg 3627, 2012). *J Am Chem Soc* **2012**, 134 (44), 18476-18476.
56. Xu, X. Z.; Zhang, Z. H.; Dong, J. C.; Yi, D.; Niu, J. J.; Wu, M. H.; Lin, L.; Yin, R. K.; Li, M. Q.; Zhou, J. Y.; Wang, S. X.; Sun, J. L.; Duan, X. J.; Gao, P.; Jiang, Y.; Wu, X. S.; Peng, H. L.; Ruoff, R. S.; Liu, Z. F.; Yu, D. P.; Wang, E. G.; Ding, F.; Liu, K. H., Ultrafast epitaxial growth of metre-sized single-crystal graphene on industrial Cu foil. *Sci Bull* **2017**, 62 (15), 1074-1080.
57. Cho, S. Y.; Kim, M. S.; Kim, M.; Kim, K. J.; Kim, H. M.; Lee, D. J.; Lee, S. H.; Kim, K. B., Self-assembly and continuous growth of hexagonal graphene flakes on liquid Cu. *Nanoscale* **2015**, 7 (30), 12820-12827.
58. Hao, Y. F.; Bharathi, M. S.; Wang, L.; Liu, Y. Y.; Chen, H.; Nie, S.; Wang, X. H.; Chou, H.; Tan, C.; Fallahazad, B.; Ramanarayan, H.; Magnuson, C. W.; Tutuc, E.; Yakobson, B. I.; McCarty, K. F.; Zhang, Y. W.; Kim, P.; Hone, J.; Colombo, L.; Ruoff, R. S., The Role of Surface Oxygen in the Growth of Large Single-Crystal Graphene on Copper. *Science* **2013**, 342 (6159), 720-723.
59. Mohsin, A.; Liu, L.; Liu, P. Z.; Deng, W.; Ivanov, I. N.; Li, G. L.; Dyck, O. E.; Duscher, G.; Dunlap, J. R.; Xiao, K.; Gu, G., Synthesis of Millimeter-Size Hexagon-Shaped Graphene Single Crystals on Resolidified Copper. *Acs Nano* **2013**, 7 (10), 8924-8931.

CHAPTER 2.

Graphene grain boundary visualization by Cu oxidation

This chapter is based on the paper published in
RSC advances **10**, 35671-35680, (2020).

2.1. Introduction

Since the experimental discovery of graphene by the scotch-tape method in 2004,¹ high-quality single-layer graphene has been grown from various hydrocarbon precursors by chemical vapor deposition (CVD) on Cu film. As a metal catalyst for the CVD process,^{2,3} Cu foil not only dissociates hydrocarbon precursors but also self-limits the growth of graphene by its extremely low solubility for carbon.^{2,4} Nevertheless, under the random nucleation and growth process of CVD, the graphene layer has a polycrystalline nature on the Cu surface. The graphene grain boundaries (G-GBs) inherently inhibit charge transport, severely degrading the mobility of charge carriers.⁵⁻⁸ Moreover, the G-GBs significantly affect other physical properties including, the mechanical strength and gas-molecule impermeability of graphene.^{9,10} To grow a graphene layer with a large grain size, researchers have carefully tuned the graphene-growth conditions.¹¹⁻¹³ Furthermore, the characterization of the G-GBs, such as grain size linked to the physical properties of graphene, has been a major topic of concern.

Raman spectroscopy is among the most efficient characterization methods of graphene. The D peak (which appears at $\sim 1350\text{ cm}^{-1}$ on the Raman spectrum) represents the breakage of the sp^2 bond by structural defects in the graphene lattice.¹⁴ Raman spectroscopy provides various quantitative information of graphene, such as the number of graphene layers (from the intensity ratio of the G and D peaks) and doping amount (from the shift of the G or 2D peak).¹⁵⁻¹⁷ However, Raman spectroscopy cannot provide information over the entire sample area because the laser beam size is limited to a few μm^2 . Furthermore, the graphene must be

transferred to a SiO₂ substrate for accurate analysis. Transmission electron microscopy (TEM) is clearly advantageous because its atomic resolution enables direct observation of the graphene lattice.¹⁸ However, sample preparation is quite difficult, and the observed area is extremely small. The measurement of the electrical properties of graphene requires the transfer of graphene on the insulating substrate for fabricating a device. Because various defects (*e.g.*, wrinkles, cracks, holes, and organic residues) are introduced during the transfer process,¹⁹ the measured property cannot be correlated with the quality of the as-grown graphene. Therefore, a method for the analysis of the as-grown graphene on Cu is required for proper tuning of the graphene-growth condition.

In this respect, the oxidation of Cu underlying graphene has been proposed by several researchers as a useful method to simply observe the graphene grain.²⁰⁻²⁶ Because the hexagonal arrangement of carbon atoms in graphene is sufficiently compact to inhibit the penetration of oxygen (and consequently the oxidation of Cu),²⁷ Cu is selectively oxidized by oxidizing species, such as OH⁻ or O⁻, which penetrate the G-GBs.²²⁻²⁴ These radicals are typically dissociated from H₂O at elevated temperatures (approximately 200°C) or under UV exposure.^{23,24} Energy calculations using density functional theory and TEM observations have shown that oxygen radicals penetrate the G-GBs without bond breaking. Oxygens penetrating the boundary at room temperature was reported to form Cu oxide at the graphene–Cu interface.²⁵ Moreover, the lateral diffusion of oxygen at the graphene–Cu interface is hindered by van der Waals forces between the Cu and graphene.²⁶ Although the results of oxidation kinetics depend on the states of the graphene (*e.g.*, grain size, shape, and stitching between grains) and the Cu foil (*e.g.*, crystallographic orientation),²⁸ the oxidation of Cu through the grain boundary of the graphene layer

has not been systematically investigated. Furthermore, the extent to which Cu oxidation damages the electrical property of graphene is unknown.

Here, Cu oxidation through graphene was investigated as a function of temperature (180°C–240°C) and time (10–360 min). The oxidation kinetics of Cu through the G-GBs was determined based on the Cu oxide coverage that was quantitatively estimated from the optical microscope (OM) images. To investigate the effect of Cu oxidation on graphene quality, all graphene samples were transferred on a polyethylene terephthalate (PET) film and then the electrical properties (*i.e.*, sheet resistance, Hall mobility, and charge carrier density) of these samples were measured as a function of oxidation time and temperature by Hall measurement. We correlated the extent of Cu oxidation and electrical properties of graphene; these results enable the prediction of electrical properties through graphene visualization by Cu oxidation.

2.2. Experimental details

2.2.1. Synthesis of graphene

The graphene was synthesized by RTCVD (NPS Corporation) on a 370×470 -mm² Cu foil (thickness: 0.35 mm, Nippon Mining & Metals Corporation). The Cu foil was loaded into a chamber and heated to 800°C under CH₄ atmosphere (30 sccm, 550 mTorr). The surface of the Cu foil was then cleaned using pre-annealing, and the crystalline orientation of Cu was rearranged. Next, the graphene synthesis was performed by reheating the foil to 1025°C for 1000 s. The chamber was cooled down to 600°C and then to room temperature by injecting CH₄ and N₂ gases, respectively.

2.2.2. Cu oxidation on graphene/Cu foil structure

After the deposition, the graphene grown on Cu foil was cut into specimens of 3×3 cm², and the samples were subjected to heat treatment on a hot plate for different durations at various temperatures under the air atmosphere. Four different temperatures were chosen: 180°C, 200°C, 220°C, and 240°C. The oxidation time was varied from 10 to 360 min (Table 1).

2.2.3. Characterization of graphene and Cu oxide

After the oxidation of graphene on the Cu foil, surface images were acquired with OM (Olympus BX50). The cross-sectional microstructure of graphene on Cu after oxidation was observed using Cs-corrected TEM (ARM 200F, JEOL Ltd.). The as-grown and heat-treated graphenes on Cu were transferred on a polymethyl methacrylate (PMMA) supporting layer in order to investigate the electrical

properties of graphene. The PMMA was spin-coated onto the graphene on Cu and then the underlying Cu was wet etched in imidazole-based Cu etchant (ammonium persulfate (0.1 M) + H_2SO_4 + H_2O_2). Thus, the graphene was simultaneously doped during the etching of Cu.²⁹ The floated PMMA/graphene layer was scooped after 8 hours of complete Cu etching onto PET. Finally, the top PMMA layer was removed by acetone. The graphene electrical properties, *i.e.*, sheet resistance, Hall mobility, and sheet carrier density, were measured by using a van der Pauw structure of 8×8 mm². Hall measurements were performed under a 0.5-T magnetic field (HL 5500PC, BIO-RAD) at room temperature.

Temperature (°C)		Oxidation time (min)		
180	60	120	240	360
200	30	60	120	240
220	15	30	60	120
240	10	20	30	60

Table 2-1. Oxidation conditions of Cu coated by graphene

2.3. Results and discussion

2.3.1. Characterization of as-grown graphene

The single-layer graphene (SLG) was synthesized on the Cu foil by rapid thermal chemical vapor deposition (RTCVD) at 1025°C for 1000 s. As shown in **Figure 2-1**, no discernible features, *e.g.*, G-GB or other defects, were observed on the as-grown SLG film by the OM image analysis. The sheet resistance (R_s), sheet carrier density (n_s), and Hall mobility (μ) of the SLG transferred on the PET substrate were 254 $\Omega/\text{sq.}$, $1.5 \times 10^{13} \text{ \#}/\text{cm}^2$, and 1572 cm^2/Vs , respectively. The n_s of the as-grown SLG was found to be one order of magnitude higher than that of the pristine graphene (without intentional doping) because of the molecular p-type doping by the adsorption of imidazole during the wet etching of the Cu foil.²⁹

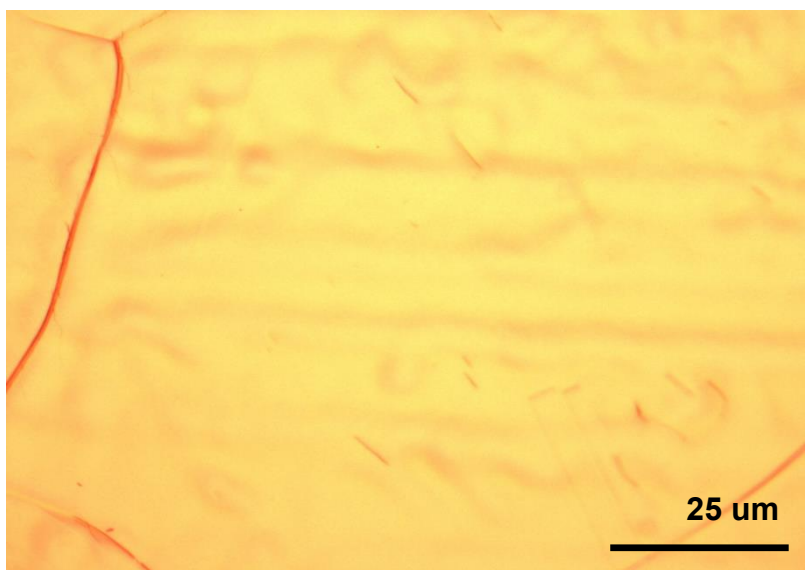


Figure 2-1. Optical microscope image of as-grown single-layer graphene on Cu foil. Except for the Cu grain boundaries, there is no optical contrast observed as graphene defects.

2.3.2. Selective oxidation of Cu at the graphene grain boundary

The as-grown SLG on Cu foil was heat-treated under air atmosphere to investigate the Cu oxidation behavior through the graphene. **Figure 2-2.** shows the OM images at each oxidation temperature (T_{ox}) and oxidation time (t_{ox}); **figure 2-2 (a–d)**, **figure 2-2(e–h)**, **figure 2-2(i–l)**, and **figure 2-2(m–p)** show the OM images at 180°C, 200°C, 220°C, and 240°C, respectively. Early heat-treated samples at 180°C/60 min, 200°C/30 min, and 220°C/15 min (Fig. 1(a), (e), and (i), respectively) show dark contrasts at the line expected with G-GBs. Upon increasing the t_{ox} , the dark contrasts not only delineate the grain boundaries of graphene (**figure 2-2(c)**, **(g)**, and **(j)**) but also increase their line width (**figure 2-2 (d)**, **(h)**, and **(k)**, respectively). Eventually, the bright area, presumed to be a graphene grain, is isolated, as shown in **figure 2-2(l)**. At 240°C, the graphene grain seems to isolate after exposure to air for 10 min and the size of the bright area decreases with increasing t_{ox} . Notably, some samples with similar oxidation morphologies, such as those treated at 180°C/240 min, 200°C/120 min, and 220°C/30 min that are illustrated in **figure 2-2(c)**, **(g)**, and **(j)**, respectively, show that the t_{ox} tends to decrease to half its value with T_{ox} by only 20°C. As shown in **figure 2-3**, EDS mapping image of the sample oxidized at 220 °C for 1 hour clearly shows that a large amount of oxygen detected in a dark area in the OM image which indicates the dark area is Cu oxide. Previous reports^{23,24} on the composition analysis of Cu oxidation under graphene using TEM also suggested that the dark contrast in OM images corresponds to Cu oxide. Therefore, the Cu oxidation, dark contrasts on OM image, begins at the G-GBs and progresses to the periphery of the G-GBs.

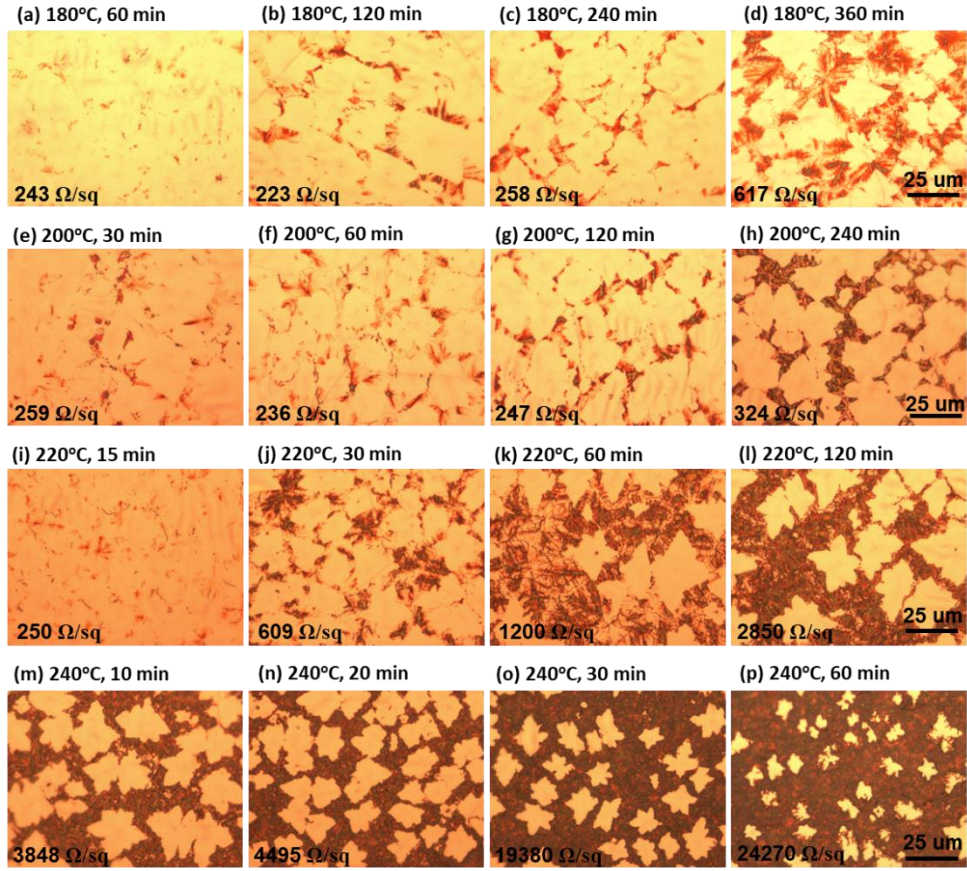


Figure. 2-2. OM images of the as-grown graphene after the oxidation at (a)–(d) 180°C, (e)–(h) 200°C, (i)–(l) 220°C, and (m)–(p) 240°C

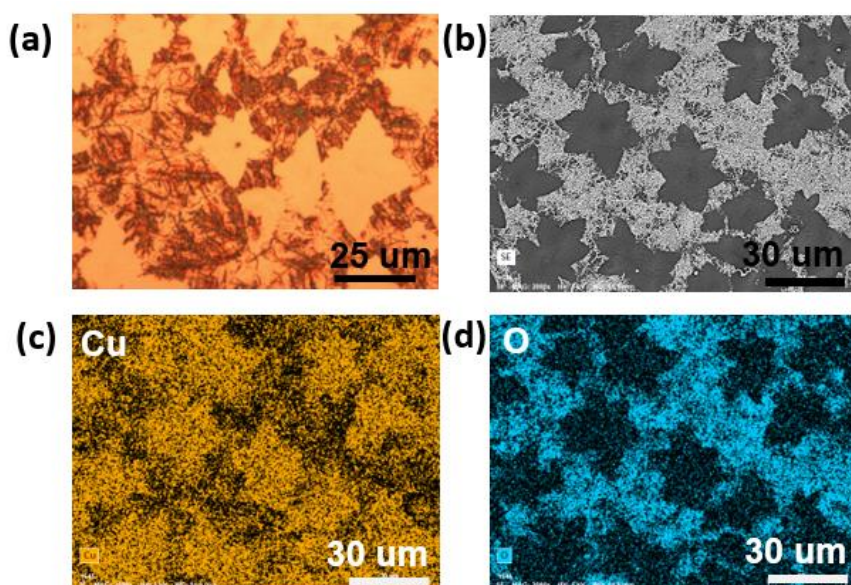


Figure. 2-3. (a) Optical microscopy image and (b) SEM image of sample oxidized at 220 °C for 1 hour. EDS mapping image of (b), representing Cu (c) and O (d) element, respectively.

2.3.3. Cu oxidation mechanism

The dark area in the sample oxidized at 200°C for 120 min was analyzed using cross-sectional TEM (**Figure 2-4**). The cross-sectional TEM samples were prepared perpendicular to the dark lines. Bright-field scanning TEM (STEM) revealed a radially grown morphology on the flat Cu surface (**Figure. 2-4(a)**). From the indexing of the selected area diffraction pattern (**Figure. 2-4(c)**) and composition analysis of energy dispersive spectroscopy (EDS, **Figure. 2-4(e)**), the species was determined as Cu₂O (space group: $Pn\bar{3}m$, $a = 4.288 \text{ \AA}$). Judging from the low contrast in the high-angle annular dark field (HAADF) STEM images (**Figure. 2-4(b)**), the Cu₂O had a lower mass density than the Cu substrate. Therefore, the interface between Cu₂O and Cu was very clearly defined. The high resolution TEM (HRTEM) images in this area clarified the graphene layer at the Cu–Cu₂O interface with an opening at the center (marked by arrows in **Figure. 2-4(d)**). The graphene layer was also found under other Cu₂O particles (see **Figure. 2-5**). The semi-circular shape of the Cu₂O and graphene opening at the center of the interface indicate that Cu₂O is formed from a point source of Cu. Furthermore, graphene existence between Cu₂O and Cu evidenced that the Cu₂O grew by out-diffusion of Cu.³⁰ Indeed, Cu oxidation predominantly occurs by the diffusion of Cu cations through Cu oxide.^{31,32} However, these results contradict a few previous reports, which claim that Cu₂O nucleates and grows by oxygen in-diffusion through graphene at the graphene–Cu interface.^{23,24} According to these previous reports, oxygen atoms dissociate from H₂O at the graphene vacancies and GBs then penetrate the G-GBs and form Cu₂O at the graphene–Cu interface.²⁴ The randomly oriented and shaped graphene grains are stitched together, forming abundant pentagon, heptagon, and other non-hexagonal carbon rings at the G-GBs.³³ G-GBs with imperfect stitching and voids would crack

during the CVD process. We believe that Cu_2O nucleation was promoted at the non-hexagonal carbon rings or in the imperfect-stitching region of G-GBs but was suppressed at the relatively stable grain boundary. For instance, at 180°C after 240 min of oxidation, the line width of the grown Cu_2O reached $10\text{ }\mu\text{m}$ (**Figure. 2-2(c)**), and these locations are considered as the non-hexagonal carbon rings or imperfect-stitching; however, at certain G-GBs where relatively stable G-GBs, still no Cu_2O was formed. We surmise that the initial nucleation process of Cu_2O was generated by oxygen in-diffusion through the G-GBs as previously reported but that Cu_2O grew by the dominant out-diffusion of Cu cations at the G-GBs. **Figure. 2-4(f)** shows the schematic sequence of Cu oxidation through graphene based on the results of the current study. During the oxidation, Cu oxide was initially formed at G-GB and further growth was proceeded by out-diffusion of Cu through the Cu oxide. Otherwise, if Cu oxide growth was proceeded by in-diffusion of oxygen to G-GBs, not by out-diffusion of Cu cation, Cu oxide would be encapsulated by the graphene layer. Consequently, the graphene layer undergoes tensile stress generated by 1.7 times of volume expansion during Cu oxide formation, and the estimated strain of graphene is about 80% based on Fig 3(a). Considering fracture occurs on PMMA and PDMS supported graphene only about 8% of strain during the tensile test,^{34,35} it seems impossible to survive graphene without fracture during Cu oxide formation. However, no significant R_s change is observed even if almost G-GBs have been decorated by Cu_2O (**Figure. 2-2(c)**, (g), and (i)). Moreover, few samples of graphene seem to be isolated by grown Cu_2O , but the measured R_s shows that graphene samples are still electrically connected (**Figure. 2-2** (d), (h), (k), and (m)) Therefore, Cu oxide growth

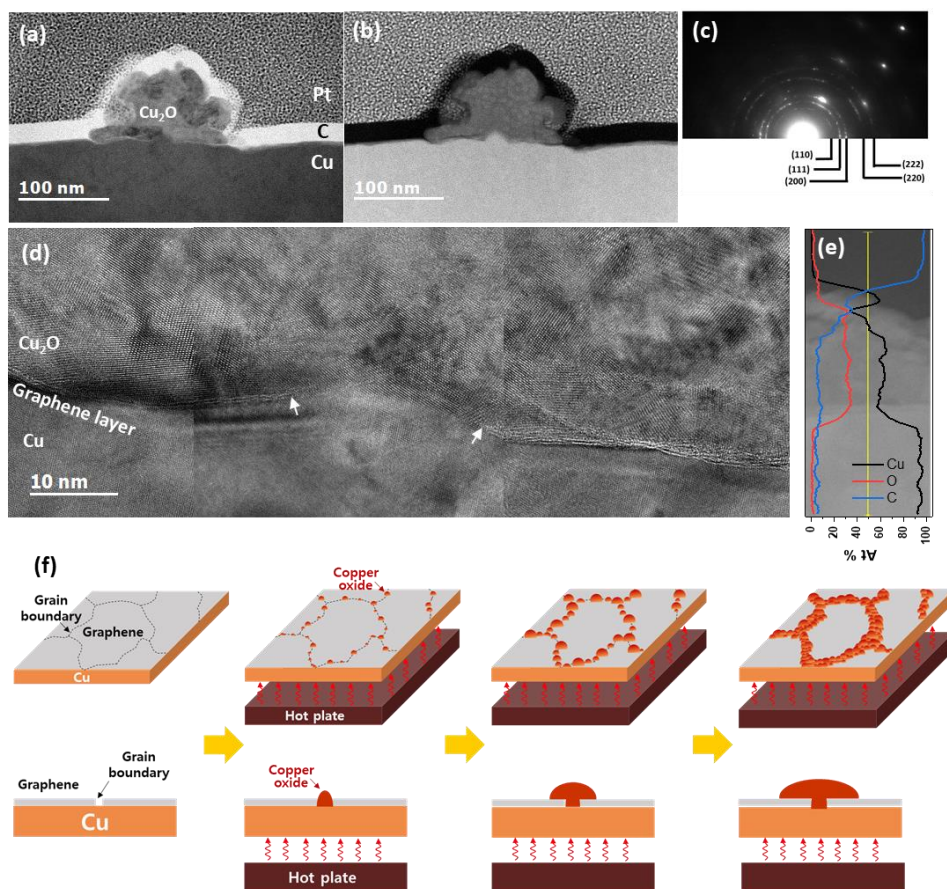


Figure. 2-4. Cross-sectional TEM images and EDS analysis (a) bright-field STEM image, (b) HAADF STEM image, (c) SADP of Cu₂O, (d) HRTEM image, (e) EDS line spectrum across the interface between Cu and Cu₂O, and (f) schematic diagrams of Cu oxidation through graphene grain boundary

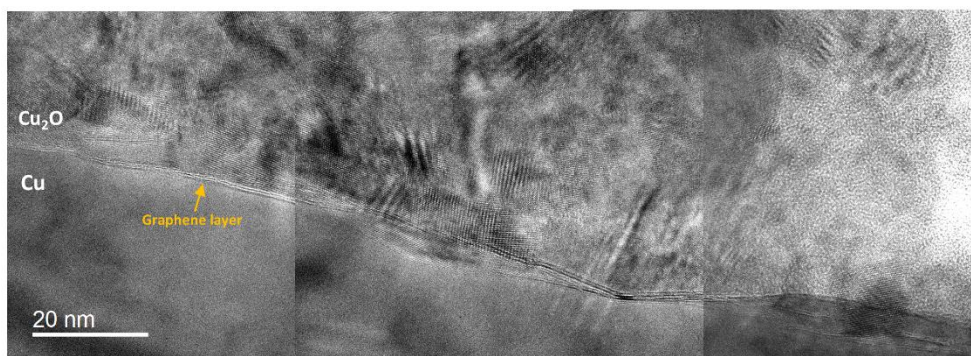


Figure. 2-5. Cross-sectional HRTEM image at the interface between Cu and Cu₂O

2.3.4. Cu oxide growth kinetics

The surface coverage of Cu₂O (F_{ox}) was assessed based on the OM images in Fig. 1. Here, the intensity of the OM image was normalized and the fraction of dark regions was estimated from the intensity histogram (for more details refer to **figure 2-6**). **Figure 2-7(a)** shows the F_{ox} as a function of t_{ox} and T_{ox} . It is worth noting that the change in the F_{ox} as a function of t_{ox} agrees well with the typical Johnson–Mehl–Avrami–Kolmogorov (JMAK) equation [Eq. (2-1)] for predicting phase transformation kinetics based on nucleation and growth.^{36,37}

$$F = 1 - \exp(-kt^n), \quad \text{Eq. (2-1)}$$

where F is the fraction of the transformed phase, t is the transformation time, n is the shape factor, and k is the kinetic parameter related to the transformation rate. n is related to the nucleation and growth dimension. If the phase change occurs by nucleation and three-dimensional growth, n has a value of approximately 4. If there is no further nucleation during the growth, i.e., nucleation is not a function of time, n has the same value as the shape dimension. And n has a value of about 3 for three-dimensional growth. In our case, the n value was well fitted to 1 at all T_{ox} , which is shown as solid lines in **figure 2-7(a)**. It means that the nuclei of Cu₂O were formed at the fixed region of G-GBs, and Cu₂O grows one-dimensionally from the G-GBs without additional nucleation. The one-dimensional growth of Cu₂O is well matched experimental result in **figure 2-2** and previous discussions that nucleation of Cu₂O is limited at the non-hexagonal carbon rings or imperfect-stitching region and further nucleation of Cu₂O is suppressed. Here, only 2-dimensional growth was considered with no information on the thickness change because the F_{ox} is the surface coverage. Therefore, because the length of G-GB is fixed, one-dimensional growth implies an increase in the width of Cu oxide from G-GBs.

Furthermore, the k value related to the transformation rate was also extracted based on the JMAK equation in Fig. 3(a) and is plotted as a function of $1/T_{\text{ox}}$ in Fig. 3(b). The slope of the curve fitted by Arrhenius equation was 1.54 eV, which reflects the activation energy of Cu_2O growth through graphene, representing the lateral growth rate of Cu_2O . Therefore, the growth of Cu_2O through graphene is controlled by Cu out-diffusion through Cu_2O because this activation energy is similar to that of Cu diffusion in Cu oxide estimated in the classical Cu oxidation experiment.³⁸ Consequently, it is possible to predict the kinetics of Cu oxidation through graphene at a certain targeting temperature through the JMAK equation using a k value obtained by extrapolation.

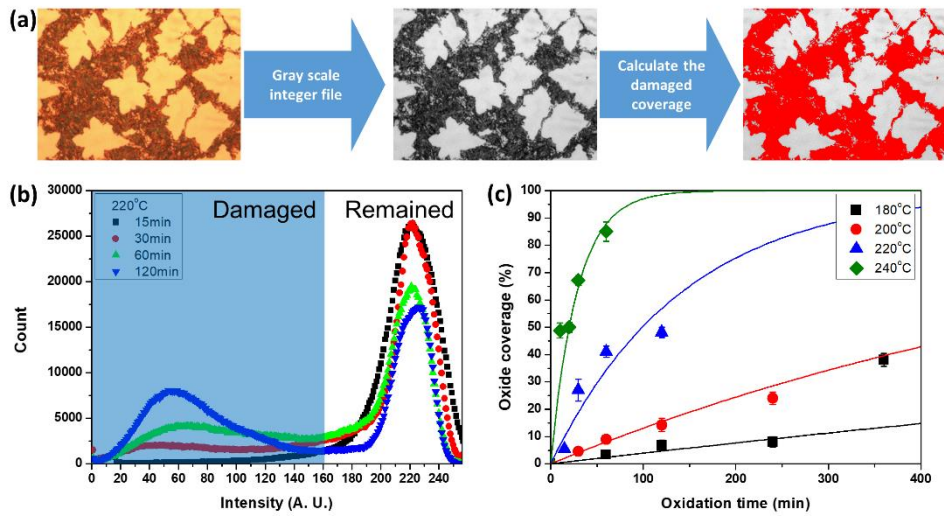


Figure. 2-6. (a) RGB colored optical image file is converted to an integer file with 256-gray scale. (b) The count of damaged pixels is extracted from the intensity histogram and (c) it is divided by the total number of pixels to obtain the oxide coverage.

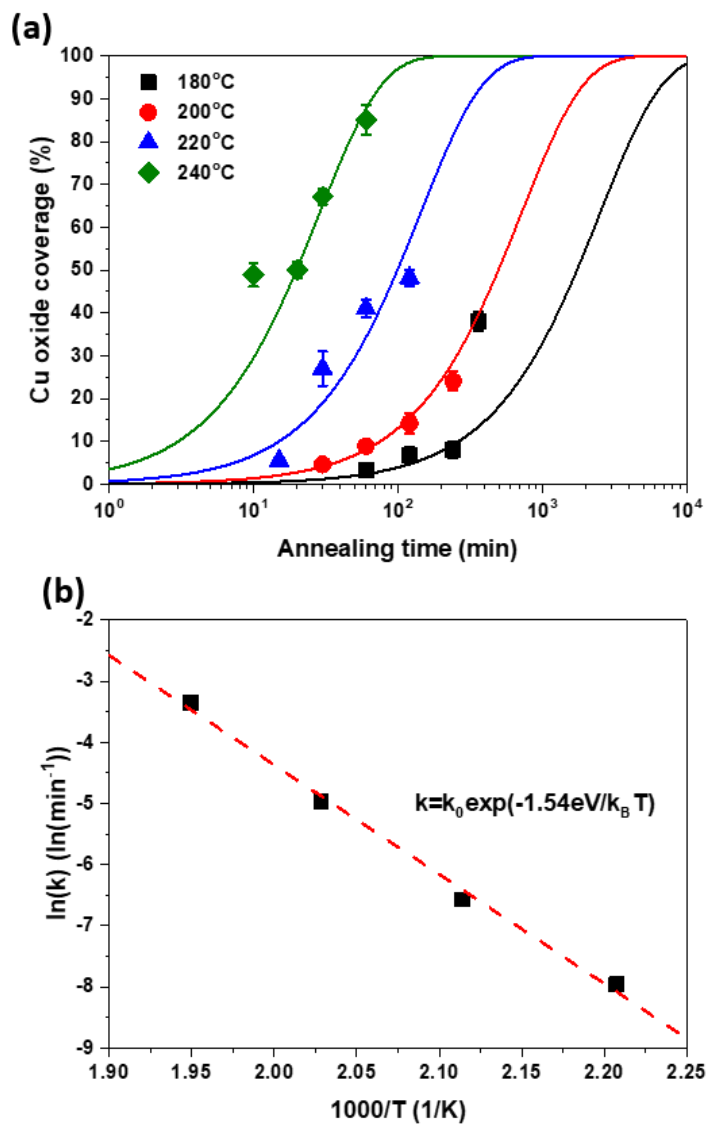


Figure. 2-7. (a) Cu oxide coverage as a function of oxidation time and (b) oxidation reaction constant as a function of inverse oxidation temperature.

2.3.5. Electrical properties of graphene based on Cu oxidation

Previous results showed that Cu oxide grows on the graphene surface by out-diffusion of Cu ions through Cu oxide. To investigate the quality change in the graphene during Cu oxidation, the electrical properties of all samples were measured. All oxidized samples, as shown in **figure 2-2**, were transferred on a PET film; then, the sheet resistance of graphene (R_s) was examined by Hall measurement using the van der Pauw structure. The change in R_s as a function of t_{ox} at each T_{ox} is illustrated in **figure 2-8(a)**. At T_{ox} of 180°C, 200°C, and 220°C, the R_s values did not significantly increase compared to those of the as-grown graphene ($R_{s0} = 254 \Omega/\text{sq.}$) until 240, 120, and 15 min of oxidation, respectively. However, at T_{ox} of 240°C, R_s sharply increased after only 10 min of oxidation. To determine the cause of the change in R_s , the carrier concentration (n_s) and Hall mobility (μ) were measured as a function of t_{ox} by Hall measurement (**figure 2-8(b)** and **(c)**). Interestingly, n_s maintains a value of $1.5 \times 10^{13} \text{ \#}/\text{cm}^2$, regardless of T_{ox} and t_{ox} . However, there was a drastic change in μ (**figure 2-8(c)**).

Because the electrical properties depend on both T_{ox} and t_{ox} , it is difficult to quantitatively determine the effect of Cu oxidation on the electrical properties of graphene. Therefore, by expressing T_{ox} and t_{ox} in terms of F_{ox} , the electrical properties of graphene were plotted as a function of F_{ox} (**figure 2-9**), in which the dashed lines represent the values of the as-grown graphene. As mentioned, n_s was independent of T_{ox} and t_{ox} and remained constant until $F_{ox} = 85\%$ (**figure 2-9(b)**). The R_s and μ had different curves for each T_{ox} , but these curves were merged into one curve by plotting it as a function of F_{ox} . It clearly indicates that the electrical properties of graphene are strongly related to F_{ox} . From $R_s = 1/n_s q \mu$, the change in R_s as a function of F_{ox} is fully described by the change of μ , inversely

corresponding to the change of μ , because of the constant n_s . The change in μ as a F_{ox} is divided into three regions. In the first region (under $F_{ox} = 15\%$), the value of μ stayed at the as-grown value, and then the value of μ decreases linearly with the increase in F_{ox} in the second region ($F_{ox} = 15\% - 50\%$). Finally, the value of μ was only a few tens of cm^2/Vs over $F_{ox} = 50\%$. Herein, Cu_2O is formed on the graphene surface and hence is undamaged by volume expansion (1.7 times) from Cu to Cu_2O . However, as a defect site of the G-GB, the initial Cu_2O nucleation site is the pathway of Cu cation out-diffusion (see the HRTEM image in **figure 2-4(d)**). The initial nucleation site is considered as a degraded G-GB point even before the Cu_2O growth; thus, it may negligibly affect the electrical properties of graphene up to $F_{ox} = 15\%$ of Cu_2O growth. However, the continuous out-diffusion of Cu cations through the nucleation sites can expand and propagate the Cu cation diffusion path along with the G-GBs. When F_{ox} exceeds 15%, the propagation of the Cu cation diffusion path becomes severe and the Hall mobility of graphene is reduced. At F_{ox} values above 50%, most of the graphene grains seem to be electrically disconnected. As electrical measurement inevitably involves charge carrier transfer, the mechanically weak points of the damaged grain boundaries can be further damaged during the transfer process, thereby exaggerating the decreasing tendency of the Hall mobility (see **figure 2-10**). From these results, we tried to provide optimal conditions for G-GB visualization through the contour map of sheet resistance as a function of T_{ox} and t_{ox} as shown in **figure 2-9(d)**. The optimal condition requires a F_{ox} enough to measure the graphene grain size at the same time without changing the electrical properties of graphene. Therefore, as mentioned above, the maximum value of F_{ox} can be defined as 15%. On the other hand, G-GB is sufficiently revealed for measuring the graphene grain size when the amount of oxidation is at least about **figure 2-2(b)** and

(f), and the F_{ox} at this time is 10 %. The boundary for optimal F_{ox} values is shown as dashed lines in **figure 2-9(d)**. The difference in oxidation time indicated by the distance between dashed lines at 200°C is 50 min, so the process margin is very wide and oxidation time is relatively short compared to 180 °C. Therefore, oxidation at 200°C for 100 min, can be suggested as an optimal condition for G-GB visualization.

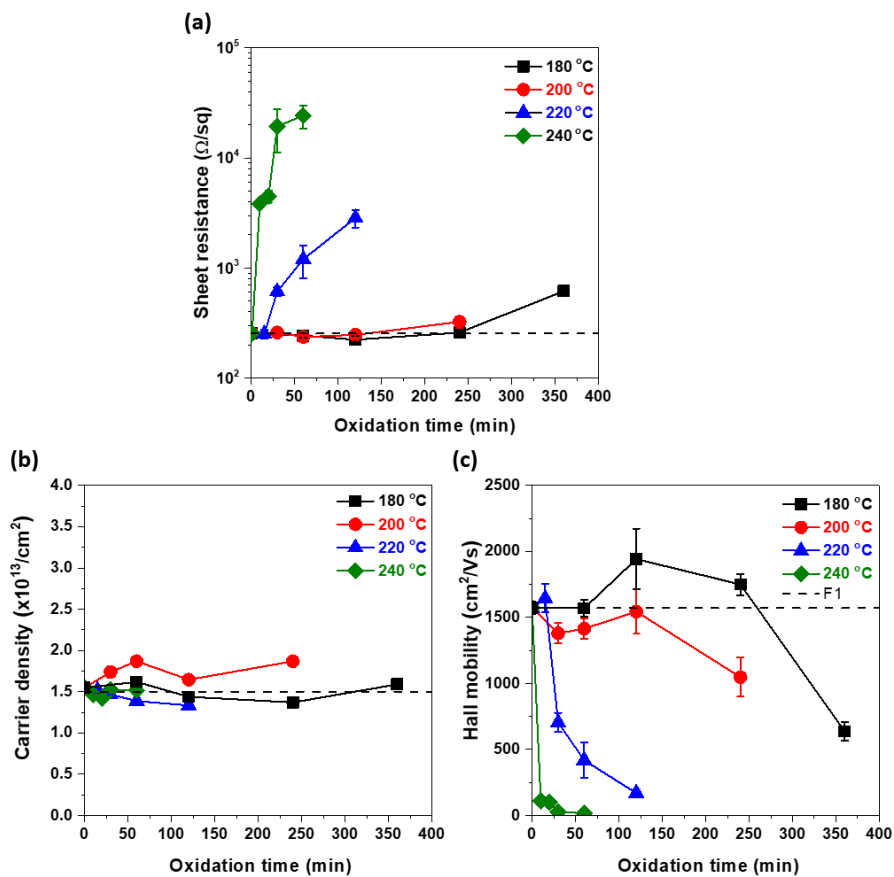


Figure. 2-8. Electrical properties of graphene as a function of the oxidation time at different oxidation temperatures (180 °C, 200 °C, 220 °C, and 240 °C); (a) sheet resistance (b) sheet carrier density, and (c) Hall mobility with dashed lines which represent the values of the as-grown graphene.

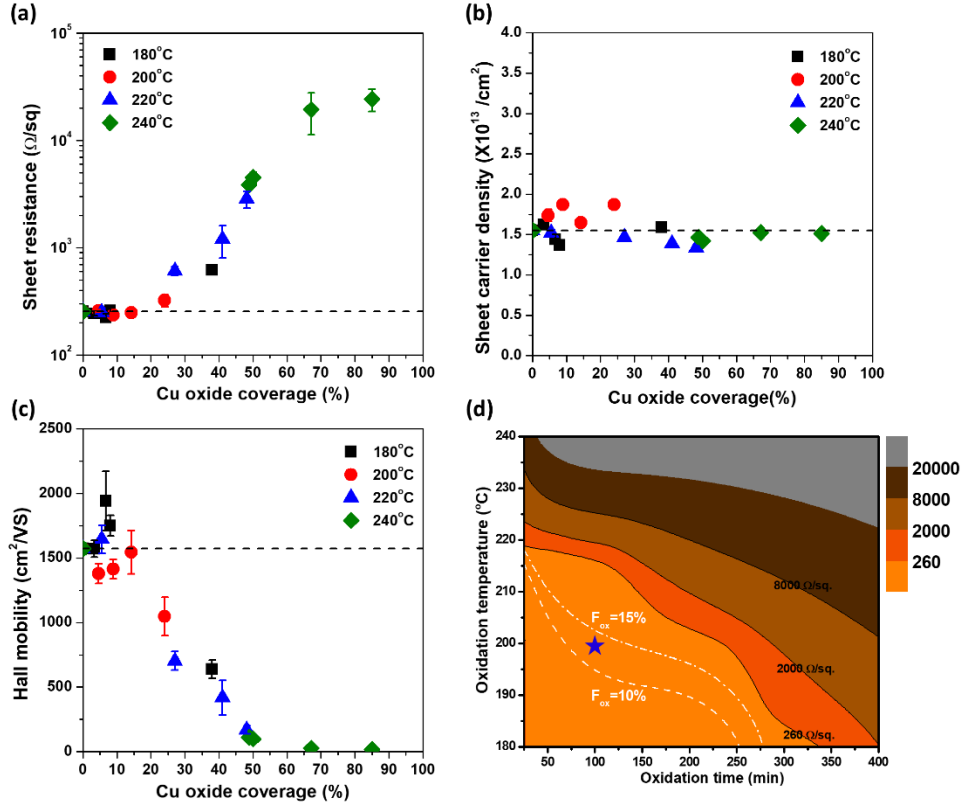


Figure. 2-9. Electrical properties of graphene as a function of Cu oxide coverage at different oxidation temperature (180°C, 200°C, 220°C, 240°C); (a) sheet resistance (b) sheet carrier density, and (c) Hall mobility. The black dashed lines represent the values of the as-grown graphene. (d) contour map of graphene sheet resistance with white dashed lines which indicates constant F_{ox} lines of 10% and 15%. The blue star represents the optimal condition of G-GB visualization.

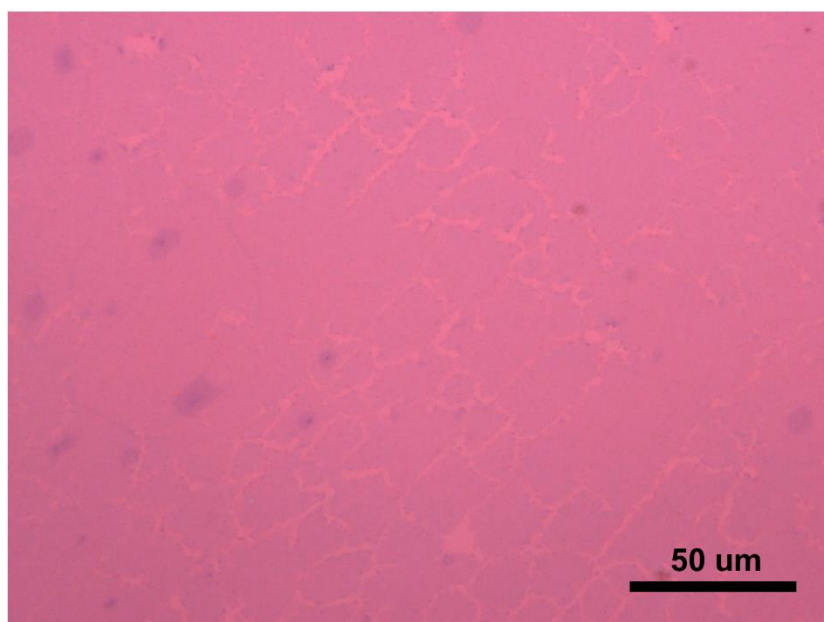


Figure. 2-10. Optical image of graphene transferred to SiO₂/Si substrate

2.4. Summary and conclusion

Cu oxidation through graphene was investigated in detail as a function of temperature and time. The kinetics of Cu oxidation through graphene were quantitatively determined based on the Cu oxide coverage that was determined from the OM image. There are three 3 unique features in discussing Cu₂O growth behavior on graphene. First, Cu₂O growth kinetics undergoes one-dimensional growth. The OM image and JMAK equation analysis shows the Cu₂O nucleation is limited in G-GBs and the Cu₂O one-dimensionally grows with suppressed further nucleation. Second, the Cu₂O growth is governed by dominant Cu cation out-diffusion in according to that; i) HR-TEM analysis reveals graphene layer is at the Cu-Cu₂O interface, ii) Cu oxidation predominantly occurs by dominant out-diffusion of Cu cation, iii) the graphene layer is not critically damaged by the volume expansion of Cu oxide. Third, F_{ox} of 10 ~ 15% confirmed that the graphene grain size could be measured without degradation of the electrical property of graphene, and suggested that the optimal condition considering practical points of experiments such as process margin is oxidation at 200°C for 100 min.

References

1. Novoselov, K. S.; Geim, A. K.; Morozov, S. V.; Jiang, D.; Zhang, Y.; Dubonos, S. V.; Grigorieva, I. V.; Firsov, A. A., Electric field effect in atomically thin carbon films. *Science* **2004**, *306* (5696), 666-669.
2. Li, X. S.; Cai, W. W.; An, J. H.; Kim, S.; Nah, J.; Yang, D. X.; Piner, R.; Velamakanni, A.; Jung, I.; Tutuc, E.; Banerjee, S. K.; Colombo, L.; Ruoff, R. S., Large-Area Synthesis of High-Quality and Uniform Graphene Films on Copper Foils. *Science* **2009**, *324* (5932), 1312-1314.
3. Lee, H. C.; Liu, W. W.; Chai, S. P.; Mohamed, A. R.; Aziz, A.; Khe, C. S.; Hidayah, N. M. S.; Hashim, U., Review of the synthesis, transfer, characterization and growth mechanisms of single and multilayer graphene (vol 7, pg 15644, 2017). *Rsc Adv* **2017**, *7* (45), 28427-28427.
4. Li, X. S.; Magnuson, C. W.; Venugopal, A.; Tromp, R. M.; Hannon, J. B.; Vogel, E. M.; Colombo, L.; Ruoff, R. S., Large-Area Graphene Single Crystals Grown by Low-Pressure Chemical Vapor Deposition of Methane on Copper. *J Am Chem Soc* **2011**, *133* (9), 2816-2819.
5. Yu, Q. K.; Jauregui, L. A.; Wu, W.; Colby, R.; Tian, J. F.; Su, Z. H.; Cao, H. L.; Liu, Z. H.; Pandey, D.; Wei, D. G.; Chung, T. F.; Peng, P.; Guisinger, N. P.; Stach, E. A.; Bao, J. M.; Pei, S. S.; Chen, Y. P., Control and characterization of individual grains and grain boundaries in graphene grown by chemical vapour deposition. *Nat Mater* **2011**, *10* (6), 443-449.
6. Zhou, H. L.; Yu, W. J.; Liu, L. X.; Cheng, R.; Chen, Y.; Huang, X. Q.; Liu, Y.; Wang, Y.; Huang, Y.; Duan, X. F., Chemical vapour deposition growth of large single crystals of monolayer and bilayer graphene. *Nat Commun*

2013, 4.

7. Cho, S. Y.; Kim, M. S.; Kim, M.; Kim, K. J.; Kim, H. M.; Lee, D. J.; Lee, S. H.; Kim, K. B., Self-assembly and continuous growth of hexagonal graphene flakes on liquid Cu. *Nanoscale* **2015**, 7 (30), 12820-12827.
8. Jauregui, L. A.; Cao, H. L.; Wu, W.; Yu, Q. K.; Chen, Y. P., Electronic properties of grains and grain boundaries in graphene grown by chemical vapor deposition. *Solid State Commun* **2011**, 151 (16), 1100-1104.
9. Lopez-Polin, G.; Gomez-Navarro, C.; Parente, V.; Guinea, F.; Katsnelson, M. I.; Perez-Murano, F.; Gomez-Herrero, J., Increasing the elastic modulus of graphene by controlled defect creation. *Nat Phys* **2015**, 11 (1), 26-31.
10. Hao, F.; Fang, D. N.; Xu, Z. P., Mechanical and thermal transport properties of graphene with defects. *Appl Phys Lett* **2011**, 99 (4).
11. Yan, Z.; Lin, J.; Peng, Z. W.; Sun, Z. Z.; Zhu, Y.; Li, L.; Xiang, C. S.; Samuel, E. L.; Kittrell, C.; Tour, J. M., Toward the Synthesis of Wafer-Scale Single-Crystal Graphene on Copper Foils. *Acs Nano* **2012**, 6 (10), 9110-9117.
12. Chen, S. S.; Ji, H. X.; Chou, H.; Li, Q. Y.; Li, H. Y.; Suk, J. W.; Piner, R.; Liao, L.; Cai, W. W.; Ruoff, R. S., Millimeter-Size Single-Crystal Graphene by Suppressing Evaporative Loss of Cu During Low Pressure Chemical Vapor Deposition. *Adv Mater* **2013**, 25 (14), 2062-2065.
13. Hao, Y. F.; Bharathi, M. S.; Wang, L.; Liu, Y. Y.; Chen, H.; Nie, S.; Wang, X. H.; Chou, H.; Tan, C.; Fallahazad, B.; Ramanarayan, H.; Magnuson, C. W.; Tutuc, E.; Yakobson, B. I.; McCarty, K. F.; Zhang, Y. W.; Kim, P.; Hone, J.; Colombo, L.; Ruoff, R. S., The Role of Surface

- Oxygen in the Growth of Large Single-Crystal Graphene on Copper. *Science* **2013**, 342 (6159), 720-723.
14. Malard, L. M.; Pimenta, M. A.; Dresselhaus, G.; Dresselhaus, M. S., Raman spectroscopy in graphene. *Phys Rep* **2009**, 473 (5-6), 51-87.
 15. Ferrari, A. C.; Basko, D. M., Raman spectroscopy as a versatile tool for studying the properties of graphene. *Nat Nanotechnol* **2013**, 8 (4), 235-246.
 16. Tuinstra, F.; Koenig, J. L., Raman Spectrum of Graphite. *J Chem Phys* **1970**, 53 (3), 1126-&.
 17. Das, A.; Pisana, S.; Chakraborty, B.; Piscanec, S.; Saha, S. K.; Waghmare, U. V.; Novoselov, K. S.; Krishnamurthy, H. R.; Geim, A. K.; Ferrari, A. C.; Sood, A. K., Monitoring dopants by Raman scattering in an electrochemically top-gated graphene transistor. *Nat Nanotechnol* **2008**, 3 (4), 210-215.
 18. Kim, K.; Lee, Z.; Regan, W.; Kisielowski, C.; Crommie, M. F.; Zettl, A., Grain Boundary Mapping in Polycrystalline Graphene. *Acs Nano* **2011**, 5 (3), 2142-2146.
 19. Suk, J. W.; Kitt, A.; Magnuson, C. W.; Hao, Y. F.; Ahmed, S.; An, J. H.; Swan, A. K.; Goldberg, B. B.; Ruoff, R. S., Transfer of CVD-Grown Monolayer Graphene onto Arbitrary Substrates. *Acs Nano* **2011**, 5 (9), 6916-6924.
 20. Jia, C. C.; Jiang, J. L.; Gan, L.; Guo, X. F., Direct Optical Characterization of Graphene Growth and Domains on Growth Substrates. *Sci Rep-Uk* **2012**, 2.
 21. Lee, J. Y.; Lee, J. H.; Kim, M. J.; Dash, J. K.; Lee, C. H.; Joshi, R.; Lee, S.; Hone, J.; Soon, A.; Lee, G. H., Direct observation of grain boundaries in chemical vapor deposited graphene. *Carbon* **2017**, 115, 147-153.

22. Hong, K. P.; Lee, D.; Choi, J. B.; Kim, Y.; Kim, H., Real-Time Optical Visualization of Graphene Defects and Grain Boundaries by the Thermal Oxidation of a Graphene-Coated Copper Foil. *Acs Appl Nano Mater* **2018**, *1* (6), 2515-2520.
23. Duong, D. L.; Han, G. H.; Lee, S. M.; Gunes, F.; Kim, E. S.; Kim, S. T.; Kim, H.; Ta, Q. H.; So, K. P.; Yoon, S. J.; Chae, S. J.; Jo, Y. W.; Park, M. H.; Chae, S. H.; Lim, S. C.; Choi, J. Y.; Lee, Y. H., Probing graphene grain boundaries with optical microscopy. *Nature* **2012**, *490* (7419), 235-+.
24. Kwak, J.; Jo, Y.; Park, S. D.; Kim, N. Y.; Kim, S. Y.; Shin, H. J.; Lee, Z.; Kim, S. Y.; Kwon, S. Y., Oxidation behavior of graphene-coated copper at intrinsic graphene defects of different origins. *Nat Commun* **2017**, *8*.
25. Kunka, C.; Bavdekar, S.; Rudawski, N. G.; Fournier, A.; Subhash, G., Oxidation of the polycrystalline copper-graphene nanocomposite. *Journal of Physics: Materials* **2019**, *2* (2).
26. Yoon, T.; Mun, J. H.; Cho, B. J.; Kim, T. S., Penetration and lateral diffusion characteristics of polycrystalline graphene barriers. *Nanoscale* **2014**, *6* (1), 151-156.
27. Chen, S. S.; Brown, L.; Levendorf, M.; Cai, W. W.; Ju, S. Y.; Edgeworth, J.; Li, X. S.; Magnuson, C. W.; Velamakanni, A.; Piner, R. D.; Kang, J. Y.; Park, J.; Ruoff, R. S., Oxidation Resistance of Graphene-Coated Cu and Cu/Ni Alloy. *Acs Nano* **2011**, *5* (2), 1321-1327.
28. Wofford, J. M.; Nie, S.; McCarty, K. F.; Bartelt, N. C.; Dubon, O. D., Graphene Islands on Cu Foils: The Interplay between Shape, Orientation, and Defects. *Nano Lett* **2010**, *10* (12), 4890-4896.

29. Jo, K.; Kim, S. M.; Lee, S. M.; Kim, J. H.; Lee, H. J.; Kim, K. S.; Kwon, Y. D.; Kim, K. S., One-step etching, doping, and adhesion-control process for graphene electrodes. *Carbon* **2015**, 82, 168-175.
30. Lee, S. K.; Hsu, H. C.; Tuan, W. H., Oxidation Behavior of Copper at a Temperature below 300 degrees C and the Methodology for Passivation. *Mater Res-Ibero-Am J* **2016**, 19 (1), 51-56.
31. Bridges, D. W.; Baur, J. P.; Baur, G. S.; Fassell, W. M., Oxidation of Copper to Cu₂O and CuO (600-Degrees-C-1000-Degrees-C and 0.026-20.4 Atm Oxygen). *J Electrochem Soc* **1956**, 103 (9), 475-478.
32. Mrowec, S.; Stoklosa, A., Oxidation of Copper at High Temperatures. *Oxid Met* **1971**, 3 (3), 291-&.
33. Biro, L. P.; Lambin, P., Grain boundaries in graphene grown by chemical vapor deposition. *New J Phys* **2013**, 15.
34. Jang, H.; Dai, Z. H.; Ha, K. H.; Ameri, S. K.; Lu, N. S., Stretchability of PMMA-supported CVD graphene and of its electrical contacts. *2d Mater* **2020**, 7 (1).
35. Bae, S. H.; Lee, Y.; Sharma, B. K.; Lee, H. J.; Kim, J. H.; Ahn, J. H., Graphene-based transparent strain sensor. *Carbon* **2013**, 51, 236-242.
36. Avrami, M., Kinetics of phase change I - General theory. *J Chem Phys* **1939**, 7 (12), 1103-1112.
37. Hermoni, A.; Salmon, A., Application of Avrami Theory on Transformation - Time Relations for Random Distribution of Nuclei to Catalytic Decomposition of Ammonium Perchlorate. *B Res Counc Israel* **1962**, A 11 (3), 200-&.
38. Ebisuzaki, Y.; Sanborn, W. B., Oxidation-Kinetics of Copper - an Experiment in Solid-State Chemistry. *J Chem Educ* **1985**, 62 (4), 341-343.

CHAPTER 3.

Liquid Cu phase effect on graphene growth

This chapter is based on the paper published in

Journal of Nanoscience and Nanotechnology

20, 316-323, (2020).

2.1. Introduction

Graphene is a single-atomic-layer of sp^2 -bonded crystalline carbon atoms, which has received much attention due to its fascinating electrical,¹⁻⁴ optical⁵, and mechanical properties.⁶ Various graphene synthesis methods have been developed so far,⁷⁻¹⁰ and among them, chemical vapor deposition (CVD) is most widely used owing to its feasibility of mass production and compatibility with conventional semiconductor thin film processing. Metal is typically used as a template for graphene growth due to catalytic activity for dissociating hydrocarbon sources and crystallizing carbon atoms. Cu is the most popular catalyst since it has extremely low carbon solubility and easily provides single-layer graphene.¹¹ However, graphene grown on Cu shows polycrystalline nature resulted from random nucleation.^{12,13} Graphene grain boundaries disrupt structural continuity and electron transport behavior, resulting in low charge carrier mobility and poor mechanical properties compared to a single crystal.¹³⁻¹⁵

Therefore, many researches on graphene growth have been conducted to overcome the polycrystalline nature. For instance, to increase the grain size and reduce the grain boundary density, many works have been studied.¹⁶⁻¹⁸ Controlling process parameters are a simple approach to enlarge the grain size of graphene (e.g., growth temperature, partial pressure, and flux of source gas), but these methods are inefficient. For example, suppressing nucleation density by lower hydrocarbon flux requires a much longer growth time to obtain full coverage graphene due to an insufficient supply of carbon monomers.^{19,20} Higher growth temperature provides longer surface diffusion length of carbon monomers and larger grain sizing

accordingly,^{21,22} but It also has an experimental limitation in increasing the growth temperature. Other useful approaches reducing heterogeneous nucleation sites on Cu by suppressing Cu surface imperfections.^{23,24} Cu template for graphene growth are not an ideal smooth surface, rather, it contains the mechanical rolling feature, scratches, and many impurities which potentially result in heteronucleation sites for graphene growth. High pressure and temperature annealing prior to graphene growth achieved larger single-crystal graphene by smoothing Cu surface.^{25,26} Electropolishing and chemical mechanical planarization (CMP) also showed a smoother surface compared to the as-purchased Cu foil and reduced graphene nuclei density.^{20,23} Several groups reported that oxygen on the Cu surface may decreases nucleation density by passivating active Cu sites for nucleation.^{27,28} In addition, to remove the surface impurities, it was reported that little etching of Cu surface by CH₃COOH, HCl, and FeCl₃ is beneficial.^{27,29}

One of the methods to eliminate the structural defect of Cu is to liquefy the Cu catalyst for graphene growth. Previous researches demonstrated that graphene growth on liquid Cu shows unique growth behaviors of self-assembly and self-alignment.^{30,31} Graphene grains grown on liquid Cu shows the same orientation for each other with no significant structural disorder. And aligned grains show negligible degradation of the electrical transport properties across the commensurate grain boundary.³² Although liquid Cu is an ideal flat surface, there are a few reports which mentioned liquid Cu phase effect on the graphene grain size. We *et al.* reported growth of single-crystalline graphene grains with size up to 200 μm on liquid Cu by optimizing CVD conditions.³³ However, graphene grain size and nuclei density not only depend on catalyst surface property but temperature effect.^{19,34} Thus, it is

necessary to prove the liquid Cu effect and exclude high-temperature effects on graphene grain size.

In this work, we studied the liquid Cu phase effect on graphene growth by comparing it with graphene grown on solid Cu in the same growth conditions except for temperature. Growth temperature for graphene varied from 1020 °C to 1100 °C with 40 °C interval. Through the graphene growth as a function of growth time, we compared the growth behavior of graphene on solid and liquid Cu by using scanning electron microscopy (SEM) and optical microscopy (OM) after selective oxidation of Cu. Nuclei density and average grain size were also measured. Atomic structure of graphene studied by transmission electron microscopy (TEM). Full coverage graphene grown on solid and liquid Cu were also studied. Defect density compared by Raman spectrum analysis. It also confirmed with electrical property in sheet resistance and carrier mobility.

3.2. Experimental details

3.2.1. Synthesis of graphene

Schematic illustration of the main experiment is provided in **figure 3-1**. First, a couple of electropolished Cu foils (Alfa Aesar #13382) are put on top of 50- μm -thick W foil (Alfa Aesar #10417) and loaded into a quartz tube type furnace (Lindberg, blue). The furnace was pumped down to $\sim 10^{-3}$ Torr. Then, the chamber was made to atmospheric pressure by flowing Ar 300 standard cubic centimeters per minute (sccm) and H_2 10 sccm, and heating started at a rate of $35\text{ }^\circ\text{C}/\text{min}$. After reaching target temperature of solid Cu ($1020\text{ }^\circ\text{C}$, $1060\text{ }^\circ\text{C}$) and liquid Cu ($1100\text{ }^\circ\text{C}$), 50 sccm of CH_4 (1000ppm diluted in Ar) precursor was introduced to grow graphene. The growth time was varied from 5 to 40 minutes for partial and full coverage graphene on solid Cu. On the other hand, it takes a longer time to grow graphene on liquid Cu. Thus, the growth time of 10 to 80 minutes was applied for partial coverage. However, full coverage graphene growth on liquid Cu should be a special consideration. Due to the thermal stress induced by the solidification of Cu, cracks are frequently observed after cooling.³⁵ In order to eliminate the cracks, we applied two-step growth.³² Once the growth of 90 minutes was completed with the conditions outlined above, the temperature was decreased from $1100\text{ }^\circ\text{C}$ to $1060\text{ }^\circ\text{C}$ under a cooling rate of $40\text{ }^\circ\text{C}/\text{min}$ for Cu solidification. And diluted CH_4 flux was further increased to 100 sccm for 30 minutes to provide fully covered graphene. After graphene growth, cooling was started under a cooling rate of $160\text{ }^\circ\text{C}/\text{min}$ in both cases.

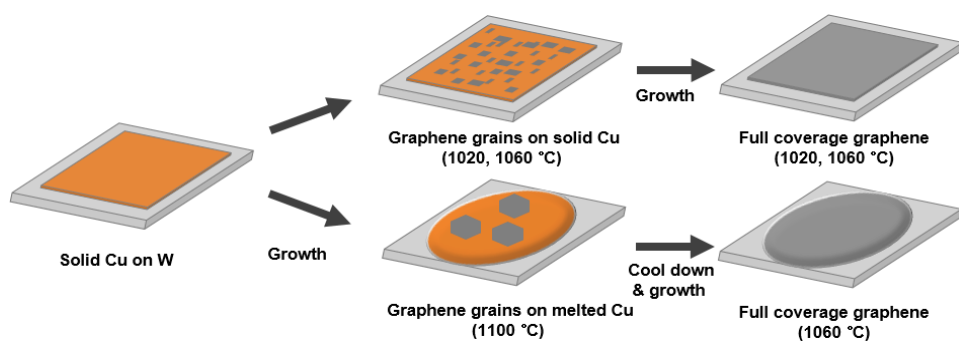


Figure. 3-1. Schematic illustration of partial and full coverage graphene growth on solid/liquid Cu at 1020, 1060 and 1100 °C.

3.2.2. Transfer and characterization

The graphene was transferred by a well-known process, which uses polymethyl methacrylate (PMMA) coating and subsequent etching of underlying Cu or Cu/W layers. In particular, W etching was performed by anodic etching which uses bare Cu foil as a cathode in 2 M NaOH solution.³⁵ The PMMA/graphene/Cu stack was then floated on ammonium persulfate solution (0.1 M) for 8 hours after complete etching of the Cu. The floated PMMA/graphene layer was scooped on a SiO₂(285 nm)/Si substrate for electrical and Raman measurement or TEM grid (20 nm-thick Si₃N₄ membranes or Quantifoil). Partial and full coverage graphene images on Cu were acquired with SEM (Merlin compact, Karl Zeiss) and OM (Olympus BX50) after selective oxidation of Cu. Selective oxidation of Cu was carried out by heating the samples in an air atmosphere on a hot plate at a temperature of 200 °C for 1 min. And nuclei density, grain sizes, and coverages were measured by using image analysis software (Image-Pro, 4.5). Graphene on TEM grid analyzed using analytical TEM (JEM-2100F, JEOL) Raman spectra were carried out by using UniRam system with DPSS (diode-pumped solid state) laser (100 mW, 532 nm). Sheet resistance and Hall mobility were measured by using the Van der Pauw (VDP) structure size of 9 X 9 mm. Hall measurements were performed under a 0.5 T magnetic field (HL 5500PC, BIO-RAD) at room temperature.

3.3. Results and discussion

3.3.1. Growth behavior of graphene

In order to compare the liquid Cu phase effect with the growth temperature effect, we chose growth temperatures from 1020 °C, 1060 °C, and 1100 °C as shown in Figure 1. Remind that the melting temperature of Cu is 1083 °C. After 10 min growth at 1020 °C, partial coverage graphene formed on solid Cu as is shown in **figure 3-2(a)**. It shows irregular shapes with high nuclei density with small grain size ($< 1 \mu\text{m}$). As the growth time increases (**Figure 3-2(b)** and **(c)**), additional nuclei formed and individual grains were eventually merged into almost full coverage after 30 min growth (~97% coverage). At 1060 °C of growth temperature, as shown in **figure 3-2(d-f)**, graphene with 10 min growth shows the coverage of 86% where grains already started to merge. The graphene with 20 min growth shows small gaps between the graphene grains (**Figure 3-2(e)**) and full coverage graphene already formed within 30 min growth (**Figure 3-2(f)**). Almost full coverage graphene with a different growth time of **figure 3-2(c)** and **(d)** show that there is no significant difference in grain size and nuclei density even though the temperature difference is 40 °C. Increasing the growth temperature provides a larger surface diffusion length of active carbons, which is known to increase grain size and arrival rate of carbon adatoms to nuclei at the same time.^{21,22} However, our graphene growth condition on solid Cu is already overfeeding carbon flux, enlarging grain size at higher temperature was not observed. Instead, the increase in surface diffusion length of carbon monomers only affects the coverage rate. When the growth temperature is further increased to 1100 °C for liquid Cu formation, a compact hexagon shape with

large grains appears as shown in **figure 3-2(g), (h), and (i)**. As the growth time increased, graphene coverage increase from 3 % to 64 % for 10 min and 30 min growth, respectively. The typical grain size of graphene is greater than 30 μm with a high symmetrical shape (**Figure 3-2(h)**). It is evident that even with the same gas condition, liquid metal catalyst not only suppresses high nuclei density presumably due to no surface defects but provide nicer growth morphologies of the symmetric hexagon shape. Graphene islands on liquid Cu aligned in the same Cu lattice.³³ Alignments of graphene islands on liquid Cu are easier to observe due to a compact hexagon. It is well illustrated on the dotted auxiliary lines in **figure 3-2(g)-(i)**.

Figure 3-3(a) shows measured average coverage of graphene on Cu as a function of growth time at different temperatures. Due to the increase of surface diffusion length, graphene grows faster at a higher temperature on solid Cu.³⁴ Full coverage graphene formed after 30 min and 40 min growth at 1060 °C and 1020 °C, respectively. However, if graphene grows on liquid Cu, the growth rate is drastically suppressed. Even after 60 min of growth, graphene coverage is still around 80 %. The reduction of coverage rate can be explained by suppression of heteronuclei due to smooth liquid Cu surface. Also, desorption of the carbon monomers would be more favorable since there are no active sites to be attached. This fact can explain lower graphene coverage on liquid Cu. In fact, several studies reported that heteronuclei can be suppressed and the growth rate can be decreased by reducing the roughness of Cu through high-pressure annealing or surface polishing.^{20,25} In order to compare the nuclei density and grain sizes of graphene, image analysis was carried out on 40 ~ 50 % coverage graphene on Cu. As shown in **figure 3-3(b)**, 10 min (1020 °C) and 5 min (1060 °C) growth on solid Cu graphene average grain density have

3.02 / μm^2 and 3.60/ μm^2 , respectively. However, the average graphene grain density of graphene grown on liquid Cu in the same conditions shows four orders lower nuclei density of 0.0004/ μm^2 . Inversely, lateral grain sizes are two orders larger on liquid Cu compared to graphene grown on solid Cu as shown in **figure 3-3(c)**. The average grain size of graphene grown on solid Cu was 0.4 μm in both cases, but the grain size of graphene grown on liquid Cu was increased to 38.5 μm .

TEM analysis was used to obtain structural information of graphene. **Figure 3-4(a)** show a bright-field TEM image of full coverage graphene grown on solid Cu at 1020 °C. **Figure 3-4(b)** shows an electron diffraction pattern of the dashed area of figure 4a. This diffraction pattern shows that three sets of rotated six-membered rings which indicate three different graphene grains existed in the selected area. **Figure 3-4(c)** shows a dark-field image of the same area from the diffraction spot 1. The bright area clearly shows the graphene morphology. In the case of graphene grown on solid Cu at 1060°C shown in **figure 3-4(d) to (f)**. It indicates that two different graphene grains constitute the area. Both graphene dark field images show lateral grain sizes are smaller than 2 μm . There is no significant difference obtained from the SEM image. On the other hand, the bright-field image of graphene grown liquid Cu shown in figure 4g. Hexagonal graphene partially covered on the TEM grid. The diffraction patterns were obtained in 4 areas separated by 2 μm or more. The orientation of each diffraction pattern in figure 4h to k indicates all the same direction which means that hexagonal graphene is a single crystal.

In order to compare the quantitative defect density of graphene which is typically grain boundaries, Raman spectra were taken. We prepared full coverage graphene film on solid and liquid Cu, and Raman spectra were achieved after transfer to 285-

nm SiO₂/Si substrate. Growth times of 40 min and 30 min were enough to achieve a continuous graphene layer on solid Cu at 1020 °C and 1060 °C, respectively. Contrary to observable D band intensity in **figure 3-5(a)**, D band intensity was negligible in graphene due to the liquid phase effect on grain size in **figure 3-5(b)**. The larger D band peak intensity of **figure 3-5(a)** is not the effect of graphene edges since all of the graphene samples were a continuous film. Statistical analysis of the Raman spectrum is also meaningful to check the defect density of graphene. **Figure 3-5(c)** shows the I_D/I_G ratio in the Raman spectrum achieved through randomly chosen 100 points. Compared to graphene on both solid Cu having I_D/I_G ratio of 0.3 ~ 0.8, roughly, graphene grown on liquid Cu shows significantly lower I_D/I_G ratio, all the point values are lower than 0.3. It also indicates that graphene grown on liquid Cu has a lower defect density compared to graphene grown on solid Cu. However, which shown in **figure 3-5(d)**, I_{2D}/I_G ratio did not show a significant difference which indicates that the number of graphene layers is not changed due to the liquid Cu phase effect.

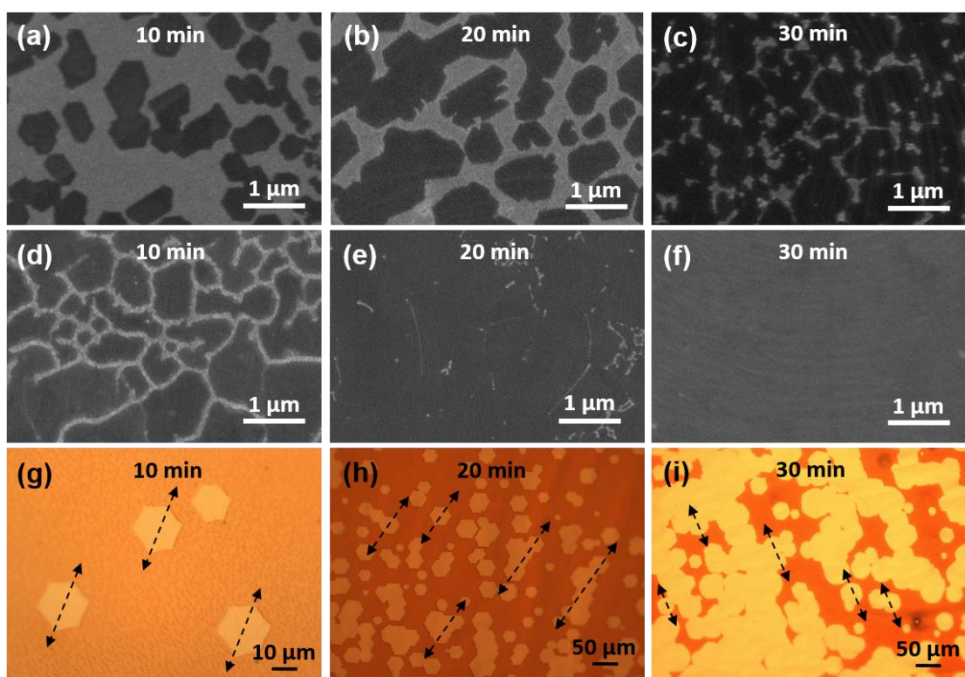


Figure. 3-2. SEM and optical images of graphene grown on solid and liquid Cu with various growth time. SEM image of (a) 10 min, (b) 20 min and (c) 30 min growth on solid Cu at 1020 °C. (d) 10 minutes, (e) 20 min and (f) 30 min growth on solid Cu at 1060 °C. Optical microscopy image of (g) 10 min, (h) 20 min and (i) 30 min growth on liquid Cu at 1100 °C after selective oxidation of Cu. Parallel arrows indicate graphene grains are aligned in the same directions.

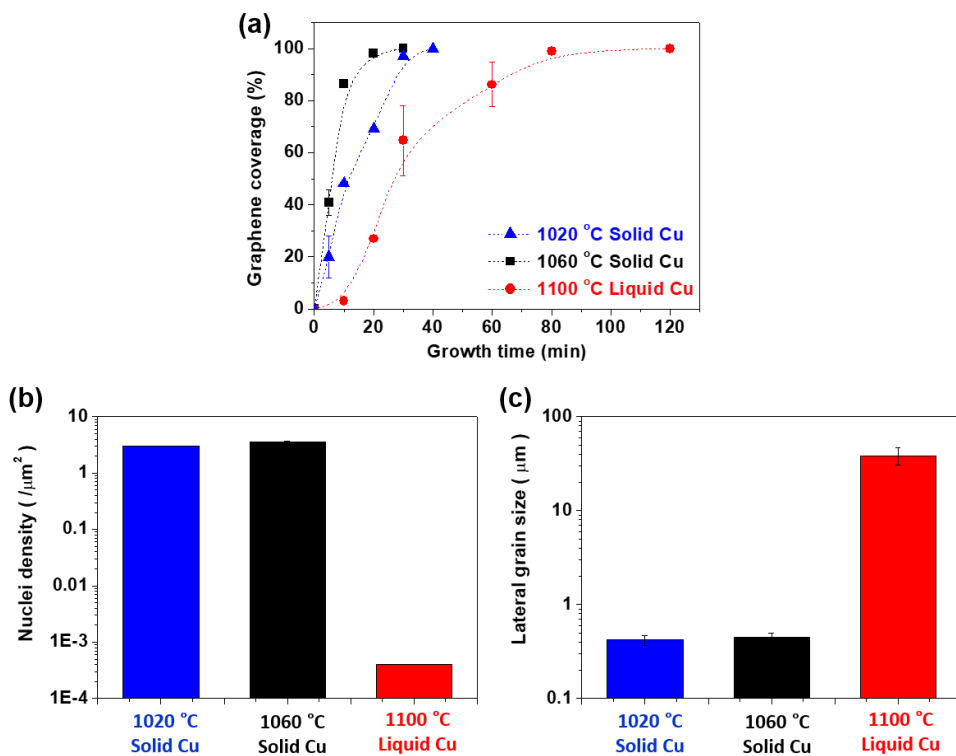


Figure. 3-3. (a) Graphene coverage on Cu as a function of growth time obtained at different temperatures. (b) nuclei density and (c) grain size difference of graphene grown on solid and liquid Cu, respectively.

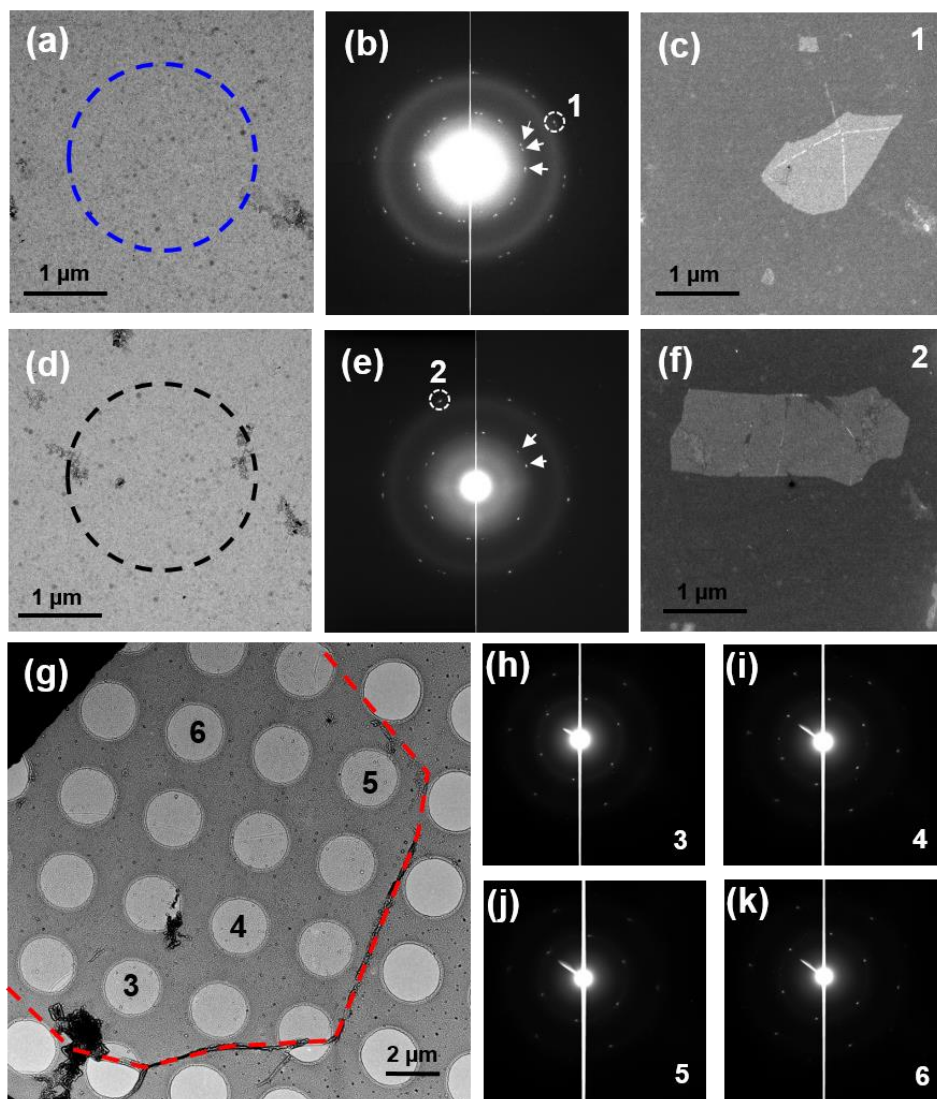


Figure. 3-4. TEM images of graphene grown on solid and liquid Cu. (a) Bright-field image of full coverage graphene grown on solid Cu (1020 °C) and (b) diffraction pattern of the dashed area of (a). (c) dark-field image of the same area from the diffraction spot 1. (d) Bright-field image of full coverage graphene grown on solid Cu (1060 °C) and (e) diffraction pattern of the dashed area of (d). (f) dark-field image of the same area from the diffraction spot 2. (g) Bright-field image of partial coverage hexagonal shaped graphene grown on liquid Cu. The edges of the domains are delineated by dashed lines. (h-k) diffraction patterns taken in corresponding windows of grid.

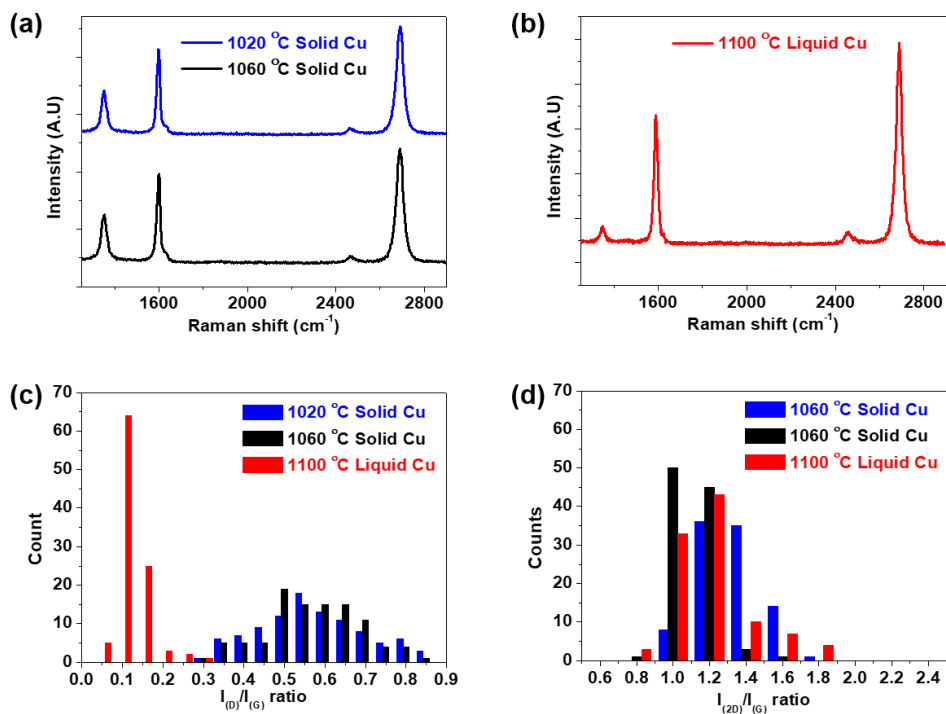


Figure. 3-5. Raman spectra of full coverage graphene films grown on (a) solid Cu (1020 °C, 1060 °C) and (b) liquid Cu (1100 °C). (c-d) statistical analysis of Raman spectra on I_D/I_G and I_{2D}/I_G taken from randomly selected 100 points on full coverage graphene, respectively.

3.3.2. Comparison of electrical properties of graphene grown on solid and liquid copper by chemical vapor deposition

Electrical properties of full coverage graphene were also characterized by Hall measurement. **Figure 3-6(a)** shows that the average sheet resistance of graphene on solid Cu is 1661 Ω/sq (1020 $^{\circ}\text{C}$) and 1764 Ω/sq (1060 $^{\circ}\text{C}$) and the sheet resistance drastically decreased to 484 Ω/sq after growth on liquid Cu phase. liquid Cu phase provided much lower electrical resistance. Hall mobility was also extracted from Hall measurement, as presented in **figure 3-6(b)**. The Hall mobility of graphene grown on solid Cu, were 149 cm^2/Vs and 188 cm^2/Vs at 1020 $^{\circ}\text{C}$ and 1060 $^{\circ}\text{C}$, respectively. Notice that higher growth temperature did not change much on the mobility of graphene on solid Cu, liquid Cu phase provided much higher mobility of 759 cm^2/Vs by enlarging the grain size. It clearly shows sheet resistance reduction comes from the increasing mobility presumably from larger grain size and less scattering during the electrical transport. This was possible by lower defect density in graphene grown on liquid Cu.

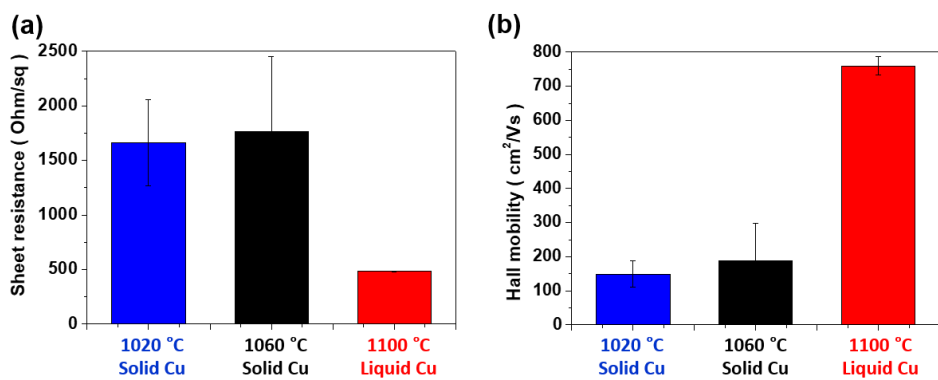


Figure 3-6. Electrical property of full coverage graphene grown on solid and liquid Cu. (a) sheet resistance of graphene grown with different temperature and extracted (b) Hall mobility.

3.4. Summary and conclusion

Liquid Cu phase effect on graphene growth has been studied by direct comparison of graphene on solid and liquid Cu. Even though the coverage rate of graphene increased at high temperature on solid Cu, growth rate of graphene was extremely retarded on liquid Cu. It clearly shows that surface smoothening drastically suppressed the heterogeneous nucleation of graphene seeds. Nuclei density of graphene reduced from 3 to 0.0004 / μm^2 by liquid catalyst effect. But the lateral grain size also increased by almost 2 orders from 0.4 to 38.3 μm . The irregular shape of graphene grains changed into symmetric hexagonal on liquid Cu which well aligned with the same orientation. The decrease in the intensity ratio of I_D/I_G from 0.3 ~ 0.8 to 0.1 provided clear evidence of defect density decrease as a result of reducing graphene grain boundary. Finally, it has also been confirmed in sheet resistance which reduced from 1764 to 484 ohm/sq. Simple melting of Cu catalyst provides an improvement of the graphene quality without further tuning in growth parameters.

References

1. Geim, A. K.; Novoselov, K. S., The rise of graphene. *Nat Mater* **2007**, 6 (3), 183-191.
2. Novoselov, K. S.; Jiang, D.; Schedin, F.; Booth, T. J.; Khotkevich, V. V.; Morozov, S. V.; Geim, A. K., Two-dimensional atomic crystals. *P Natl Acad Sci USA* **2005**, 102 (30), 10451-10453.
3. Novoselov, K. S.; Geim, A. K.; Morozov, S. V.; Jiang, D.; Zhang, Y.; Dubonos, S. V.; Grigorieva, I. V.; Firsov, A. A., Electric field effect in atomically thin carbon films. *Science* **2004**, 306 (5696), 666-669.
4. Bolotin, K. I.; Sikes, K. J.; Jiang, Z.; Klima, M.; Fudenberg, G.; Hone, J.; Kim, P.; Stormer, H. L., Ultrahigh electron mobility in suspended graphene. *Solid State Commun* **2008**, 146 (9-10), 351-355.
5. Nair, R. R.; Blake, P.; Grigorenko, A. N.; Novoselov, K. S.; Booth, T. J.; Stauber, T.; Peres, N. M. R.; Geim, A. K., Fine structure constant defines visual transparency of graphene. *Science* **2008**, 320 (5881), 1308-1308.
6. Lee, C.; Wei, X. D.; Kysar, J. W.; Hone, J., Measurement of the elastic properties and intrinsic strength of monolayer graphene. *Science* **2008**, 321 (5887), 385-388.
7. Kim, K. S.; Zhao, Y.; Jang, H.; Lee, S. Y.; Kim, J. M.; Kim, K. S.; Ahn, J. H.; Kim, P.; Choi, J. Y.; Hong, B. H., Large-scale pattern growth of graphene films for stretchable transparent electrodes. *Nature* **2009**, 457 (7230), 706-710.
8. Dikin, D. A.; Stankovich, S.; Zimney, E. J.; Piner, R. D.; Dommett, G. H. B.; Evmenenko, G.; Nguyen, S. T.; Ruoff, R. S., Preparation and

- characterization of graphene oxide paper. *Nature* **2007**, *448* (7152), 457-460.
9. Eda, G.; Fanchini, G.; Chhowalla, M., Large-area ultrathin films of reduced graphene oxide as a transparent and flexible electronic material. *Nat Nanotechnol* **2008**, *3* (5), 270-274.
 10. Sutter, P. W.; Flege, J. I.; Sutter, E. A., Epitaxial graphene on ruthenium. *Nat Mater* **2008**, *7* (5), 406-411.
 11. Li, X. S.; Cai, W. W.; An, J. H.; Kim, S.; Nah, J.; Yang, D. X.; Piner, R.; Velamakanni, A.; Jung, I.; Tutuc, E.; Banerjee, S. K.; Colombo, L.; Ruoff, R. S., Large-Area Synthesis of High-Quality and Uniform Graphene Films on Copper Foils. *Science* **2009**, *324* (5932), 1312-1314.
 12. Mattevi, C.; Kim, H.; Chhowalla, M., A review of chemical vapour deposition of graphene on copper. *J Mater Chem* **2011**, *21* (10), 3324-3334.
 13. Huang, P. Y.; Ruiz-Vargas, C. S.; van der Zande, A. M.; Whitney, W. S.; Levendorf, M. P.; Kevek, J. W.; Garg, S.; Alden, J. S.; Hustedt, C. J.; Zhu, Y.; Park, J.; McEuen, P. L.; Muller, D. A., Grains and grain boundaries in single-layer graphene atomic patchwork quilts. *Nature* **2011**, *469* (7330), 389-+.
 14. Yu, Q. K.; Jauregui, L. A.; Wu, W.; Colby, R.; Tian, J. F.; Su, Z. H.; Cao, H. L.; Liu, Z. H.; Pandey, D.; Wei, D. G.; Chung, T. F.; Peng, P.; Guisinger, N. P.; Stach, E. A.; Bao, J. M.; Pei, S. S.; Chen, Y. P., Control and characterization of individual grains and grain boundaries in graphene grown by chemical vapour deposition. *Nat Mater* **2011**, *10* (6), 443-449.
 15. Tsen, A. W.; Brown, L.; Levendorf, M. P.; Ghahari, F.; Huang, P. Y.; Havener, R. W.; Ruiz-Vargas, C. S.; Muller, D. A.; Kim, P.; Park, J., Tailoring Electrical Transport Across Grain Boundaries in Polycrystalline

- Graphene. *Science* **2012**, 336 (6085), 1143-1146.
16. Wu, T. R.; Ding, G. Q.; Shen, H. L.; Wang, H. M.; Sun, L.; Jiang, D.; Xie, X. M.; Jiang, M. H., Triggering the Continuous Growth of Graphene Toward Millimeter-Sized Grains. *Adv Funct Mater* **2013**, 23 (2), 198-203.
 17. Vlassiounk, I.; Smirnov, S.; Regmi, M.; Surwade, S. P.; Srivastava, N.; Feenstra, R.; Eres, G.; Parish, C.; Lavrik, N.; Datskos, P.; Dai, S.; Fulvio, P., Graphene Nucleation Density on Copper: Fundamental Role of Background Pressure. *J Phys Chem C* **2013**, 117 (37), 18919-18926.
 18. Chen, S. S.; Ji, H. X.; Chou, H.; Li, Q. Y.; Li, H. Y.; Suk, J. W.; Piner, R.; Liao, L.; Cai, W. W.; Ruoff, R. S., Millimeter-Size Single-Crystal Graphene by Suppressing Evaporative Loss of Cu During Low Pressure Chemical Vapor Deposition. *Adv Mater* **2013**, 25 (14), 2062-2065.
 19. Li, X. S.; Magnuson, C. W.; Venugopal, A.; An, J. H.; Suk, J. W.; Han, B. Y.; Borysiak, M.; Cai, W. W.; Velamakanni, A.; Zhu, Y. W.; Fu, L. F.; Vogel, E. M.; Voelkl, E.; Colombo, L.; Ruoff, R. S., Graphene Films with Large Domain Size by a Two-Step Chemical Vapor Deposition Process. *Nano Lett* **2010**, 10 (11), 4328-4334.
 20. Luo, Z. T.; Lu, Y.; Singer, D. W.; Berck, M. E.; Somers, L. A.; Goldsmith, B. R.; Johnson, A. T. C., Effect of Substrate Roughness and Feedstock Concentration on Growth of Wafer-Scale Graphene at Atmospheric Pressure. *Chem Mater* **2011**, 23 (6), 1441-1447.
 21. Kim, H.; Mattevi, C.; Calvo, M. R.; Oberg, J. C.; Artiglia, L.; Agnoli, S.; Hirjibehedin, C. F.; Chhowalla, M.; Saiz, E., Activation Energy Paths for Graphene Nucleation and Growth on Cu. *Acs Nano* **2012**, 6 (4), 3614-3623.
 22. Hwang, C.; Yoo, K.; Kim, S. J.; Seo, E. K.; Yu, H.; Biro, L. P., Initial

- Stage of Graphene Growth on a Cu Substrate. *J Phys Chem C* **2011**, *115* (45), 22369-22374.
23. Han, G. H.; Gunes, F.; Bae, J. J.; Kim, E. S.; Chae, S. J.; Shin, H. J.; Choi, J. Y.; Pribat, D.; Lee, Y. H., Influence of Copper Morphology in Forming Nucleation Seeds for Graphene Growth. *Nano Lett* **2011**, *11* (10), 4144-4148.
 24. Cho, S. Y.; Kim, M.; Kim, M. S.; Lee, M. H.; Kim, K. B., Effect of Cu surface treatment in graphene growth by chemical vapor deposition. *Mater Lett* **2019**, *236*, 403-407.
 25. Wang, H.; Wang, G. Z.; Bao, P. F.; Yang, S. L.; Zhu, W.; Xie, X.; Zhang, W. J., Controllable Synthesis of Submillimeter Single-Crystal Monolayer Graphene Domains on Copper Foils by Suppressing Nucleation (vol 134, pg 3627, 2012). *J Am Chem Soc* **2012**, *134* (44), 18476-18476.
 26. Yan, Z.; Lin, J.; Peng, Z. W.; Sun, Z. Z.; Zhu, Y.; Li, L.; Xiang, C. S.; Samuel, E. L.; Kittrell, C.; Tour, J. M., Toward the Synthesis of Wafer-Scale Single-Crystal Graphene on Copper Foils. *Acs Nano* **2012**, *6* (10), 9110-9117.
 27. Hao, Y. F.; Bharathi, M. S.; Wang, L.; Liu, Y. Y.; Chen, H.; Nie, S.; Wang, X. H.; Chou, H.; Tan, C.; Fallahazad, B.; Ramanarayan, H.; Magnuson, C. W.; Tutuc, E.; Yakobson, B. I.; McCarty, K. F.; Zhang, Y. W.; Kim, P.; Hone, J.; Colombo, L.; Ruoff, R. S., The Role of Surface Oxygen in the Growth of Large Single-Crystal Graphene on Copper. *Science* **2013**, *342* (6159), 720-723.
 28. Magnuson, C. W.; Kong, X. H.; Ji, H. X.; Tan, C.; Li, H. F.; Piner, R.; Ventrice, C. A.; Ruoff, R. S., Copper oxide as a "self-cleaning" substrate for

- graphene growth. *J Mater Res* **2014**, 29 (3), 403-409.
29. Gan, L.; Luo, Z. T., Turning off Hydrogen To Realize Seeded Growth of Subcentimeter Single-Crystal Graphene Grains on Copper. *Acs Nano* **2013**, 7 (10), 9480-9488.
 30. Geng, D. C.; Wu, B.; Guo, Y. L.; Huang, L. P.; Xue, Y. Z.; Chen, J. Y.; Yu, G.; Jiang, L.; Hu, W. P.; Liu, Y. Q., Uniform hexagonal graphene flakes and films grown on liquid copper surface. *P Natl Acad Sci USA* **2012**, 109 (21), 7992-7996.
 31. Geng, D. C.; Luo, B. R.; Xu, J.; Guo, Y. L.; Wu, B.; Hu, W. P.; Liu, Y. Q.; Yu, G., Self-Aligned Single-Crystal Graphene Grains. *Adv Funct Mater* **2014**, 24 (12), 1664-1670.
 32. Cho, S. Y.; Kim, M. S.; Kim, M.; Kim, K. J.; Kim, H. M.; Lee, D. J.; Lee, S. H.; Kim, K. B., Self-assembly and continuous growth of hexagonal graphene flakes on liquid Cu. *Nanoscale* **2015**, 7 (30), 12820-12827.
 33. Wu, Y. M. A.; Fan, Y.; Speller, S.; Creeth, G. L.; Sadowski, J. T.; He, K.; Robertson, A. W.; Allen, C. S.; Warner, J. H., Large Single Crystals of Graphene on Melted Copper Using Chemical Vapor Deposition. *Acs Nano* **2012**, 6 (6), 5010-5017.
 34. Xing, S. R.; Wu, W.; Wang, Y. A.; Bao, J. M.; Pei, S. S., Kinetic study of graphene growth: Temperature perspective on growth rate and film thickness by chemical vapor deposition. *Chem Phys Lett* **2013**, 580, 62-66.
 35. Fan, Y.; He, K.; Tan, H. J.; Speller, S.; Warner, J. H., Crack-Free Growth and Transfer of Continuous Monolayer Graphene Grown on Melted Copper. *Chem Mater* **2014**, 26 (17), 4984-4991.

CHAPTER 4.

Electrical properties of interface-engineered multilayer graphene

This chapter is based on the paper published in

ACS applied materials & interfaces

12, 30932-30940, (2020).

4.1. Introduction

Graphene has attracted great attention for electronic applications because of its fascinating properties. In particular, graphene has a high charge carrier mobility ($\sim 200,000 \text{ cm}^2/\text{Vs}$),¹ which enables the operation of field-effect transistors at very high frequencies,² and a low sheet resistance and high optical transparency ($\sim 97.7 \%$),³ which render it as a promising candidate for transparent conductive electrodes.⁴ With these applications in mind, substantial efforts have been devoted to enhancing the electrical properties of graphene by increasing the carrier mobility and/or the charge carrier density. The carrier mobility of graphene can be enhanced by synthesizing high-quality graphene by CVD (chemical vapor deposition) through epitaxial growth or by controlling the rates of nucleation and growth.⁵⁻¹⁰ In addition, various kinds of doping processes have been introduced to increase the carrier density.¹¹⁻¹⁶

One of the ways of forming a highly conductive graphene film is to increase the number of graphene layers, which also enhances its mechanical and chemical stability.^{17,18} Multilayer graphene can be easily obtained by CVD on catalytic metals with a high carbon solubility such as Ni. However, the direct growth of multilayer graphene by CVD does not assure uniformity in terms of the number of graphene layers.¹⁹ On the other hand, the multiple transfers of single-layer graphene yield high-quality multilayer graphene with uniform graphene layers. Despite the complicated transfer process, the obtained multilayer graphene has a low sheet resistance and high optical transmittance, which are useful for practical applications.

It has been reported that the sheet resistance of multilayer graphene (R_s^m) is inversely proportional to the number of graphene layers (N), which is explained by conventional conductivity theory in metals as shown in Eq (4-1).²⁰⁻

22

$$R_s^m = \frac{\rho}{t} = \frac{1}{n \cdot q \cdot \mu \cdot t} = \frac{1}{n \cdot q \cdot \mu \cdot (t_s \cdot N)} = \frac{1}{n_s \cdot q \cdot \mu \cdot N} = \frac{R_s^s}{N} \quad (4-1)$$

where, ρ , t , n , q , and μ , is resistivity, multilayer thickness, charge carrier concentration (#/cm³), unit charge (1.6×10^{-19} C), and charge carrier mobility (cm²/Vs), respectively. And, R_s^s , t_s , $n_s (= n \times t_s)$ is a sheet resistance, thickness, and sheet carrier density (#/cm²) of single-layer graphene, respectively. In other words, R_s^m is equal to the parallel addition of R_s^s .²³ At this time, the important assumption is that each graphene layer has the same physical properties such as n_s and μ .

However, understanding the reduction of R_s^m with the increase of N is not so simple because the n_s and μ of graphene significantly depends on the surface and interface properties.²⁴⁻²⁶ Firstly, unintentional doping of the graphene surface is caused by PMMA residues during the transport process²⁷ and physical adsorption of oxygen and water molecules from the air.²⁸ Therefore, in the case of multilayer graphene, it can be assumed that the n_s of the top graphene layer is higher than that of the inner graphene layers. In addition, the μ also varies depending on charge scattering by the dangling bonds or charge traps of substrate.²⁹ The highest μ of 200,000 cm²/Vs was obtained at suspended graphene without the scattering effect by the substrates.¹ A graphene device on a hexagonal boron nitride substrate shows

almost an order of magnitude higher μ than that of the devices on SiO₂ substrates.³⁰ These results suggest that μ of the bottom layer can be considerably differ from that of other layers. Furthermore, the electrical characteristic of the inner graphene layers surrounded by other graphenes varies greatly depending on the stacking order because of the modification of band structure. It has been reported that the μ of AB-stacked multilayer graphene is lower than that of monolayer graphene due to the nonlinear band dispersion.³¹ On the other hand, the μ of turbostratic stacked multilayer graphene is reported to be higher than that of monolayer graphene even without the deformation of band structure by the suppression of carrier scattering by the first layer graphene.³²⁻³⁴ Consequently, not all the layers in multilayer graphene have the same n_s and μ according to their surface and interface properties.

To this end, we systematically investigated the electrical properties of multilayer graphene by modulating the number of layers as well as interlayer doping state to figure out the effects of inhomogeneity of each sublayer on the electrical properties of layer-by-layer stacked graphene. As mentioned above, the outer and inner graphene layers on interlayer intentionally undoped multilayer graphene might have different electrical characteristics. Since increasing the number of layers increases the number of interfaces, the effects of inner and outer layers on the properties of multilayer graphene can be evaluated by varying the number of layers. On the other hand, interlayer doping not only yields graphene layers with almost similar electrical properties but also limits the interaction between the graphene layers. Thus, it is expected to show a different trend from dopant free multilayer graphene. The R_s , n_s and μ were systematically measured and analyzed by Hall effect measurements and using a model of Hall effect in the hetero-junction. To prepare multilayer graphene with

different interfaces, we adopted two different methods of layer stacking. One is the interface residue-free layer-by-layer stacking transfer to minimize the unwanted doping effect, and the other is the interlayer doping during the transfer of individual layers using benzimidazole, a p-type dopant.^{21,35} In addition, by doping the exposed graphene surface with benzimidazole, the effect of the surface doping level on the electrical properties was investigated. And, the effect of polymer residue between graphene layers was also investigated by applying for thermal release tape transfer. Furthermore, partial-coverage graphene layers were stacked on the full-coverage graphene layers, and the electrical properties of the graphene with mixed (series and parallel) conduction channels were determined. Finally, we determined the parameters that enhance the electrical properties depending on the dopant position in multilayer graphene.

4.2. Experimental details

4.2.1. Synthesis of partial and full-coverage monolayer graphene

The growth of partial and full-coverage monolayer graphene by CVD on Cu foils (Alfa Aesar #13382) was controlled by the following method. Before growing the graphene, as-received Cu foils cut into the size of $4 \times 4 \text{ cm}^2$ were electropolished in the electrolyte at the voltage of 5 V for 120 s. The electrolyte was composed of 100 mL of water, 50 mL of orthophosphoric acid, 50 mL of ethanol, 10 mL of isopropyl alcohol, and 1 g of urea. After electropolishing, the Cu foil was rinsed with deionized water, washed with ethanol, and blow-dried with nitrogen. An electropolished Cu foil was loaded into a quartz-type tube furnace (Lindberg, blue), and the chamber was evacuated to a base pressure of approximately 10^{-3} Torr. Then, 20 sccm (standard cubic centimetre per min) of hydrogen (H_2) and 50 sccm of argon (Ar) were introduced into the chamber, and the Cu foil was annealed at 1030°C for 30 min. Subsequently, graphene growth was commenced by flowing 0.5 sccm of methane (CH_4) in an ambient of 12 sccm of H_2 and 50 sccm of Ar. The graphene coverages were 20, 38 and 84% for growth times of 3, 5, and 7.5 min, respectively. To obtain full-covered graphene, the growth time of 30 min was applied with the growth conditions above, then the CH_4 flow rate was increased to 1 sccm for another 30 min. Working pressure of entire growth processes were 5×10^{-2} Torr.

4.2.2. Graphene transfer (layer-by-layer stacking) and chemical doping

To form multilayer graphene without a polymer residue between the layers, we adopted the layer-by-layer transfer method proposed by Wang et al.;²¹ the schematic of the fabrication process is shown in **figure 4-1**. First, PMMA was spin-coated onto the as-grown graphene on Cu, and the Cu was etched using a 0.1 M ammonium persulfate ((NH₄)₂S₂O₈) solution to obtain a dopant-free interface. To fabricate the interlayer-doped sample, benzimidazole (C₇H₆N₂) powder (0.06 M) was added to the Cu-etching solution (ammonium persulfate (0.1 M) + H₂SO₄ + H₂O₂). Thus, the graphene was doped simultaneously during the etching of Cu. After Cu etching, to wash off the acid contaminants, PMMA/graphene layer was rinsed with deionized water for 30 min. Then, the PMMA/graphene layer was transferred onto another set of graphene/Cu samples. Again, the Cu was etched in the same manner as stated above for the undoped or doped samples. By repeating the transfer process, multilayer graphene samples with the desired number of layers were fabricated. After transfer to the target substrate, the PMMA of undoped multilayer graphene was removed by directly heating the samples in the air at 400 °C for 4 hours. However, due to the low melting point of the benzimidazole molecule of 170 °C, PMMA of doped multilayer graphene was removed in acetone.

In addition, in order to confirm the effect of the interlayer polymer residue on the electrical properties of graphene, 1 to 4 layers of multilayer graphenes were prepared by using thermal release tape. As shown in **figure 4-2**, graphene/Cu attached to the tape was transferred one by one onto the SiO₂ substrate after etching the Cu by ammonium persulfate.

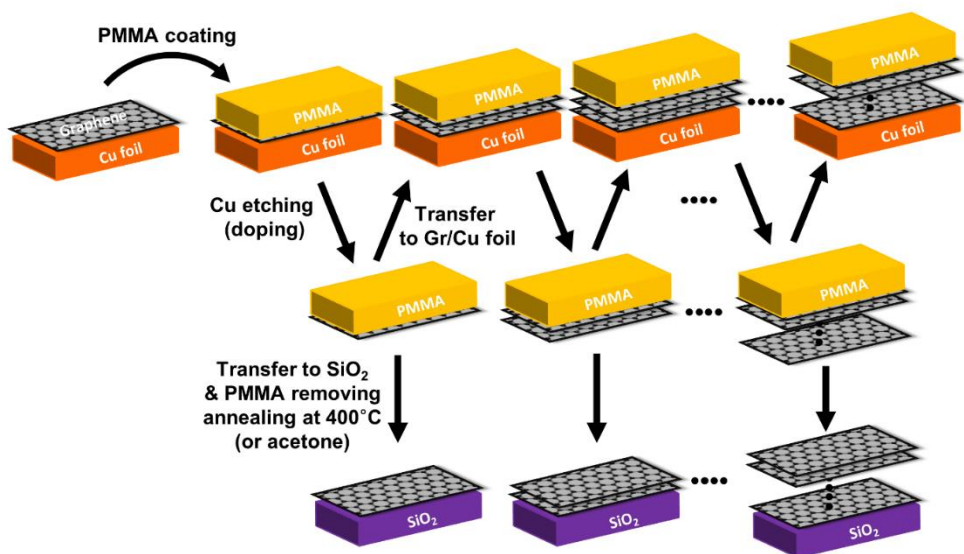


Figure. 4-1. Schematic diagram showing graphene transfer by layer-by-layer stacking. Two types of multilayer graphene samples preparation: interlayer-undoped and interlayer doped multilayer graphene.

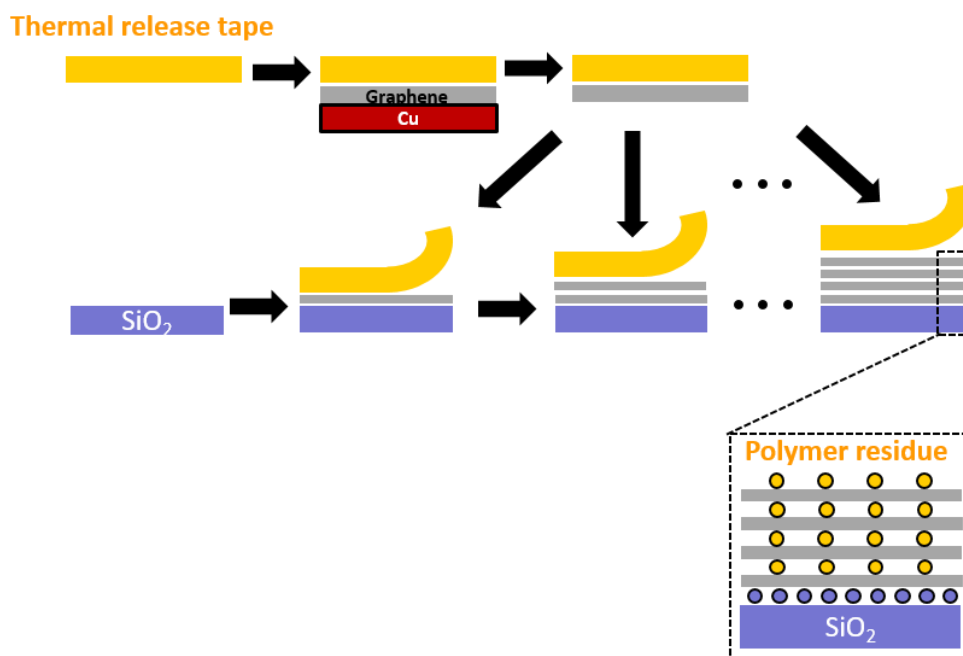


Figure. 4-2. Schematic diagram showing interlayer polymer residue existed multilayer graphene transferred by using thermal release tape.

4.2.3. Characterization

The multilayer graphene was transferred to a thermally grown SiO₂ surface (285 nm thickness) on a Si substrate. The sheet resistance, Hall mobility, and sheet carrier density were measured using the van der Pauw structure, size of 9 × 9 mm. 1 mm sized metal contacts were formed by silver paste. Hall measurements were performed under a 0.5 T magnetic field (HL 5500PC, BIO-RAD) at room temperature. Raman spectra were measured using a UniRam system with a diode-pumped solid-state laser (100 mW, 532 nm). For optical property measurements, another set of graphene samples was transferred onto a quartz substrate and the transmittance was measured using a Cary 5000 UV–vis–NIR spectrophotometer (Varian). XPS data were collected using an AXIS-HIS system (Kratos, Inc.) with Mg K α radiation.

4.3. Results and discussion

4.3.1. Characterizations of inter-layer doped and undoped multilayer graphene

Single-layer graphene was used for the stacking was synthesized by a two-step growth process. **Figure 4-3(a)-(e)** shows the optical images of graphene on Cu grew with increasing growth time after 1 min selective Cu oxidation at 180 °C under air. The lateral size of the grain is approximately $\sim 50\text{ }\mu\text{m}$. After transfer the fully grown graphene on SiO_2 , the add-layers can be observed as shown in **figure 4-3(f)**. Although the lateral size of the add-layers grew up to $15\text{ }\mu\text{m}$, the average coverage is 2% and the single layer is predominant.

Prior to electrical characterization, the physical and chemical states of the multilayer graphene depending on the graphene interface were investigated. **Figure 4-4(a)** shows the schematic diagram of the interlayer-undoped multilayer graphene (*u*-MLG) and interlayer-doped multilayer graphene (*d*-MLG). The *u*-MLG is assumed to have a pristine and clean interface between the graphene layers due to layer-by-layer stacking, while the *d*-MLG is assumed to have a considerable amount of benzimidazole molecules adsorbed between the graphene layers because of the repeated molecular doping and stacking of individual graphene layers. Nevertheless, as shown in **Figure 4-5**, the optical microscope image does not show a significant difference between *u*-MLG and *d*-MLG even if the number of layers increases.

Figure 4-4(b) shows the optical transmittances of the *u*-MLG and *d*-MLG samples at the wavelength of 550 nm with the number of graphene layers (*N*). The transmittance of the *u*-MLG is well-matched with the black dotted line which

represents a 2.4% reduction in transmittance per additional graphene layer due to intra-band optical transitions. This is similar to that of pristine graphene (2.3% reduction in transmittance per graphene layer). In contrast, interlayer doping reduces the transmittance by approximately 3.1% per additional layer, presumably due to the scattering of photons by the adsorbed benzimidazole molecules. The chemical states of undoped single-layer graphene (*u*-SLG) and doped single-layer graphene (*d*-SLG) were investigated by XPS. The C 1s signal shown in **figure 4-4(c)** could be deconvoluted into several peaks for both samples. The five peaks at 284.5, 285.4, 286.6, 287.6, and 288.6 eV were attributed to the C-C (sp^2), C (sp^3), C-O, C=O, and O=C-OH bonds, respectively.^{36,37} The relative area of the peak at 285.4 eV increased upon doping, which indicates that the adsorption of benzimidazole generated more sp^3 -type carbon bonds. Moreover, the clear N 1s peak of the *d*-SLG in **figure 4-4(d)** indicates that the benzimidazole molecules are sandwiched between the graphene and substrate.³⁵

To compare the quality of the *u*-SLG and *d*-SLG samples, Raman spectroscopy was performed, which is shown in **figure 4-6(a)**. The intensity of the D band ($\sim 1350\text{ cm}^{-1}$) is negligibly small for *u*-SLG, the average $I_D(\sim 1350\text{ cm}^{-1})/I_G(\sim 1580\text{ cm}^{-1})$ ratio is $0.11(\pm 0.01)$, which indicates that the defect density of *u*-SLG is relatively small. After doping, due to the C-H and C-N bond vibration of underlying benzimidazole, the spectral near the D band region increased.^{38,39} The blue-shifts of both the G and 2D bands ($+8.4$ and $+12.4\text{ cm}^{-1}$, respectively), as shown in **figure 4-6(b)**, indicates that adsorption of benzimidazole result the noticeable p-type doping.⁴⁰ Reduction of the $I_{2D}(\sim 2700\text{ cm}^{-1})/I_G(\sim 1580\text{ cm}^{-1})$ ratio is also known as evidence of doping.⁴¹ The representative Raman spectra of *u*-MLG and *d*-MLG from 1 to 4 layers are shown in **figure 4-6(d)** and **(e)**, respectively. In both cases, it seems that all band intensities

increased in proportion to the number of layers. However, the average I_{2D}/I_G ratios obtained by randomly selecting 30 points are different. The I_{2D}/I_G ratios of the two sets of samples are plotted as a function of N in **figure 4-4(c)**. For the *u*-MLG, the average I_{2D}/I_G ratio slightly decreased from 1.7 ± 0.3 to 1.3 ± 0.8 . Even though the graphene was randomly transferred, the decrease in the I_{2D}/I_G ratio with increasing N implies Bernal stacking.^{42,43} It is noteworthy that the I_{2D}/I_G ratios of the Bernal stacked bilayer and quadruple layer graphenes were experimentally obtained as 0.75 and 0.53, respectively.^{44,45} However, the average I_{2D}/I_G ratio of the quadruple layer fabricated in this study was 1, which indicates that the Bernal stacking area is still small compared to randomly stacked multilayer region with the same I_{2D}/I_G ratio as that of the monolayer graphene.⁴ On the other hand, in the case of *d*-MLG, the I_{2D}/I_G ratios were constant regardless of the number of layers. It is believed that existing doping molecules between graphene layers inhibit graphene layer coupling. As shown in **figure 4-6(f)**, the full width of half maximum of the 2D band of *u*-MLG and *d*-MLG also indicates a similar tendency.

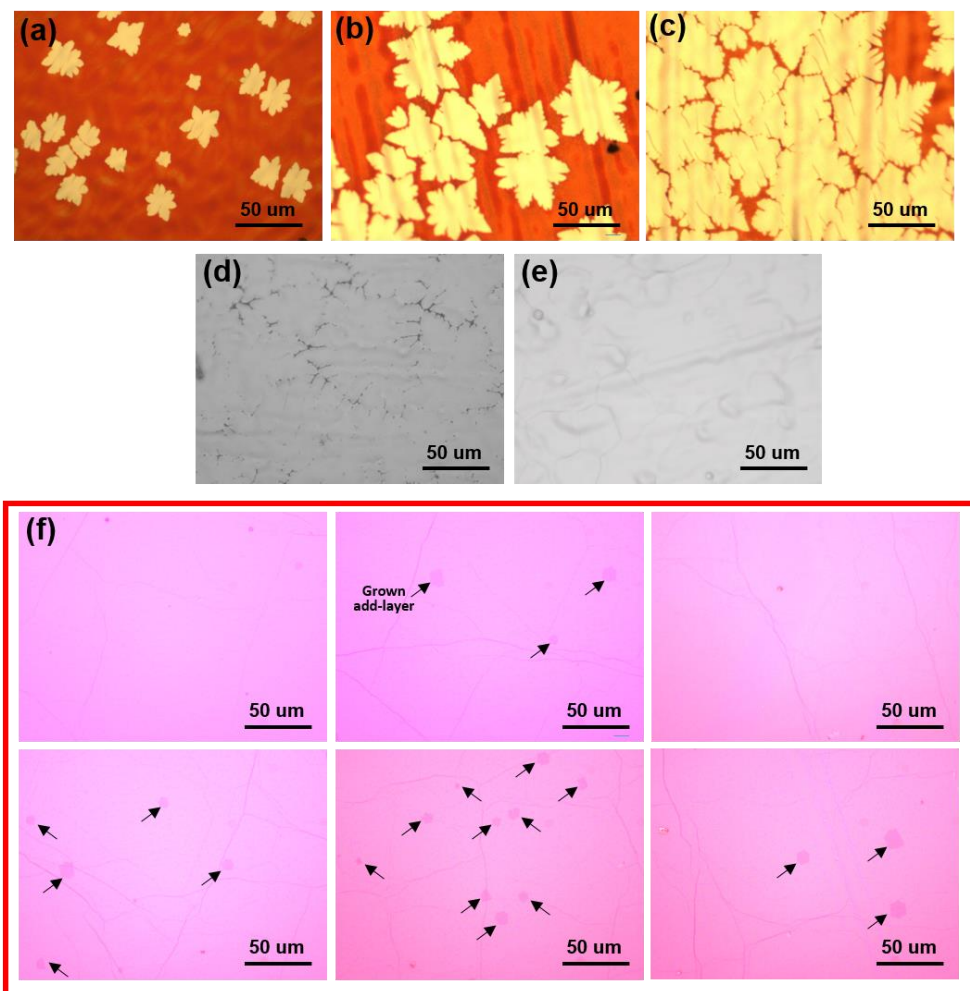


Figure. 4-3. Optical microscope images of graphene on selectively oxidized Cu foil after (a) 3, (b) 5, (c) 7.5 and (c) 20 min of first growth step and (e) two-step growth. (f) Optical microscope images which area is randomly selected of single-layer graphene transferred on SiO₂/Si.

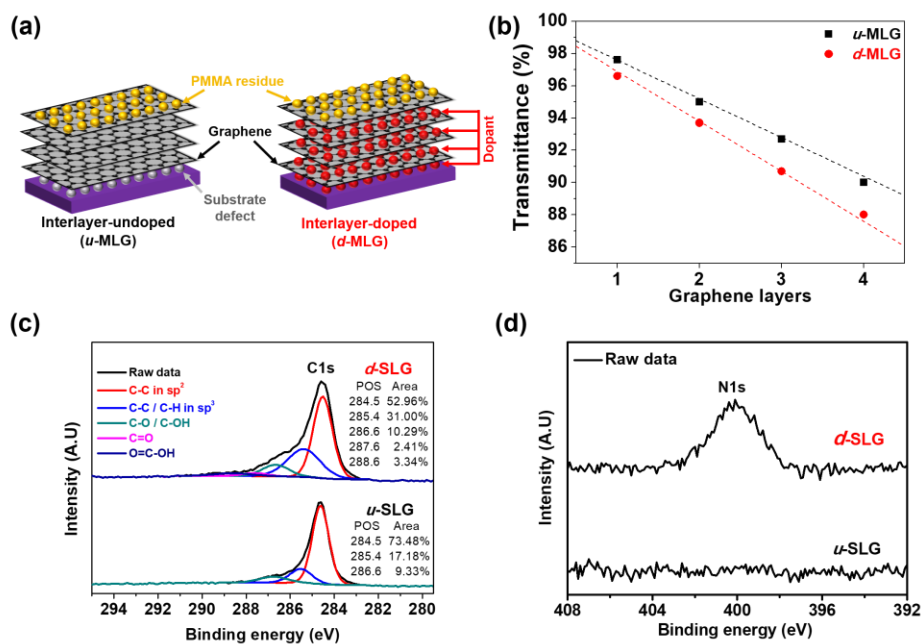


Figure. 4-4. (a) Schematic diagram of *u*-MLG and *d*-MLG. The *u*-MLG has surface residues while in *d*-MLG, benzimidazole molecules are adsorbed between the graphene layers. (b) Optical transmittance at 550 nm as a function of the number of graphene layers. XPS spectra of *u*-SLG and *d*-SLG: (c) C 1s peak and (d) N 1s peak.

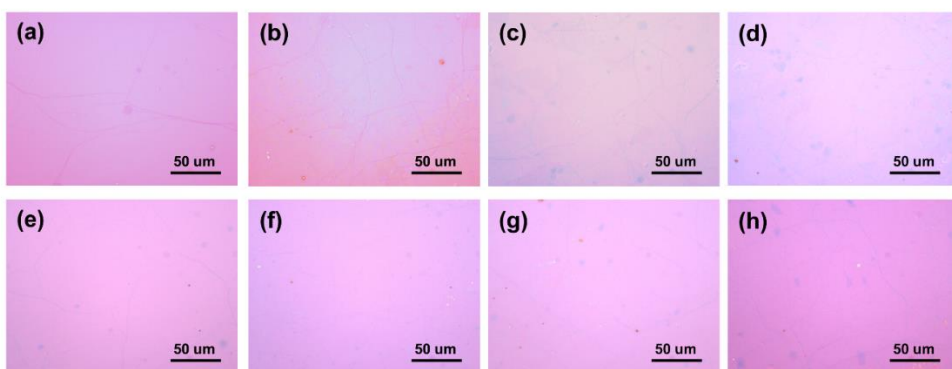


Figure. 4-5. Optical microscope images of u-MLG (a) 1 layer, (b) 2 layers, (c) 3 layers, (d) 4 layers and d-MLG (e) 1 layer, (f) 2 layers, (g) 3 layers, (h) 4 layers after transferred on SiO_2/Si .

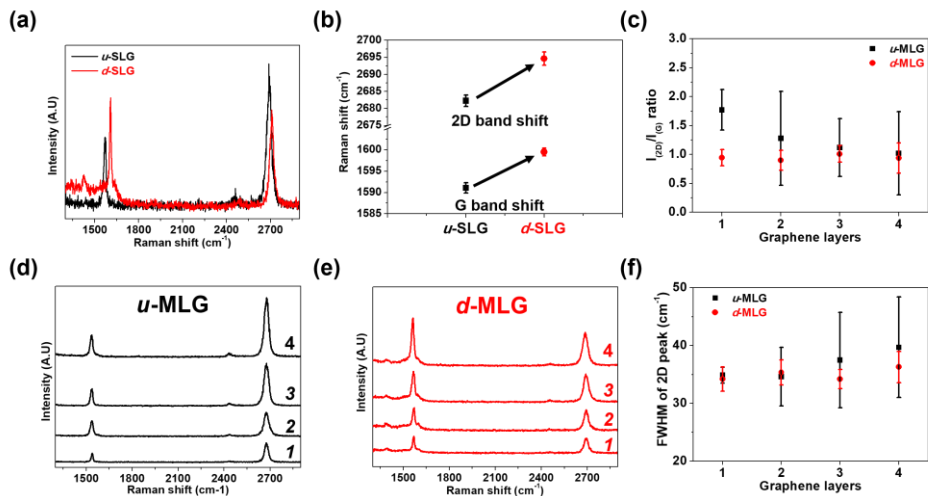


Figure. 4-6. Raman spectrum analysis of graphene (a) Raman spectrum of *u*-SLG and *d*-SLG. (f) blueshifts of G and 2D band after doping. (g) The ratio of the 2D to G band intensities (I_{2D}/I_G) as a function of the number of graphene layers. Raman spectra of (a) *u*-MLG from 1 to 4 layers and (b) *d*-MLG from 1 to 4 layers. (c) FWHM of 2D band of *u*-MLG and *d*-MLG as a function of the number of graphene layers.

4.3.2. Electrical properties of inter-layer doped and undoped multilayer graphene

We investigated the variation in the R_s^m of u -MLG and d -MLG as a function of N which is shown in **figure 4-7(a)**. The R_s^m of u -MLG and d -MLG decrease from 705 to 104 Ω/sq and from 250 to 25 Ω/sq with an increase in N from 1 to 12, respectively. As expected, the R_s^m in both cases decreased with increasing N , although the R_s^m of the d -MLG are much lower than that of u -MLG. According to the conventional conductivity theory previously mentioned in Eq.(4-1), calculated $R_s^m (= R_s^s/N)$ are plotted as dotted lines in Figure 3(a) where R_s^s of u -MLG and d -MLG are 705 and 250 Ω/sq , respectively. In the case of d -MLG, measured R_s^m matches well with calculated R_s^m , which indicates that all the graphene layers have identical electrical properties. On the other hand, in the case of u -MLG, the difference between measured and calculated R_s^m increased with increasing N , finally measured R_s^m of 12 layers graphene (104 Ω/sq) shows almost 2 times higher than calculated R_s^m (58 Ω/sq). It is believed that the electrical properties of the added layers are different from that of the first layer in u -MLG.

In order to reveal the origin of R_s^m reduction as a function of N , the sheet carrier density (n_s) and the carrier mobility (μ) were investigated by the Hall measurement, which is shown in **figure 4-7(b)** and **(c)**, respectively. In the case of d -MLG, the n_s linearly increased as a function of N with a slope = $1.6 \times 10^{13}/\text{cm}^2$, and finally reached $1.97 \times 10^{14}/\text{cm}^2$ for the graphene with 12 layers. The μ remained constant at approximately 1400 cm^2/Vs irrespective of N . This result shows that n_s and μ of each graphene layer in d -MLG is the same as those of d -SLG, which is well conducted the R_s^m reduction matched by conventional conductive theory. In

contrast, *u*-MLG exhibited an almost constant n_s of $1 \times 10^{13}/\text{cm}^2$ irrespective of N . Twelve layers of the *u*-MLG show $n_s=1.4 \times 10^{13}/\text{cm}^2$, which is only $0.6 \times 10^{13}/\text{cm}^2$ higher than that of *u*-SLG. The μ of *u*-MLG almost linearly increased with increasing N from $1040 \text{ cm}^2/\text{Vs}$ for *u*-SLG to $3100 \text{ cm}^2/\text{Vs}$ for quadruple layers, and then saturated to the value of about $4000 \text{ cm}^2/\text{Vs}$ for 12 layers *u*-MLG. Consequently, the reduction of R_s^m of *d*-MLG and *u*-MLG is governed by the increase of n_s and μ , respectively.

The reason why *u*-MLG does not follow the conventional conductivity theory is believed that the surrounding environment of each graphene in *u*-MLG is different as described above introduction part. In our experiment, n_s of *u*-SLG ($\sim 10^{13} / \text{cm}^2$) shows a relatively high value, which is known that PMMA residues and/or $\text{H}_2\text{O}/\text{O}_2$ molecules adsorption caused p-doping of the graphene by the electron transfer reaction involving the $\text{H}_2\text{O}/\text{O}_2$ redox couple on the graphene surface.^{27,28} Moreover, our sample preparation scheme only allowed the top-most layer to have PMMA residues, which indicates that the unintentional doping of graphene mainly occurred at the surface. Hence, the inner graphene layers have relatively lower n_s than the top graphene layer and then, the total n_s is expected to be almost constant irrespective of N . The increasing μ of *u*-MLG as stacking the graphenes indicates that the μ reduction effect due to band structure change by Bernal stacking is negligible, which is the same as the result of Raman spectrum in **figure 4-6(g)**. Therefore, the μ is affected by the carrier density or surface defects of each layer. So, the addition of inner layers with a low n_s improves the μ by reducing both the impurity-induced scattering and substrate defect induced scattering to the overall charge carrier conduction simultaneously.

To confirm the change in carrier mobility due to the electrical inhomogeneity of the layers, we introduce the model of the Hall effect in the heterojunction.^{46,47,48} When N -layers of p-type graphene exist without contact resistance, the Hall coefficient is represented as Eq. (4-2):

$$R_{H,N} = \frac{\mu_{h1}^2 p_1 + \mu_{h2}^2 p_2 + \cdots + \mu_{hN}^2 p_N}{q(\mu_{h1} p_1 + \mu_{h1} p_2 + \cdots + \mu_{hN} p_N)^2} \quad (4-2)$$

$$= \frac{1}{q p_{tot,N}} = \frac{\mu_{tot,N}}{\sigma_{tot,N}} \quad (4-3)$$

where μ_{hN} , p_N is the Hall mobility and sheet carrier density of N^{th} graphene layer. If the physical properties of all layers are the same, i.e. $\mu_{h1} = \mu_{h2} = \cdots = \mu_{hN}$ and $p_1 = p_2 = \cdots = p_N$, Eq. (4-2) is the same as Eq. (4-1) which is shown in Eq. (4-3), where $p_{tot,N}$, $\mu_{tot,N}$, and $\sigma_{tot,N} (= \mu_{h1} p_1 + \mu_{h1} p_2 + \cdots + \mu_{hN} p_N)$ are Hall mobility, sheet carrier density, and sheet conductance of N -layer graphene, respectively. In our u -MLG case, the top layer graphene is exposed to air, the bottom layer graphene attached to the substrate, and the inner layer graphenes are surrounded by other graphenes. Therefore, assuming that the physical properties of the top layer graphene (μ_{h1} and p_1) and bottom layer graphene (μ_{h2} and p_2) are different from that of the inner graphene layers (μ_{h3} and p_3), the Hall mobility of our multi-structure is as follows Eq. (4-4):

$$\mu_{tot,N} = \frac{p_1 \mu_{h1}^2 + p_2 \mu_{h2}^2 + (N-2) p_3 \mu_{h3}^2}{p_1 \mu_{h1} + p_2 \mu_{h2} + (N-2) p_3 \mu_{h3}} \quad (4-4)$$

The Eq. (4-4) can be simplified to Eq. (4-5) by applying $\mu_{tot,2} = (p_1 \mu_{h1}^2 +$
1 1 9

$p_2\mu_{h2}^2)/(p_1\mu_{h1} + p_2\mu_{h2})$ and $K = (p_3\mu_{h3})/(p_1\mu_{h1} + p_2\mu_{h2}) = (p_3\mu_{h3})/(\mathbf{p}_{tot,2}\mu_{tot,2})$ which are the mobility of double-layer graphene and the conductance ratio of inner and double (top and bottom) layers, respectively.

$$\mu_{tot,N} = \frac{\mu_{tot,2} + K\mu_{h3}(N - 2)}{1 + K(N - 2)} \quad (4 - 5)$$

$$\lim_{N \rightarrow \infty} \mu_{tot,N} = \lim_{L \rightarrow \infty} \frac{\mu_{tot,2} + K\mu_{h3}(N - 2)}{1 + K(N - 2)} = \mu_{h3} \quad (4 - 6)$$

The fitting of the variation in carrier mobility, as indicated by the black dotted line in **figure 4-7(c)** by introducing measured $\mu_{tot,2} = 2288 \text{ cm}^2/\text{Vs}$ yields $\mu_{h3} = 500 \text{ cm}^2/\text{Vs}$ and $K = 0.18$. From the conductance ratio of $K = 0.18$ and measured $\mathbf{p}_{tot,2} = 7.92 \times 10^{12}/\text{cm}^2$, the inner layer carrier density was calculated as $p_3 = 6.05 \times 10^{11}/\text{cm}^2$. Using this number of p_3 , the carrier density of *u*-MLG with more than two layers was calculated, as shown in **figure 4-7(b)** and **(d)** as the black dotted line, which coincides with the experimental result. Further, for an infinite number of layers, the carrier mobility saturates to μ_{h3} as shown in Eq. (4-6). It clearly confirmed that the inner graphenes have high mobility ($5000 \text{ cm}^2/\text{Vs}$) with low carrier density ($6.05 \times 10^{11}/\text{cm}^2$).

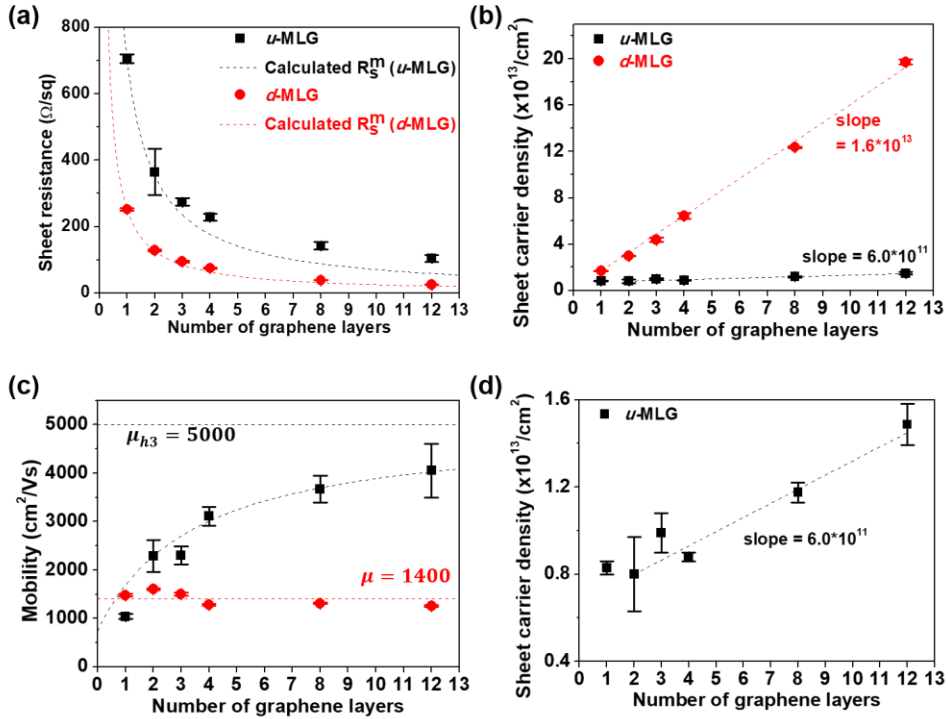


Figure 4-7. The electrical property of *u*-MLG and *d*-MLG. (a) Sheet resistance, (b) sheet carrier density, and (c) carrier mobility of *u*-MLG (black) and *d*-MLG (red). And (d) separately magnified sheet carrier density of *u*-MLG. The dotted lines represent the calculated results.

4.3.3. Undoped multilayer graphene surface doping with dopant

To further confirm the effect of the surface doping level on the electrical properties and to investigate whether the mobility and carrier density could be separately tuned, as shown in **figure 4-8(a)**, we doped the top surface of the *u*-MLG samples by dropping a benzimidazole solution as droplets on the *u*-MLG for 8h. **Figure 4-8(b)-(d)** shows the electrical properties of the *u*-MLG with and without top layer doping. Regardless of the number of graphene layers, the sheet resistance decreased after doping, as shown in Figure 4(a). While the sheet resistance of monolayer decreased by 34% (from 705 to 463 Ω/sq), the sheet resistance of the quadruple-layer decreased by 51% (from 190 to 90 Ω/sq) with concomitant changes in the carrier mobility and density [**figure 4-8(c) and (d)**]. Again, with the doping of the top graphene layer, the carrier density increases from $8 \times 10^{12}/\text{cm}^2$ to $3.0 \times 10^{13}/\text{cm}^2$, irrespective of the number of graphene layers. At the same time, the carrier mobility decreased by approximately 450 cm^2/Vs irrespective of the number of layers. This uniform decrease in carrier mobility indicates that the charged impurity scattering due to the increase in doping concentration only occurred on the top layer.⁴⁹ These results confirmed that the electrical properties of multilayer graphene do not simply depend on the number of graphene layers, but can be tuned by designing the transfer and doping processes.

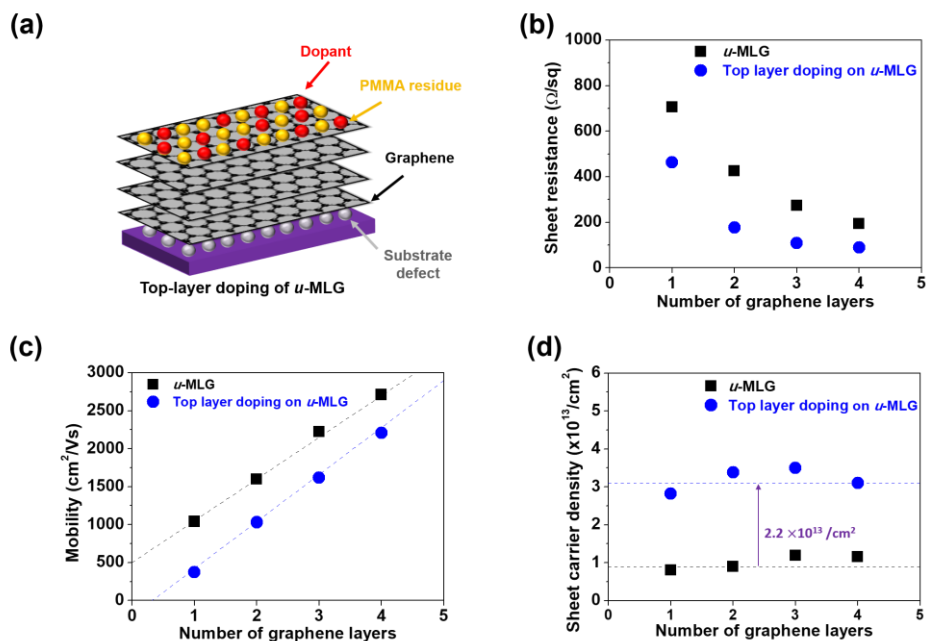


Figure. 4-8. (a) Schematic diagram of surface doped u -MLG with benzimidazole molecules. Electrical properties of u -MLG (black) and top-layer doping of u -MLG (blue): (b) sheet resistance, (c) carrier mobility, and (d) carrier density.

4.3.4. Multilayer graphene with inter-layer polymer residues

Then, if polymer residues other than dopant molecules exist in the interlayer, graphene was transferred one by one on SiO₂ substrate using a thermal release tape to investigate how it affects the electrical properties of graphene. In the case of preparing multilayer graphene with thermal release tape, it is expected that there will be residue by the tape because the graphene of all layers undergoes adhesion and desorption process with the tape, and it is shown as a schematic image in **figure 4-9(a)**. It indicates that polymer residues exist between the inner graphenes. The electrical properties are shown in **figure 4-9(b)** to **(d)**. As shown in **figure 4-9(b)**, the sheet resistance decrease from 417 to 149 Ω/sq with an increase in the number of graphene layers from 1 to 4. However, as shown in **figure 4-9(c)** and **(d)**, carrier mobility is constant at 1100 cm^2/Vs , and linearly increased carrier density with a slope of $9.0 \times 10^{12}/\text{cm}^2$ decreases the sheet resistance. It indicates that each layer has the identical carrier mobility and carrier density of 1100 cm^2/Vs and $9.0 \times 10^{12}/\text{cm}^2$, respectively. It is worth noting that the behaviour of electrical properties according to the number of graphene layers is the same as that of *d*-MLG. In other words, when polymer residues are adsorbed on the inner layers, they act as dopants so, it increases the carrier density but decreases mobility.

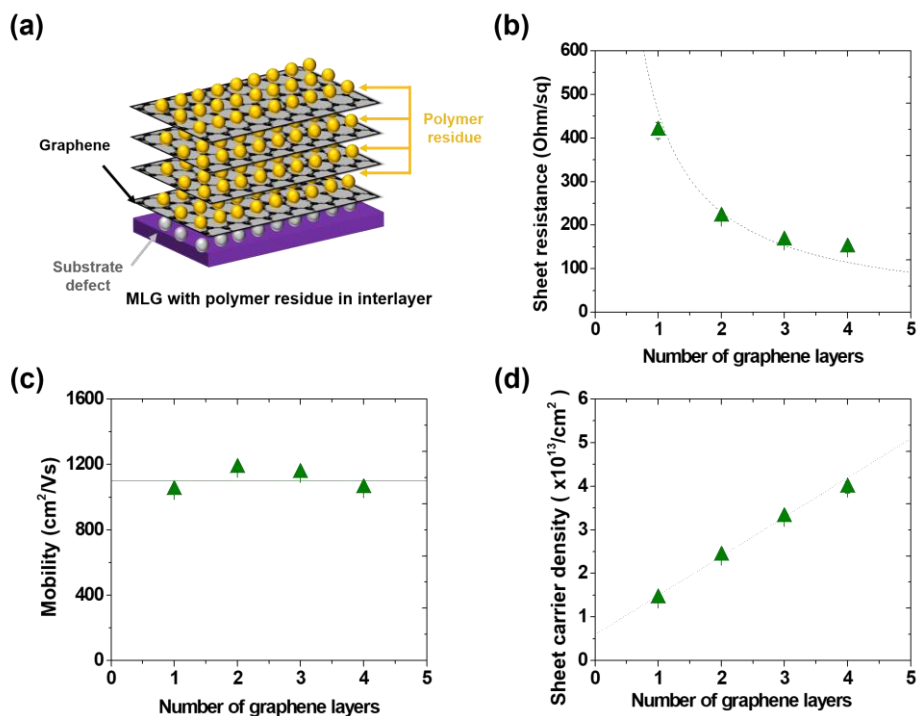


Figure. 4-9. (a) Schematic diagram of MLG with polymer residue in the interlayers. Electrical properties of MLG with polymer residue in the interlayers: (b) sheet resistance, (c) carrier mobility, and (d) carrier density.

4.3.5. Double layer graphene with different 2nd layer coverage

So far, we have investigated the effect of interface and surface doping on the electrical properties of stacked continuous monolayer graphenes having parallel conduction channels. Finally, we investigated the electrical properties of graphene with mixed (parallel and series) conduction channels. To prepare mixed conduction channels, we stacked interlayer-undoped graphene layers to fabricate bilayer graphene with different second layer coverages of 0, 20, 38, 84, and 100%. The optical microscope images of the layer stacked graphene is shown in **figure 4-10(a)**. The dendritic shape of the additional layer graphene can be easily distinguished by optical contrast. This mixed conduction channel can be modeled as a series conduction path of mono and double-layer graphene. The sheet resistance of the graphene with mixed conduction channels as a function of double-layer fraction (f) which shown in **figure 4-10(b)** can be represented as:

$$R_{s,tot} = R_{s,1} \cdot (1 - f) + R_{s,2} \cdot f \quad (4 - 7)$$

where $R_{s,1}$ and $R_{s,2}$ are the sheet resistances of monolayer and double layer, respectively, and $R_{s,tot}$ is the total sheet resistance. The experimental results [**Figure 4-10(c)**] showed that the sheet resistance gradually decreased from 705 to 364 Ω/sq . This is consistent with the Eq. (4-7) shown as the dotted line. The sheet resistance decreased due to an increase in the double-layer fraction [**Figure 4-10(d)**]. Moreover, the sheet carrier density remained almost constant ($\sim 8 \times 10^{12}/\text{cm}^2$) irrespective of the coverage of the second layer. These results show conclusively that the decrease in sheet resistance originates from the enhancement of the carrier mobility.

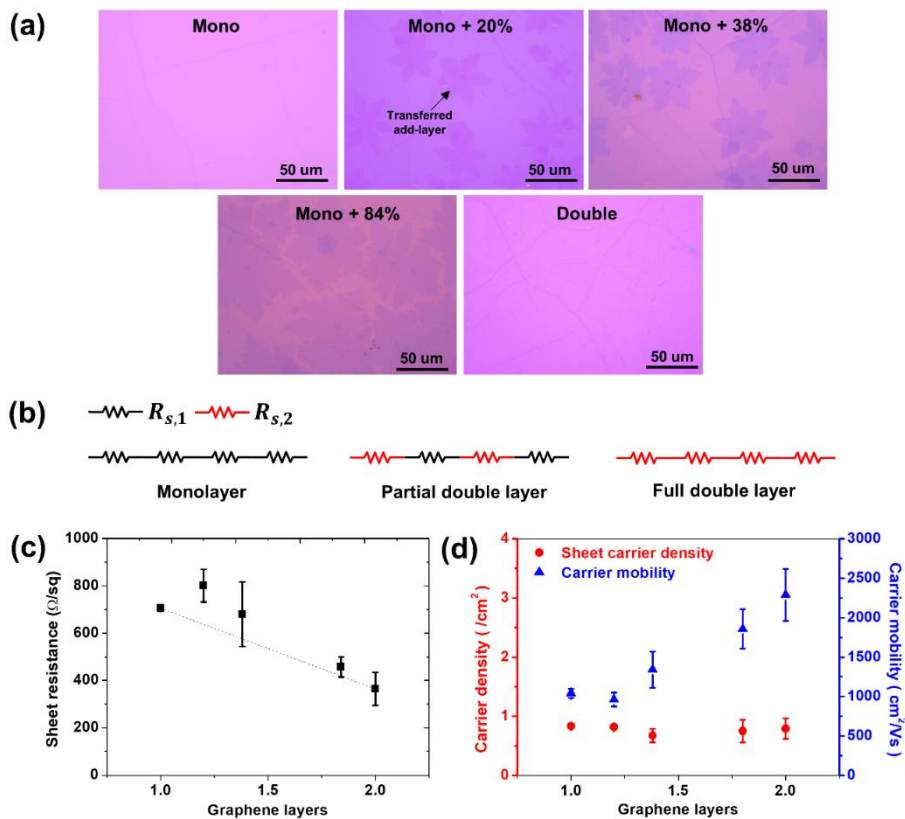


Figure. 4-10. (a) Optical microscope images of graphene transferred on SiO₂/Si by varying the additional layer coverage. (b) Resistor models of single-layer to double-layer graphene with increasing second-layer coverage. Black and red resistors represent sheet resistance of monolayer and double-layer graphene. (c) Variation in sheet resistance of the samples with different additional layer coverages, and (d) the corresponding variations in sheet carrier density (red) and carrier mobility (blue).

4.4. Summary and conclusion

We investigated the variation in the sheet resistance of multilayer graphene with and without interlayer doping. The origin of the sheet resistance variation was determined by Hall measurements. Overall, we found that the sheet resistance decreased gradually with an increase in the number of graphene layers in both cases. However, the Hall measurements showed that the main factors contributing to the sheet resistance reduction in the two cases are different. The layer-stacked graphene with interlayer doping (*d*-MLG) showed a decrease in sheet resistance by the increase of sheet carrier density with the increase of the number of the graphene layer. This is well-matched to the conventional conductivity theory of metals assuming the identical physical properties in each graphene layer. The multilayer graphene without the interlayer molecular doping (*u*-MLG) showed an increase in carrier mobility with the number of graphene layers, while the sheet carrier density remained almost constant. This result means that each graphene layer has different physical properties such as sheet carrier density and carrier mobility, and the characteristics of each graphene layer can be extracted by the calculation of Hall mobility at the heterojunction. Further, we confirmed the separate controllability of doping concentration and mobility enhancement in multilayer graphene by doping the top layer of the interlayer-undoped graphene and multilayer graphene with mixed conduction channels.

References

1. Bolotin, K. I.; Sikes, K. J.; Jiang, Z.; Klima, M.; Fudenberg, G.; Hone, J.; Kim, P.; Stormer, H. L., Ultrahigh electron mobility in suspended graphene. *Solid State Commun* **2008**, *146* (9-10), 351-355.
2. Lin, Y. M.; Dimitrakopoulos, C.; Jenkins, K. A.; Farmer, D. B.; Chiu, H. Y.; Grill, A.; Avouris, P., 100-GHz Transistors from Wafer-Scale Epitaxial Graphene. *Science* **2010**, *327* (5966), 662-662.
3. Nair, R. R.; Blake, P.; Grigorenko, A. N.; Novoselov, K. S.; Booth, T. J.; Stauber, T.; Peres, N. M. R.; Geim, A. K., Fine structure constant defines visual transparency of graphene. *Science* **2008**, *320* (5881), 1308-1308.
4. Bae, S.; Kim, H.; Lee, Y.; Xu, X. F.; Park, J. S.; Zheng, Y.; Balakrishnan, J.; Lei, T.; Kim, H. R.; Song, Y. I.; Kim, Y. J.; Kim, K. S.; Ozyilmaz, B.; Ahn, J. H.; Hong, B. H.; Iijima, S., Roll-to-roll production of 30-inch graphene films for transparent electrodes. *Nat Nanotechnol* **2010**, *5* (8), 574-578.
5. Yan, Z.; Lin, J.; Peng, Z. W.; Sun, Z. Z.; Zhu, Y.; Li, L.; Xiang, C. S.; Samuel, E. L.; Kittrell, C.; Tour, J. M., Toward the Synthesis of Wafer-Scale Single-Crystal Graphene on Copper Foils. *Acs Nano* **2012**, *6* (10), 9110-9117.
6. Chen, S. S.; Ji, H. X.; Chou, H.; Li, Q. Y.; Li, H. Y.; Suk, J. W.; Piner, R.; Liao, L.; Cai, W. W.; Ruoff, R. S., Millimeter-Size Single-Crystal Graphene by Suppressing Evaporative Loss of Cu During Low Pressure Chemical Vapor Deposition. *Adv Mater* **2013**, *25* (14), 2062-2065.
7. Hao, Y. F.; Bharathi, M. S.; Wang, L.; Liu, Y. Y.; Chen, H.; Nie, S.;

- Wang, X. H.; Chou, H.; Tan, C.; Fallahazad, B.; Ramanarayan, H.; Magnuson, C. W.; Tutuc, E.; Yakobson, B. I.; McCarty, K. F.; Zhang, Y. W.; Kim, P.; Hone, J.; Colombo, L.; Ruoff, R. S., The Role of Surface Oxygen in the Growth of Large Single-Crystal Graphene on Copper. *Science* **2013**, 342 (6159), 720-723.
8. Zhou, H. L.; Yu, W. J.; Liu, L. X.; Cheng, R.; Chen, Y.; Huang, X. Q.; Liu, Y.; Wang, Y.; Huang, Y.; Duan, X. F., Chemical vapour deposition growth of large single crystals of monolayer and bilayer graphene. *Nat Commun* **2013**, 4.
 9. Cho, S. Y.; Kim, M.; Kim, M. S.; Lee, M. H.; Kim, K. B., Effect of Cu surface treatment in graphene growth by chemical vapor deposition. *Mater Lett* **2019**, 236, 403-407.
 10. Cho, S. Y.; Kim, M. S.; Kim, M.; Kim, K. J.; Kim, H. M.; Lee, D. J.; Lee, S. H.; Kim, K. B., Self-assembly and continuous growth of hexagonal graphene flakes on liquid Cu. *Nanoscale* **2015**, 7 (30), 12820-12827.
 11. Kwon, K. C.; Choi, K. S.; Kim, S. Y., Increased Work Function in Few-Layer Graphene Sheets via Metal Chloride Doping. *Adv Funct Mater* **2012**, 22 (22), 4724-4731.
 12. Shin, D. H.; Lee, K. W.; Lee, J. S.; Kim, J. H.; Kim, S.; Choi, S. H., Enhancement of the effectiveness of graphene as a transparent conductive electrode by AgNO₃ doping. *Nanotechnology* **2014**, 25 (12).
 13. Khan, M. F.; Iqbal, M. Z.; Iqbal, M. W.; Eom, J., Improving the electrical properties of graphene layers by chemical doping. *Sci Technol Adv Mat* **2014**, 15 (5).
 14. Tongay, S.; Berke, K.; Lemaitre, M.; Nasrollahi, Z.; Tanner, D. B.;

- Hebard, A. F.; Appleton, B. R., Stable hole doping of graphene for low electrical resistance and high optical transparency. *Nanotechnology* **2011**, *22* (42).
15. Kim, M.; Kim, K. J.; Lee, S. J.; Kim, H. M.; Cho, S. Y.; Kim, M. S.; Kim, S. H.; Kim, K. B., Highly Stable and Effective Doping of Graphene by Selective Atomic Layer Deposition of Ruthenium. *Acs Appl Mater Inter* **2017**, *9* (1), 701-709.
 16. Kim, M.; Nabeya, S.; Nandi, D. K.; Suzuki, K.; Kim, H. M.; Cho, S. Y.; Kim, K. B.; Kim, S. H., Atomic Layer Deposition of Nickel Using a Heteroleptic Ni Precursor with NH₃ and Selective Deposition on Defects of Graphene. *Acs Omega* **2019**, *4* (6), 11126-11134.
 17. Won, S.; Hwangbo, Y.; Lee, S. K.; Kim, K. S.; Kim, K. S.; Lee, S. M.; Lee, H. J.; Ahn, J. H.; Kim, J. H.; Lee, S. B., Double-layer CVD graphene as stretchable transparent electrodes. *Nanoscale* **2014**, *6* (11), 6057-6064.
 18. Chen, S. S.; Brown, L.; Levendorf, M.; Cai, W. W.; Ju, S. Y.; Edgeworth, J.; Li, X. S.; Magnuson, C. W.; Velamakanni, A.; Piner, R. D.; Kang, J. Y.; Park, J.; Ruoff, R. S., Oxidation Resistance of Graphene-Coated Cu and Cu/Ni Alloy. *Acs Nano* **2011**, *5* (2), 1321-1327.
 19. Kim, K. S.; Zhao, Y.; Jang, H.; Lee, S. Y.; Kim, J. M.; Kim, K. S.; Ahn, J. H.; Kim, P.; Choi, J. Y.; Hong, B. H., Large-scale pattern growth of graphene films for stretchable transparent electrodes. *Nature* **2009**, *457* (7230), 706-710.
 20. Gunes, F.; Shin, H. J.; Biswas, C.; Han, G. H.; Kim, E. S.; Chae, S. J.; Choi, J. Y.; Lee, Y. H., Layer-by-Layer Doping of Few-Layer Graphene Film. *Acs Nano* **2010**, *4* (8), 4595-4600.
 21. Wang, Y.; Tong, S. W.; Xu, X. F.; Ozyilmaz, B.; Loh, K. P., Interface

- Engineering of Layer-by-Layer Stacked Graphene Anodes for High-Performance Organic Solar Cells. *Adv Mater* **2011**, 23 (13), 1514-1518.
22. Wu, W.; Yu, Q. K.; Peng, P.; Liu, Z. H.; Bao, J. M.; Pei, S. S., Control of thickness uniformity and grain size in graphene films for transparent conductive electrodes. *Nanotechnology* **2012**, 23 (3).
 23. Kasry, A.; Kuroda, M. A.; Martyna, G. J.; Tulevski, G. S.; Bol, A. A., Chemical Doping of Large-Area Stacked Graphene Films for Use as Transparent, Conducting Electrodes. *Acs Nano* **2010**, 4 (7), 3839-3844.
 24. Pirkle, A.; Chan, J.; Venugopal, A.; Hinojos, D.; Magnuson, C. W.; McDonnell, S.; Colombo, L.; Vogel, E. M.; Ruoff, R. S.; Wallace, R. M., The effect of chemical residues on the physical and electrical properties of chemical vapor deposited graphene transferred to SiO₂. *Appl Phys Lett* **2011**, 99 (12).
 25. Lafkioti, M.; Krauss, B.; Lohmann, T.; Zschieschang, U.; Klauk, H.; von Klitzing, K.; Smet, J. H., Graphene on a Hydrophobic Substrate: Doping Reduction and Hysteresis Suppression under Ambient Conditions. *Nano Lett* **2010**, 10 (4), 1149-1153.
 26. Gannett, W.; Regan, W.; Watanabe, K.; Taniguchi, T.; Crommie, M. F.; Zettl, A., Boron nitride substrates for high mobility chemical vapor deposited graphene. *Appl Phys Lett* **2011**, 98 (24).
 27. Suk, J. W.; Lee, W. H.; Lee, J.; Chou, H.; Piner, R. D.; Hao, Y. F.; Akinwande, D.; Ruoff, R. S., Enhancement of the Electrical Properties of Graphene Grown by Chemical Vapor Deposition via Controlling the Effects of Polymer Residue. *Nano Lett* **2013**, 13 (4), 1462-1467.
 28. Levesque, P. L.; Sabri, S. S.; Aguirre, C. M.; Guillemette, J.; Siaj, M.;

- Desjardins, P.; Szkopek, T.; Martel, R., Probing Charge Transfer at Surfaces Using Graphene Transistors. *Nano Lett* **2011**, *11* (1), 132-137.
29. Jung, D. Y.; Yang, S. Y.; Park, H.; Shin, W. C.; Oh, J. G.; Cho, B. J.; Choi, S. Y., Interface engineering for high performance graphene electronic devices. *Nano Converg* **2015**, *2*.
 30. Dean, C. R.; Young, A. F.; Meric, I.; Lee, C.; Wang, L.; Sorgenfrei, S.; Watanabe, K.; Taniguchi, T.; Kim, P.; Shepard, K. L.; Hone, J., Boron nitride substrates for high-quality graphene electronics. *Nat Nanotechnol* **2010**, *5* (10), 722-726.
 31. Nagashio, K.; Nishimura, T.; Kita, K.; Toriumi, A., Mobility Variations in Mono- and Multi-Layer Graphene Films. *Appl Phys Express* **2009**, *2* (2).
 32. Uemura, K.; Ikuta, T.; Maehashi, K., Turbostratic stacked CVD graphene for high-performance devices. *Jpn J Appl Phys* **2018**, *57* (3).
 33. Krajewska, A.; Pasternak, I.; Sobon, G.; Sotor, J.; Przewloka, A.; Ciuk, T.; Sobieski, J.; Grzonka, J.; Abramski, K. M.; Strupinski, W., Fabrication and applications of multi-layer graphene stack on transparent polymer. *Appl Phys Lett* **2017**, *110* (4).
 34. Kim, M.; Nabeya, S.; Han, S.-M.; Kim, M.-S.; Lee, S.; Kim, H.-M.; Cho, S.-Y.; Lee, D.-J.; Kim, S.-H.; Kim, K.-B., Selective Atomic Layer Deposition of Metals on Graphene for Transparent Conducting Electrode Application. *Acs Appl Mater Inter* **2020**.
 35. Kim, S. J.; Ryu, J.; Son, S.; Yoo, J. M.; Park, J. B.; Won, D.; Lee, E. K.; Cho, S. P.; Bae, S.; Cho, S.; Hong, B. H., Simultaneous Etching and Doping by Cu-Stabilizing Agent for High-Performance Graphene-Based Transparent Electrodes. *Chem Mater* **2014**, *26* (7), 2332-2336.

36. Ermolieff, A.; Chabli, A.; Pierre, F.; Rolland, G.; Rouchon, D.; Vannuffel, C.; Vergnaud, C.; Baylet, J.; Semeria, M. N., XPS, Raman spectroscopy, X-ray diffraction, specular X-ray reflectivity, transmission electron microscopy and elastic recoil detection analysis of emissive carbon film characterization. *Surf Interface Anal* **2001**, *31* (3), 185-190.
37. Zhao, F.; Vrajitoarea, A.; Jiang, Q.; Han, X. Y.; Chaudhary, A.; Welch, J. O.; Jackman, R. B., Graphene-Nanodiamond Heterostructures and their application to High Current Devices. *Sci Rep-Uk* **2015**, *5*.
38. Suwaiyan, A.; Zwarich, R.; Baig, N., Infrared and Raman-Spectra of Benzimidazole. *J Raman Spectrosc* **1990**, *21* (4), 243-249.
39. Mohan, S.; Sundaraganesan, N.; Mink, J., Ftir and Raman Studies on Benzimidazole. *Spectrochim Acta A* **1991**, *47* (8), 1111-1115.
40. Dong, X. C.; Fu, D. L.; Fang, W. J.; Shi, Y. M.; Chen, P.; Li, L. J., Doping Single-Layer Graphene with Aromatic Molecules. *Small* **2009**, *5* (12), 1422-1426.
41. Das, A.; Pisana, S.; Chakraborty, B.; Piscanec, S.; Saha, S. K.; Waghmare, U. V.; Novoselov, K. S.; Krishnamurthy, H. R.; Geim, A. K.; Ferrari, A. C.; Sood, A. K., Monitoring dopants by Raman scattering in an electrochemically top-gated graphene transistor. *Nat Nanotechnol* **2008**, *3* (4), 210-215.
42. Hao, Y. F.; Wang, Y. Y.; Wang, L.; Ni, Z. H.; Wang, Z. Q.; Wang, R.; Koo, C. K.; Shen, Z. X.; Thong, J. T. L., Probing Layer Number and Stacking Order of Few-Layer Graphene by Raman Spectroscopy. *Small* **2010**, *6* (2), 195-200.
43. Ferrari, A. C.; Basko, D. M., Raman spectroscopy as a versatile tool for studying

- the properties of graphene. *Nat Nanotechnol* **2013**, 8 (4), 235-246.
44. Yan, K.; Peng, H. L.; Zhou, Y.; Li, H.; Liu, Z. F., Formation of Bilayer Bernal Graphene: Layer-by-Layer Epitaxy via Chemical Vapor Deposition. *Nano Lett* **2011**, 11 (3), 1106-1110.
 45. Wang, Y. Y.; Ni, Z. H.; Yu, T.; Shen, Z. X.; Wang, H. M.; Wu, Y. H.; Chen, W.; Wee, A. T. S., Raman studies of monolayer graphene: The substrate effect. *J Phys Chem C* **2008**, 112 (29), 10637-10640.
 46. Petritz, R. L., Theory of an Experiment for Measuring the Mobility and Density of Carriers in the Space-Charge Region of a Semiconductor Surface. *Phys Rev* **1958**, 110 (6), 1254-1262.
 47. Arnaudov, B.; Paskova, T.; Evtimova, S.; Valcheva, E.; Heuken, M.; Monemar, B., Multilayer model for Hall effect data analysis of semiconductor structures with step-changed conductivity. *Phys Rev B* **2003**, 67 (4).
 48. Bierwagen, O.; Choi, S.; Speck, J. S., Hall and Seebeck measurement of a p-n layer stack: Determining InN bulk hole transport properties in the presence of a strong surface electron accumulation layer. *Phys Rev B* **2012**, 85 (16).
 49. Adam, S.; Hwang, E. H.; Galitski, V. M.; Das Sarma, S., A self-consistent theory for graphene transport. *P Natl Acad Sci USA* **2007**, 104 (47), 18392-18397.

CHAPTER 5.

Summary and conclusions

After graphene was first discovered in 2004, due to the outstanding properties, graphene has attracted great attention. In particular, graphene has a high charge carrier mobility. In this work, the electrical property of single and multilayer CVD graphene are investigated. Therefore, the structure of graphene and the origin of its physical properties especially electrical property were discussed in Chapter 1. Moreover, the band structure derived from the lattice structure of graphene shows that the high mobility and low carrier density in intrinsic graphene. Although graphene has excellent intrinsic electrical properties, it is degraded by various factors. The factors affecting the electrical properties of CVD graphene are also discussed in Chapter 1 in terms of carrier density and mobility. The change in carrier density caused doping by molecule adsorption, and the results of improving electrical properties through doping were investigated. It also summarized efforts to reduce scattering factors at the interface with the substrate and at the grain boundary which degrades carrier mobility.

The mechanism of direct visualization of the graphene grain boundary on Cu through Cu oxidation and the effect of Cu oxide growth on the electrical properties of single-layer graphene are investigated in chapter 2. The kinetics of Cu oxidation through graphene grain boundaries were quantitatively determined based on the Cu oxide coverage that was determined from the optical microscopy image. There are three unique features in discussing Cu₂O growth behavior on graphene. First, Cu₂O growth kinetics undergoes one-dimensional growth. The optical microscopy image and JMAK equation analysis shows the Cu₂O nucleation is limited in graphene grain boundaries and the Cu₂O one-dimensionally grows with suppressed further nucleation. Second, the Cu₂O growth is governed by dominant Cu cation out-

diffusion in according to HR-TEM analysis reveals graphene layer is at the Cu-Cu₂O interface which indicates that the graphene layer is not critically damaged by the volume expansion of Cu oxide. Third, the variation of the sheet resistance as a function of annealing temperature and time was converted into one curve as a function of Cu oxide coverage (F_{ox}). The sheet resistance of 250 Ω /sq was constant, similar to that of as-grown graphene up to F_{ox} of 15% and then increased with F_{ox} . And, the F_{ox} of 10 ~ 15% confirmed that the graphene grain size could be measured without degradation of the electrical property of graphene, and suggested that the optimal condition considering practical points of experiments such as process margin is oxidation at 200°C for 100 min. The drastic sheet resistance increasing in 15 ~ 50% of F_{ox} resulted from the decreasing of mobility which is revealed by Hall measurement. It was explained by electrical conduction of graphene is disconnected by Cu₂O formation along with the graphene grain boundary, even though the Cu oxide formed above the graphene.

In chapter 3, to confirm the surface roughness effect of metal catalyst on the formation of graphene grain boundaries in CVD growth, liquid Cu phase effect on graphene growth has been studied by direct comparison of graphene on solid and liquid Cu. Although the coverage rate of graphene increased at high temperatures on solid Cu, the growth rate of graphene was extremely retarded on liquid Cu. This clearly shows that surface smoothening drastically suppresses hetero-nucleation of graphene seeds. Nuclei density of graphene was reduced from 3 to 0.0004/m² by the liquid catalyst effect. However, the lateral grain size also increased almost by 2 orders of magnitude from 0.4 to 38.3 μ m. The irregular shape of graphene grains changed into symmetrical hexagons on liquid Cu, which were well aligned with the same orientation. The decrease in the intensity ratio of I_D/I_G from 0.3–0.8 to 0.1

provided clear evidence of the defect density decrease as a result of the reduction of the graphene grain boundary. Finally, this was confirmed from the sheet resistance, which was reduced from 1764 to 484 ohm/sq. Simple melting of Cu catalyst provides an improvement of the graphene quality without further tuning of the growth parameters.

In chapter 4, the variation in the sheet resistance of multilayer graphene as a function of graphene layers is investigated depending on dopant and polymer residue position. The origin of the sheet resistance variation was determined by Hall measurements. Overall, we found that the sheet resistance decreased gradually with an increase in the number of graphene layers. However, the Hall measurements showed that the main factors contributing to the sheet resistance reduction in the two cases of inter-layer doped and undoped are different. The layer-stacked graphene with interlayer doping showed a decrease in sheet resistance by the increase of sheet carrier density with the increase of the number of the graphene layers. This is well-matched to the conventional conductivity theory of metals assuming the identical physical properties in each graphene layer. The multilayer graphene without the interlayer molecular doping showed an increase in carrier mobility with the number of graphene layers, while the sheet carrier density remained almost constant. This result means that each graphene layer has different physical properties such as sheet carrier density and carrier mobility, and the characteristics of each graphene layer can be extracted by the calculation of Hall mobility at the heterojunction. From the calculation, the inner-layer of interlayer undoped multilayer graphene shows carrier density and mobility of $6 \times 10^{11} / \text{cm}^2$ and $5000 \text{ cm}^2/\text{Vs}$, respectively. In addition, if the PMMA residues are existed in the graphene interface, they act as a dopant, resulting the electrical properties of inner layers same, resulting in a decrease in sheet

resistance due to an increase in carrier density. Therefore, the mobility is maintained at $1100 \text{ cm}^2/\text{Vs}$ regardless of the number of graphene layers. Further, I confirmed the separate controllability of doping concentration and mobility enhancement in multilayer graphene by doping the top layer of the interlayer-undoped graphene and multilayer graphene with mixed conduction channels.

Abstract (in Korean)

그래핀(graphene)은 2차원(2D) 재료의 가장 주목할만한 물질이다. 뛰어난 전기적 광학적 및 기계적 특성으로 인해 많은 관심을 끌었습니다. 이 논문에서는 화학적기상증착(CVD)로 합성된 단일층 및 다층 그래핀의 전기적 특성을 연구하였다. CVD를 통해 성장한 그래핀은 본질적으로 다결정성을 보인다. 그 결과 구조적 결함으로 형성되는 결정립계에서의 산란으로 인해 전하의 수송이 방해받는다. 2장에서는 이러한 그래핀의 결정립계를 산화구리 형성을 통해 구리위에서 직접시각화하는 매커니즘과 구리산화물 성장이 그래핀의 전기적 특성미치는 영향을 설명하였다. 그리고 3장에서는 그래핀을 액체구리 위에서 성장시킴으로써 구리표면의 거칠기가 그래핀의 결정립계 형성 및 전기적 특성에 미치는 영향을 연구하였다. 마지막으로 4장에서는 닷층 그래핀의 전기적 특성에 대한 그래핀간의 계면 및 표면 특성의 영향을 그래핀 층수에 따라 연구한 결과를 설명하였다.

1장은 연구의 배경 소개 섹션이다. 그래핀의 특성에 대한 개요를 제공한다. 또한 그래핀을 합성하는 다양한 방법에 대해 간략히 설명하였다. 그중 금속 촉매를 이용한 CVD방법의 장점과 원리도 소개한다. CVD에 의해 합성된 그래핀은 고품질을 가지는 것으로 알려져 있지만, 다양한 논문에서 보고한 그래핀의 전기적 특성은 모두 단일층으로 합성했음에도 불구하고 매우 다른데 이러한 이유는 그래핀의 두께가 너무 얇아서 다양한 요인이 전기적 특성에 결정적인 영향을 미치기 때문이다. 그래핀의 전기적 특성에 영향을 미치는 요인을 표면도핑, 계면산란 및 결정립계 산란으로 나누어 요약 및 설명하였다.

2장에서는 그래핀 결정립계의 직접 시각화를 설명한다. 그래핀 결정립계에서의 구리산화물을 통해 광학현미경을 통해 그래핀 결정립을 확인할 수 있다.. 그래핀 결정립계를 통한 산화구리 형성은 대기 환경에서 산화시간(10-360분)과 온도(180°C-240°C)를 변화시켜 산화구리의 표면 커버리지(F_{ox})를 평가하였다. 투과 전자 현미경 연구는 Cu_2O 성장이 그래핀 결정립계를 통한 구리의 외부확산에 의해 좌우된다는 것을 밝혔다. 또한 산화구리형성이 그래핀 품질에 미치는 영향은 그래핀을 PET위로 전사 후 그래핀의 전기적 특성을 측정하여 조사 하였다. 모든 산화온도에서 산화시간의 함수로서 면저항의 변화는 F_{ox} 의 함수로서 하나의 곡선으로 변환되었다. 250 Ω/sq 으로 측정된 산화전 그래핀의 면저항은 산화후에는 $F_{ox} = 15\%$ 까지는 산화처리전 그래핀과 비슷했으며 그후에는 F_{ox} 의 증가와 함께 갑자기 증가했다 이러한 면저항의 증가는 전적으로 그래핀의 손상에 의해서 나타난 것임을 홀 이동성이 감소하는 것으로 확인하였다. 따라서 우리는 그래핀 결정립계를 통해 구리의 산화동력학을 체계적으로 개발하고 동시에 그래

핀의 전기적 특성 변화를 조사했다.

4장에서는 계면 및 표면특성이 다른 다층 그래핀의 전기적 특성을 연구한 결과를 설명한다. CVD로 구리위에 성장된 단일층 그래핀을 여러 번의 전사를 통하여 모든 종류의 다층 그래핀을 준비하였다. 먼저, 다층 그래핀에서 그래핀간의 계면 특성에 따라서 전기적 특성에 미치는 영향을 확인하고자 그래핀 층사이의 도펀트 유무에 따라 층수를 1 ~ 12층으로 변경하여 조사하였다. 두 경우 모두 층수가 증가함에 따라 면저항은 감소했다. 도핑되지 않은 그래핀의 경우 면저항이 700에서 104 Ω/sq 으로, 층간 도핑 된 그래핀의 경우는 280에서 25 Ω/sq 으로 감소하였다. 각샘플의 홀측정을 통해서 두 경우의 면저항 감소원인이 다른 것을 확인했다. 층간 도핑되지 않은 그래핀에서는 층수가 증가함에 따라 캐리어 밀도가 낮고 캐리어 이동도가 높은 내부 층이 추가되어 이동도가 증가하여 면저항이 감소했다. 반면, 층간 도핑된 다층 그래핀은 캐리어 밀도 증가로 인해 감소했다. 두 경우 모두의 이동성과 캐리어 밀도 변화는 이중 접합에서의 홀효과와 모델을 적용하여 수식적으로도 확인하였다. 또한 그래핀 층사이에 폴리머 잔류물이 있어도 도펀트처럼 작용하여 그래핀 층의 수가 증가할수록 이동도는 변하지 않고 캐리어 밀도가 증가한다는 것을 발견했다. 또한, 다층그래핀의 상부층의 표면도핑 및 부분 커버리지가 다른 이중 층 그래핀의 형성에 의한 표면 특성 수정은 캐리어 밀도 및 이동도를 개별적으로 제어 할 수 있음을 확인하였다.

결론적으로 본연구에서는 단층 및 다층 그래핀의 전기적 특성을 연구하였다. 산화구리를 통한 그래핀 결정립 시각화는 그래핀 결정립계에서 구리 양이온의 확산에 의해 제어되어 그래핀 품질에 대한 손상을 최소화하므로, 구리 산화물 커버리지의 최대 15%까지 그래핀의 전기적 특성에 열화가 관찰되지 않았다. 고체 및 액체 구리에 대한 그래핀의 성장 거동을 비교함으로써 액체 구리의 극히 평평한 표면은 이중 핵형성을 극도로 감소시킴으로써 결정립 크기를 증가시키는 것이 제안된다. 따라서 액체 구리에서 합성된 그래핀의 캐리어 이동성이 향상된다. 마지막으로 도펀트와 고분자 잔류물의 위치를 달리하여 다층 그래핀의 계면 및 표면 특성에 따라 면저항 감소의 주요요인이 달라짐을 확인되었다. 전자소자 적용을 위한 다층 그래핀의 특성을 제어하기 위한 효과적인 접근방식을 제공한다.

주요어: 그래핀, 결정립계, 시각화, 다층그래핀, 면저항, 캐리어 밀도, 이동도

학번: 2014-30208